SCANNING TRANSMISSION ELECTRON MICROSCOPY TOMOGRAPHY AND 4D-STEM APPLIED TO THE STUDY OF CHIRAL AND SELF-ASSEMBLED NANOPARTICLES

by

Alessandra da Silva

A thesis submitted to The University of Birmingham for the degree of

DOCTOR OF PHILOSOPHY

UNIVERSITY OF BIRMINGHAM

Nanoscale Physics Research Laboratory
School of Physics and Astronomy
University of Birmingham
Birmingham, UK.

July 2020

Acknowledgements

I would like to thank,

Dr. Wolfgang for his supervision and support throughout this PhD. I am grateful for his critical output and the invaluable knowledge of science and analysis that I have learnt from him, especially python.

Dr. Peter Ercius for his supervision while I was working at the Molecular Foundry and for always being positive. Also, for the opportunity to be involved in these projects.

The Brazilian National Council of Technological and Scientific Development (CNPq) for funding my PhD.

Dr. Karen Bustillo for her support and suggestions with the electron microscope. Dr. Assaf Ben-Moshe for the opportunity of collaboration and for the interesting discussions and trust in my work.

To Dr. Ian Stevens for being so ethical and his respect and unconditional support to students in Birmingham.

Prof. Steve Donnelly for being humble and helping me out with difficult times.

Dr. Jonathan Hinks for being an exceptional professional and always willing to help with technical problems.

To my family for all the support and friendship that they always have offered me during my entire life.

My friends Matt, Ximenes, Cristiane, Paula and Tais that even though we were physically distant they were always in touch and offering me support throughout this PhD.

My dear Anna Berger, Radames, Clare and Yara for making my time in Berkeley better.

To Fran and Eamonn for being nice and trying to make our PhD period more enjoyable with the little things.

Finally, to my Patrickinho, for beyond the great scientific discussions, giving me unconditional support and cooking every day during my thesis writing period.

Abstract

Over recent years, advances in nanotechnology have led to an increased interest towards engineering nanomaterials with defined morphologies, for applications where the nanoparticle shape plays a significant role in processes, such as in catalysis, drug delivery and optics. Therefore, it is essential to resolve the 3D morphology and structure of these materials in order to gain understanding about their physical and chemical properties for further optimization. Following this line of research, this thesis explores a set of experiments that makes use of Scanning Transmission Electron Microscopy (STEM), incorporating both STEM tomography and 4D-STEM techniques. These techniques were used to investigate the origin of chiral shapes in Tellurium (Te) bipyramidal nanoparticles, where it was determined that the chiral geometries of the nanoparticles arise from growth mediated by screw dislocations rather than chiral ligands used in their synthesis. Gold (Au) nanoparticle self-assembled superlattices were studied by electron tomography and their lattice structure was investigated through determination of the 3D nanoparticle positions. The superlattices were found to have different crystalline structures for different molecular weights of their protective ligands. Finally, gold nanoparticles that seemed to have a twisted bipyramidal geometry were investigated through electron tomography. A model was built from the reconstructed cross-sections which supported the conclusion that the asymmetry in the shape resulted from the arrangement of the facets rather than a twist. The analyses performed in this thesis were custom-developed building upon general electron microscopy and mathematical concepts, enabling their application towards different systems and materials.

List of Figures

List of Acronyms

BCC	Body Centered Cubic
BF	Bright Field
CBED	Convergent Beam Electron Diffraction
CTAB	Cetyltrimethylammonium Bromide
DF	Dark Field
EELS	Electron Energy-Loss Spectroscopy
ET	Electron Tomography
FBP	Filtered Back Projection
FCC	Face Centered Cubic
FFT	Fast Fourier Transform
FOLZ	First Order Laue Zone
HCP	Hexagonal Closed Packed
NBED	Nano-Beam Electron Diffraction
NN	Nearest Neighbour
PGNP	Polymer Grafted Nanoparticles
PP	Polypropylene
PS	Polystyrene
RHCP	Random Hexagonal-Closed Packed
SAD	Selected Area Diffraction
SF	Stacking Faults
SIRT	Simultaneous Iterative Reconstruction Technique
SLSQP	Sequential Least Squares Programming

SOLZ	Second Order Laue Zone
STEM	Scanning Transmission Electron Microscopy
TEM	Transmission Electron Microscopy
VBF	Virtual Bright Field
VDF	Virtual Dark Field
VLM	Visible-Light Microscopes
WBP	Weighted Back-Projection
ZOLZ	Zero Order Laue Zones
4D-STEM	Four-Dimensional Scanning Transmission Electron Microscopy

List of Symbols

Latin Symbols

a	first lattice parameter
a_0	Bohr radius
$\vec{b}$	Burgers vector
c	second lattice parameter
c_l	speed of light in the vacuum
C_B	electron beam spot in a diffraction pattern
C_L	center of ZOLZ circle
d	real-space interplanar distance
d_p	pixel size
D	final diameter of the reconstruction
D_r	minimum resolved distance
D_x	tomography resolution along the x-axis
D_y	tomography resolution along the y-axis
D_z	tomography resolution along the z-axis
e	electron charge
$\vec{e}$	electron beam direction
e_s	scale factor
e_{yz}	elongation factor on the z-axis
F_{1D}	1D Fourier transform
F_{2D}	2D Fourier transform
F_{nn}	cumulative NN distribution

$\vec{g}$	reciprocal lattice vector
h	Planck constant
hkl	Miller indices of parallel atomic plans
j	jth scan line index
j'	$j'th$ scan line index
k_x	horizontal reciprocal coordinate
k_y	vertical reciprocal coordinate
$\overrightarrow{K_I}$	wave vector of the incident electron beam
$\overrightarrow{K_D}$	wave vector of the diffracted electron beam
$\overrightarrow{\Delta K}$	difference between the incident and diffracted wavefront normal vectors
L	camera length
L_{lig}	extended ligand length
l	distance between twist bands
M_n	molecular weight
m_0	electron rest mass
n	natural number
n_p	degree of polymerization
N	Laue zone order
N_p	number of projections
P	general point
R_θ	Radon transform
r	radius
r_s	short axis of an irregular pentagon
r^*	radius of the ZOLZ circle

t	integral line variable in the Radon transform
x, y	horizontal and vertical cartesian coordinates
$x_c, y_{c,}\, r$	parameters of the ZOLZ circle
$x_0, y_{0,}\, r_0$	first estimation for ZOLZ circle parameters
$\vec{v}$	generic vector
V	accelerating voltage
$[uvw]$	electron beam direction
Z	atomic number

Greek Symbols

a_c	convergence angle
α	tilt angle
α_m	measured tilt angle
α_{off}	offset in the tilt angle
β	beam tilt
β_c	collection semi-angle
β_g	angle between $\vec{g}$ vectors
ε	residuals of circle fitting
ε_0	dielectric constant
δ	Dirac delta function
Δφ	angular deviation in the vertices of a pentagon
θ	generic angle
θ_B	Bragg's angle of diffraction
θ_{off}	angular offset

θ_t	rotation of the tilt axis from the horizontal direction
θ_0	screening parameter
λ	electron beam wavelength
λ_s	soft parameter
μ	refractive index
ρ	average density of nanoparticles
Σ	grafting density
σ	standard deviation of a gaussian filter
σ_R	differential Rutherford scattering cross section
τ	Eshelby twist
$\emptyset$	zone-axis mistilt
$\emptyset_x$	out-of-plane bending along c-axis
$\emptyset_y$	rotation around c-axis
ω	frequency coordinate
Ω	solid angle of scattering

Table of Contents

1 Introduction

This introductory chapter gives a brief overview of some key concepts from the fields of electron microscopy and nanomaterials, which support the experiments presented in this thesis. Section 1.1 gives an overview of why electron sources are used to image nanomaterials. Section 1.2 introduces the basic modes of operation in transmission electron microscopy (TEM) and scanning transmission electron microscopy (STEM). Section 1.3 gives an overview of the diffraction patterns resulting from parallel and convergent beams. Section 1.4 presents the common crystal structures in bulk metals and in particular the structures of the bulk materials studied in this thesis: tellurium and gold. Finally, section 1.5 gives an outline of how this thesis is organized.

1.1 Images from electrons

1.1.1 Interaction of the electrons with the specimen

When electrons interact with matter they are scattered and according to their final energy the scattering will be either elastic, when there is no measurable loss of energy, or inelastic. Elastic scattering happens mainly due to the interactions between the electron and the nuclei of the specimen. On the other hand, inelastic processes primarily occur when the incident electron beam interacts with the electrons from the atoms of the specimen. Both types of scattering are useful for studying materials. In the past, the elastically scattered electrons used to be the only signal used in classical TEM, since they generate the direct beam and much of the intensity in the diffraction patterns[1].

Inelastic scattering processes are studied with electron energy-loss spectrometry (EELS) and X-ray techniques and they are responsible for specimen damage, since the electrons transfer energy into the specimen. These techniques provide important information about the chemistry and electronic structure of the specimen[1].

If the scattered electrons are in phase, the scattering process it is called *coherent*, in contrast the process is named *incoherent*, when the electrons are scattered with different phases.

At low angles, elastic scattering is mostly coherent, but becomes progressively incoherent with increasing scattering angle. On the other hand, inelastic scattering is mostly incoherent. The coherence of electrons is important because it is associated with their angle of scattering and therefore with the arrangement of the atoms in the specimen.

In particular, high-angle scattering, caused by the electron-nucleus interaction, can be described by the differential Rutherford scattering cross section[2]:

$$\sigma_R(\theta) = \frac{Z^2\lambda^4}{64\pi^4 a_0^2} \frac{d\Omega}{\left[sin^2\left(\frac{\theta}{2}\right) + \frac{\theta_0^2}{2}\right]^2} \tag{1.1}$$

Where Z is the atomic number, $a_0 = \frac{h^2 \varepsilon_0}{\pi m_0 e^2}$ is the Bohr radius of the scattering atom, λ is the relativistic electron wavelength, Ω is the solid angle of scattering, θ is the scattering angle and θ_0 is the screening parameter.

High angle elastically scattered electrons are used for STEM Z-contrast imaging, and this signal is due to Rutherford scattering. This will be shown in more detail in the section 1.2, where the high-angle annular dark field (HAADF) detector is presented.

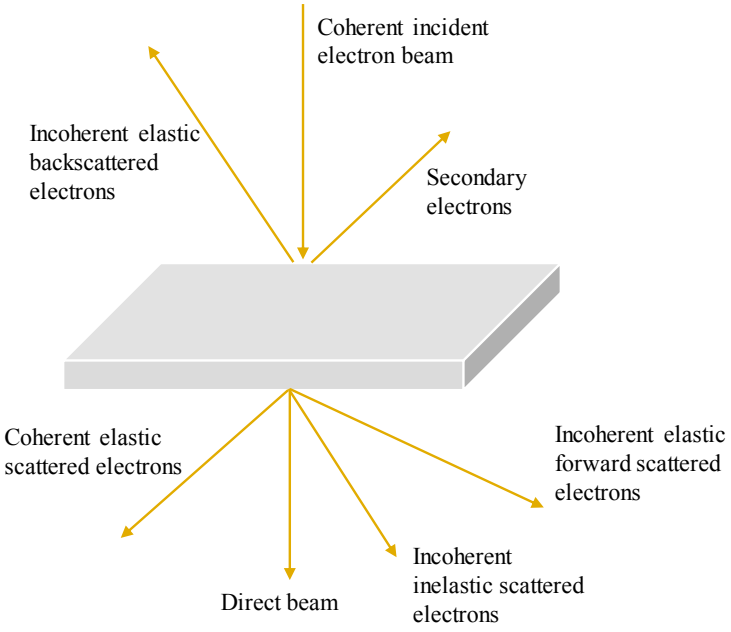

Figure 1-1 Diagram showing a scheme with the different kinds of electron scattering in a thin specimen. Adapted with permission from Williams, D.B. and Carter C.B.[1] Copyright 2009 Springer Nature.

1.1.2 Resolution

The most intuitive way of imaging a material is through the use of light sources, such as in photography or in visible-light microscopes (VLM). However, these sources have insufficient resolution to image features smaller than the wavelength of visible light (~400-700 nm), and therefore other sources with shorter wavelengths are needed for this purpose.

Electrons are the most adequate source to acquire information from atoms and materials at the nanoscale. High energy electrons have short wavelengths which leads to high resolution imaging. In TEM, the resolution is limited by diffraction effects and lens aberrations. It is simpler to describe the TEM in terms of classic Rayleigh Criterion for VLM[3], where the minimum distance (D_r) that can be resolved is given by[1]:

$$D_r = 0.61 \frac{\lambda}{\mu \sin \beta_c} \tag{1.1}$$

Where λ is the radiation wavelength, μ is the refractive index and β_c is the semi-angle of collection of the magnifying lens. For simplicity, $\mu \sin \beta_c$, can be approximated to unity.

$$D_r = 0.61\, \lambda \tag{1.2}$$

For example, in an optical microscope, where the visible light wavelength ranges from 400 to 750 nm, this expression results in a maximum wavelength-dependent resolution of approximately 244 to 457 nm.

In the case of electrons, the relativistic wavelength is given by:

$$\lambda = \frac{h}{\sqrt{2m_0 eV(1 + \frac{eV}{2m_0 {c_l}^2})}} \tag{1.3}$$

Where h is the Planck constant, m_0 is the mass of the electron, e is electron charge, V is the accelerating voltage and c_l is the speed of light in a vacuum.

Therefore, by increasing the acceleration voltage, the electron wavelength is decreased, and the resolution is improved. As an illustration, for an accelerating voltage of 200 kV, which is common for electron microscopes, the wavelength of the electron is 2.51 pm and according to equation (1.2), the corresponding Rayleigh limit is 1.53 pm, which is much smaller than the lower limit of the VLM as presented above, and smaller in fact than the diameter of an atom (0.1-0.5 nm). In practice, the resolution of electron microscopes are far from the Rayleigh limit; the resolution of the electron microscopes are limited by aberrations in the electron lenses and the current resolution record is around 50 pm[4].

1.2 Transmission electron microscopy

A transmission electron microscope consists of three basic components: the illumination system, the objective lens system and the imaging system.

The main role of the illumination system is to accelerate and transport the electron beam to the sample, whereas the convergence of the beam at the sample plane (convergence angle, α_c) determines the mode of operation. In TEM mode the condenser lenses provide the illumination system and they are set to generate a parallel beam at the sample level, equivalent to a near zero α_c angle.

In TEM the imaging mode is selected by the objective aperture. When the objective aperture is centred on the direct beam, bright-field images are formed (Figure 1-2, a). On other hand, a dark-field image is formed when the objective aperture is centered on a diffracted spot - or the electron beam is tilted, such that a Bragg reflection is collected on-axis (Figure 1-2, b). The beam-tilt method is more commonly used for DF-TEM since it minimizes the aberrations and astigmatism caused by an off-axis beam[1,5].

Image contrast between both imaging modes is inverted. The direct beam is composed of electrons that were not deviated from their trajectory when interacting with the specimen. Regions of the specimen that scatter a significant proportion of electrons therefore appear dark on a bright background in bright-field imaging mode. By contrast in dark-field mode the high intensity regions indicate significant electron scattering. Scattering materials therefore look bright against a dark background during dark-field imaging.

TEM mode is ideal to image defects and the crystal structure of nanomaterials since it offers great image contrast and also precise information about the crystal structure of materials through their diffraction patterns. It is also advantageous compared to STEM mode in relation to contamination growth during the imaging due to smaller electron beam flux on the sample.

Interpretation of diffraction patterns compared to convergent beam electron diffraction (CBED) patterns in the STEM mode are also more straightforward.

STEM consists of a convergent beam that is rastered across the sample to collect the signals resulting from the interactions between sample and electron beam at each probe position. To achieve this, magnetic lenses are used to focus the electron beam into a small probe, which is scanned across the sample. The transmitted electrons from each area of the specimen are projected onto the STEM imaging system.

The STEM mode also can generate Bright-Field (BF-STEM) and Dark-Field (DF-STEM) images from the direct and scattered beam, respectively. However, the collected electron signal is determined through choice of detectors[1], where the electron collection angle (β_c) of the detector is adjusted by the camera length.

DF-STEM uses the signal from scattered electrons and incorporates annular dark field (ADF) and high angle ADF (HAADF) imaging. A schematic of the different modes of the STEM can be seen in Figure 1-2-b. The ADF detector is centred on the optical axis, but it is hollow in the middle to avoid electrons in the direct beam (where a BF detector is placed) in order to select the Bragg scattered beam. The contrast in the images produced from the ADF detector is derived from diffraction contrast and there is a close link between ADF-STEM and dark-field TEM images, produced by selecting a specific spot in the diffraction pattern[6]. Therefore, ADF images are very suitable for the study of defects and dislocations in crystalline materials[7].

In HAADF-STEM the collected electrons are scattered through high angles. Conventionally the inner HAADF angle is greater than 50 mrad[1], however there are different opinions about this limit and the angle will depend of the convergence angle used[8]. As mentioned above, this type of imaging provides Z-contrast, since for high angles, the scattered electron signal is primarily due to Rutherford scattering. However, the Z dependence of the

scattering cross-section σ_R is reduced from Z^2 to Z^n $(n = 1.0 - 1.8)$ due to electron screening effects[9].

The main advantage of HAADF-STEM is that the chemical composition of the sample can be resolved in many cases due to the variation in contrast for different elements (different Z), for example metal oxides and metal alloys. Also, by combining HAADF-STEM with aberration correction it is possible to image the atomic structure and composition of materials with sub-angstrom resolution[10]. Disadvantages of STEM microscopy include specimen damage from the electron beam, the focused electron probe is known to induce heating[11] and also build-up of organic contamination during imaging.

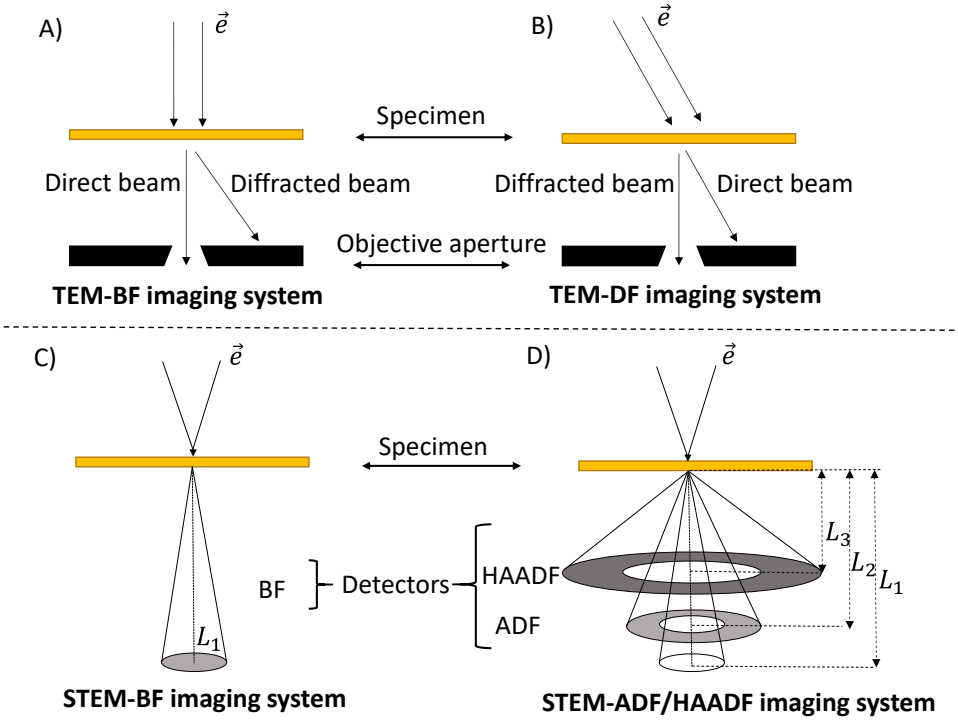

Figure 1-2 Comparison between BF and DF image formation in TEM and STEM modes. a) The BF mode formed in the TEM mode by selecting the direct beam through the objective aperture. b) a dark-field image is formed by tilting the beam such that a diffracted beam is on-axis. c) In STEM mode, the direct beam is collected by the BF detector, adjusted to a long camera length L_1. d) The ADF and HAADF are annular detectors that collect the scattered beam, by varying the camera length to shorter lengths (L_2 and L_3, respectively). Adapted with permission from Williams, D.B. and Carter C.B.[1] Copyright 2009 Springer Nature.

1.3 TEM and STEM diffraction

1.3.1 Ewald sphere and Laue zones

The Ewald sphere is a theoretical construction which defines the spots that will be visible in the diffraction pattern for a given incident electron beam with wavelength λ. In other words, the Ewald sphere determines the points in reciprocal space that are formed from constructive interference, i.e. the points obey the Bragg condition[12] ($\lambda = 2d \cdot sin\theta_B$), forming a sphere with radius $1/\lambda$. In reality, the reciprocal lattice is composed by rods instead of spherical spots, due to the effects from a finite sample shape. Figure 1-3 shows a 2D schematic where the Ewald sphere intercept a lattice - where $\vec{K}_I$ and $\vec{K}_D$ are the incident and diffracted beam wave vectors, respectively. In reality, as mention earlier, in TEM the electron wave is very short and therefore the radius of the Ewald sphere is very large. Thus, the diagram in Figure 1-3 is only to illustrate the concept, but in practice the sphere has a very small curvature.

During imaging in the TEM, it is standard procedure to tilt the sample until the crystal is oriented on axis, i.e. to rotate the sample until the normal to the lattice plane of interest is parallel to the electron beam direction. This is equivalent to tilting the sample until the Ewald sphere intersects the lattice at the intended direction - instead of cutting the lattice at intermediate points.

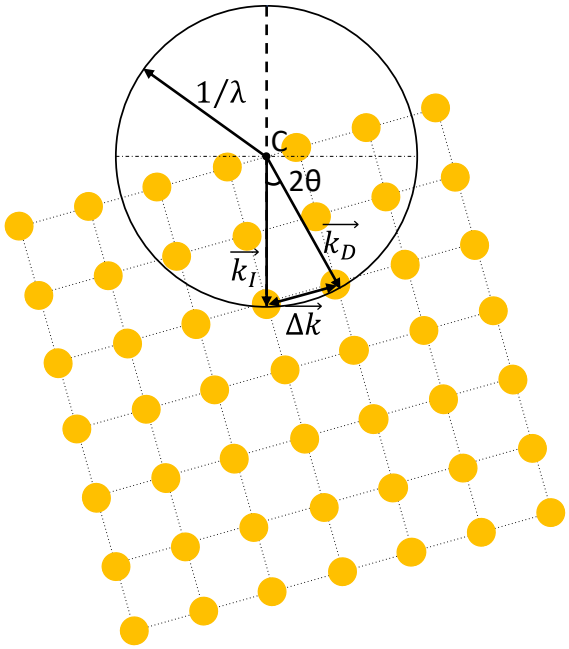

Figure 1-3 Scheme showing the Ewald sphere in 2D. The Ewald sphere has radius $1/\lambda$, where λ is the wavelength of the electron beam. The lattice points intersected by the sphere will be visible in the diffraction pattern.

Since the lattice and Ewald sphere are in three-dimensional space, there are different reflection planes intersected by the Ewald sphere as shown in Figure 1-4. Each individual plane is called a Laue Zone and given by[13]:

$$hu + kv + lw = N \tag{1.4}$$

where $[uvw]$ is the electron beam direction and hkl are the coordinates of the allowed reflection in the Nth order Laue zone. $N = 0$ gives rise to the circular and central diffraction pattern where the electron beam 000 is contained (Figure 1-4, b) and is called the Zero Order Laue Zone (ZOLZ). Analogously, $N = 1$ gives the first outer diffraction ring and it is denominated first Laue zone (FOLZ). The same applies for the high order Laue zones (HOLZ)[14].

Since the electron wavelength λ is very short, the curvature of the Ewald sphere is small and most of the electrons are scattered into the directions that are present in the ZOLZ[15].

Thus, a lower camera length is required and a wide field of view are required to acquire HOLZ.[16]

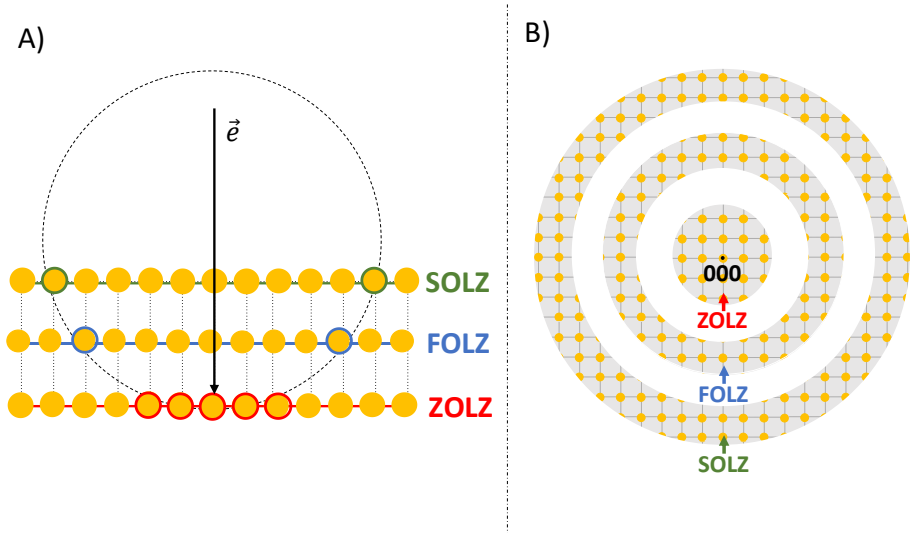

Figure 1-4 Scheme showing the Ewald Sphere and Laue circles. a) Lateral view showing zero (ZOLZ), first (FOLZ) and second (SOLZ) Laue zones. The highlighted circles are the spots observed in the diffraction pattern in each Laue zone circle b) In-plane view showing the Laue circle zones as observed in the electron microscope.

1.3.2 Diffraction pattern from different convergence angles

In TEM and STEM modes the difference in the convergence of the electron beam will result in different types of diffraction patterns. As mentioned earlier, in TEM mode the incident beam is parallel. The diffraction patterns are formed in the back focal plane, and the region of interest is selected by an aperture in the image plane of the objective lenses. The resulting diffraction pattern is formed by bright points (Figure 1-5, a). On the other hand, since in STEM mode the electron beam is convergent, the diffraction pattern formed will depend on the convergence angle α_c and, instead of using a mechanical aperture, the region from where diffraction information is extracted is selected by the area illuminated by the electron beam[16].

In STEM mode, instead of points, the diffraction patterns are formed by disks. The patterns contain different information depending of their characteristics. At high convergence angles each disk is full of crystallographic details and patterns are denominated *convergent-beam electron diffraction* (CBED) patterns (Figure 1-5,b).

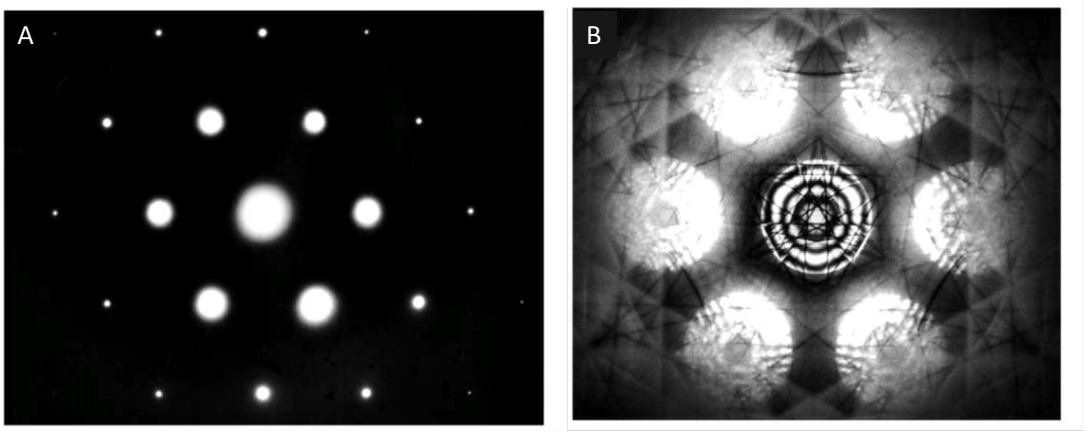

Figure 1-5 Different modes of diffraction according to the convergence angle α_c for a [111] Si sample. a) SAD pattern from a parallel beam, b) CBED pattern, from a convergent beam showing disks and Kikuchi lines. Adapted with permission from Williams, D.B. and Carter C.B.[1] Copyright 2009 Springer Nature.

Therefore, the type of diffraction data will highly depend on the convergence angle used in the experiment. Changing the convergence angle will not only result in the acquisition of different crystallographic information from different types of diffraction patterns, but will also result in the trade-off between real-space resolution and angular resolution in reciprocal space[17,18]. Smaller convergence angles produce probes with lower resolution, but on the other hand, they will result in more well-defined disks. In addition, when the convergence angle becomes very small, i.e. tends to zero, since the disks converge to a SAD pattern, only statistical crystal information from a relatively large area (> 100 nm in diameter) of the specimen is acquired - and local information and deviations in the lattice structure are difficult to detect from these patterns[19].

Conversely, when the convergence angle is increased but the beam is still nearly parallel, the size of the diffraction disks increases, and they will form a nanobeam electron diffraction (NBED) pattern – the origin of the name is derived from the fact that the focused probe can produce diffraction patterns from areas with less than 1 nm in diameter[20]. As a result, the diffraction pattern is formed from a much smaller volume of the specimen and local atomic variations and structure can be easily resolved by indexing and comparing NBED patterns acquired at neighbouring probe positions. The pattern recorded in NBED is similar to the ones observed in SAD[18], and this is illustrated in Figure 1-6 (a).

As mentioned above, larger convergence angles form CBED patterns. The reduced probe size results in better real-space resolution. However, the trade-off is decreased precision in reciprocal space, since the disks becomes larger and start to overlap[17], as can be seen in Figure 1-6 (b). Ideally the convergence angle must be limited to a maximum Bragg angle θ_B to avoid the overlap of adjacent diffraction disks, or in other words, the crystal periodicities need to be smaller than the diameter of the incident electron beam[20].

In the analysis of CBED patterns, there are two ways to study the orientation of crystalline materials: fitting Kikuchi lines when the sample analysed is thick or indexing the diffraction disks for thinner specimens. The former method is in general more precise due to the sharpness of the lines but it can lose accuracy for regions with deformation where the intensity becomes imprecise[17]. Another advantage of using CBED patterns is that thicker specimens can be used since they result in more dynamical scattering effects[1]. One challenge in the use of CBED is that this technique is very susceptible to hydrocarbon contamination, due to the focussed electron beam, which compromises the resolution of dynamical details[16].

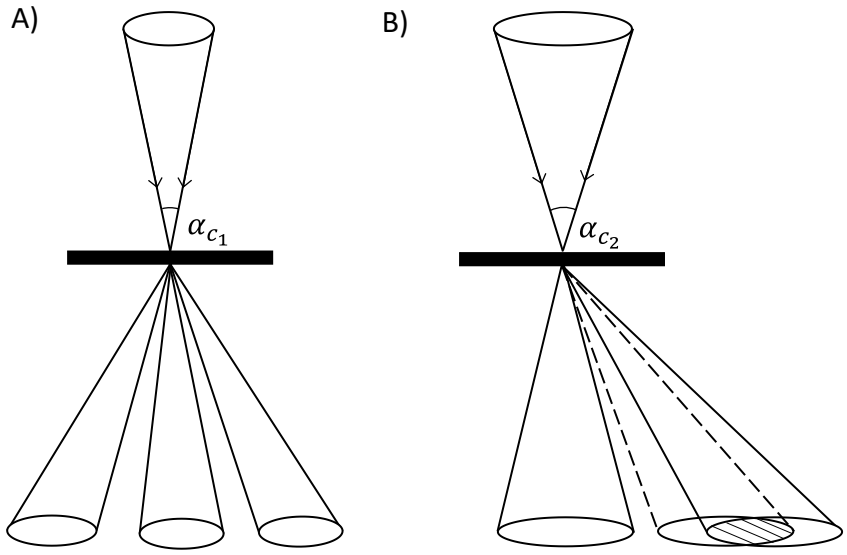

Figure 1-6 Diffraction disks from different convergence angles in the electron microscope. a) Small convergence angles generate non overlapping disks. b) If the convergence angle is progressively increased the disks start to overlap.

1.4 Common crystal structures of metals

The most common structures in solid metals are the body-centered cubic (BCC), face-centered cubic (FCC) and hexagonal closed packed (HCP) structures[21]. Bcc is a cubic structure with atoms at each corner and one atom at the center of each unit cell. They form a non-close packed structure because the atoms at the edges are only in contact with the central atom but are not in contact with each other. Thus, the BCC atomic packing fraction, i.e. the fractional volume in the unit cell filled by spheres is 0.68 - and the coordination number (i.e. the number of first nearest neighbours) is 8. Examples of materials with BCC structure are W and Fe[22,23].

Fcc is a cubic structure with atoms at each corner and at the centre of each face in the unit cell. Because the atoms at the corners are in contact with the atoms at the adjacent faces, they form a close-packed structure. Examples of bulk materials with FCC structure are Au, Ag and Pt[24,25]. Materials with HCP structures, such as Ti and Co[26,27], have a hexagonal unit cell.

Both FCC and HCP have a packing fraction of 0.74, i.e., the spheres fill 74% of the cubic volume, and a coordination number of 12.

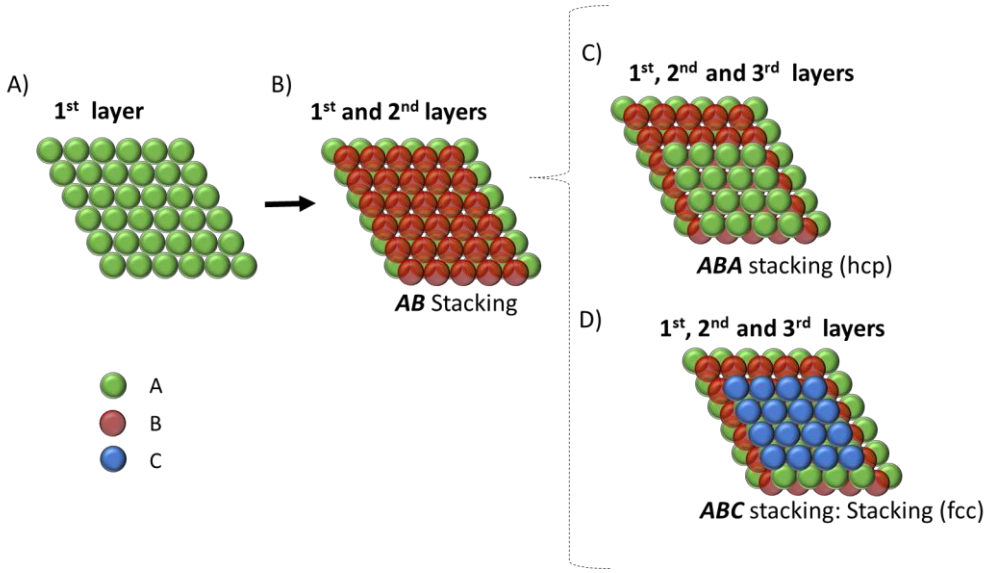

Figure 1-7 Stacking assembly of the most common closed packed structures, FCC and HCP. a) The first layer is organized in a hexagonal pattern, with each sphere being surrounded by six nearest neighbours. b) The second layer on both structures is slightly shifted with respect to the first and lies in the hollow sites of the layer below. c) The third layer in HCP structures lies exactly above the first layer. d) On the other hand, in FCC, the third layer is also shifted, and it lies in the hollow sites of the second layer.

Figure 1-7 shows the stacking arrangement in FCC and HCP structures. In a monolayer, the closest assembly of spheres is intuitive, and can be observed when a set of spheres are in contact, and the arrangement forms a hexagonal structure in plane[28] (Figure 1-7, a). In close packed structures the next layer is stacked in order to minimize space and therefore it is shifted with relation to the bottom layer such that the spheres in the second layer sit in the hollow sites of the first layer (Figure 1-7, b). The third layer defines the packing structure: in the hexagonal close packed structure (HCP) this layer will match registration of the first layer, whereas in FCC structures the third layer sits in hollow sites of the second layer that are not directly above the first layer. The resulting stacking order repeats every two layers for HCP and three for FCC, where the stacking orders are referred to as ABAB and ABCA respectively.

1.5 Thesis outline

This thesis is structured as follows: Chapter 1 provided a general introduction. Chapter 2 introduces the main concepts of electron tomography and the 4D-STEM technique. Chapter 3 presents experimental results obtained from the application of these techniques in the investigation of the formation of chiral shapes in tellurium nanoparticles. Chapter 4 presents electron tomography experiments from gold polymer grafted superlattices to investigate their 3D-lattice structure. Chapter 5 covers the investigation of Au bipyramidal nanoparticles produced by seed-mediated processes. The investigation of the morphologies of these nanoparticles, was also performed through electron tomography and a model that simulated their shapes from the geometry of their cross-sections. Finally, chapter 6 presents the conclusions of the thesis and outlook. Supplementary information is provided in appendix A.

2 Principles of Electron Tomography and 4D-STEM microscopy

This chapter introduces the basics concepts associated with the two techniques used in this thesis for the study of materials: STEM tomography and 4D-STEM techniques. The structure of this chapter is as follows: Section 2.1 gives an overview of the field of electron tomography. Section 2.2 describes the experimental procedure used to acquire a tomography series in the electron microscope and the main challenges that need to be confronted to obtain a dataset that will result in a good reconstructed volume with minimum artefacts. Section 2.3 present the main methods and algorithms used for the alignment which represents, the most critical task to achieve a satisfactory tomography reconstruction. The mathematical theory of tomographic reconstructions is covered in the Section 2.4. Section 2.5 is a more comprehensive section, where the mathematical concepts previously presented are applied to the most used reconstruction methods. Section 2.6 presents the resolution of an electron tomography dataset. Section 2.7 shows the main problems and experimental errors associated with the final reconstruction. Finally, section 2.8 presents the main concepts related to the 4D-STEM technique.

2.1 STEM tomography

Tomography is a wide field that is comprised of any technique that uses penetrating waves to acquire images at different angles of orientation and therefore reconstruct a volumetric object from these projections. The single projections from the reconstructed volume are called *slices*, and while the 2D-projections are constituted from *pixels,* the volumetric object (3D) is composed of *voxels.*

The tomography technique has its origins in the mathematical concept proposed by Radon (1917)[29], who showed how a 2D function can be retrieved from its 1D projections. Since this theorem can be applied to higher dimensions, one of the first applications of this concept was x-ray tomography, where images of an object are acquired at different angles by rotating an x-ray source and detector around the object. X-ray tomography is an efficient and non-destructive method which is routinely used in medicine to visualize the interior features within the human body, such as bone, leading to precise medical diagnosis[30].

Although x-ray tomography is the most popular application of tomography, there are many other types[31], including microwave tomography[32], neutron tomography[33], muon tomography[34], etc. – since the principles of tomography can be applied to many different types of probe.

The main focus of this thesis regards the application of electron tomography[35] , which is a powerful tool towards generating a complete volumetric description of the structure of nanomaterials and biological components. Electron tomography is an advantageous technique when compared with regular TEM imaging, where material information is only acquired in 2D, leading to ambiguity in the interpretation of the 3D shapes of nanoparticles[36].

Moreover, one of the main benefits of electron tomography is that it can lead to the reconstruction of volumes with atomic resolution[37–39]. This is achieved despite some drawbacks and hurdles of STEM tomography which include specimen damage caused by scanning the high energy, condensed electron beam across the specimen which can cause structural changes, specimen shrinkage and loss of material[29]. Also, due to the highly focused beam, carbon contamination growth can build up during data acquisition, compromising the quality of the final reconstructed volume[40].

2.2 STEM tomography data acquisition

2.2.1 Single tilt acquisition and the missing wedge

The most common method used for electron tomography data acquisition is the single-tilt technique since it is one of the most convenient ways to acquire the data and it has the simplest geometrical approach for reconstruction. In the particular case of the electron microscope, the sample holder rotates around the eucentric single axis, denotated as the Cartesian x-axis and projections are acquired at each of the tilt angles[29] which make up the dataset; this is called a tilt series. According to the mathematical theory underpinning tomography reconstructions, a volumetric object can be completely and perfectly retrieved when the set of angles in a tilt series is acquired over the entire angular range[29], i.e. from -90° to 90°. However, this is not possible in a conventional STEM single tilt acquisition (Figure 2-1), since the side of the holder or the mesh of the TEM grid start to obstruct the electron path and thus shadow the features of interest at high tilt angles[41]; this limits the feasible angular range of around -75° to 75° in a conventional STEM tomography experiment.

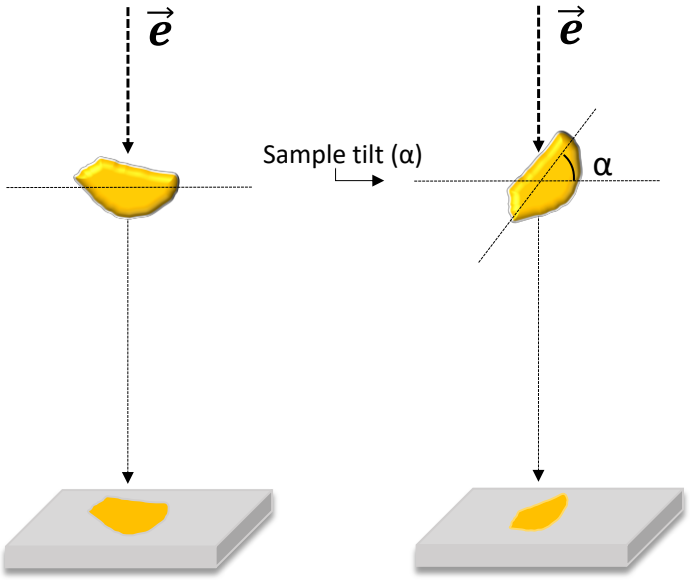

Figure 2-1 Scheme of an electron tomography series acquisition with a single-axis tilting. The object is rotated through a range of angles (α) and around a single fixed axis, where each projection is recorded. A typical electron tomography series is taken in the range ±75° in 1-2° increments.

Therefore, there is a region along the beam direction (*z*-axis) where the volume is left unmeasured during the data collection, termed as the *missing wedge* (Figure 2-2). This region of missing information results in distortion of the shapes and intensities of the reconstructed features[42] – mainly causing blurring and elongation of the objects along the *z*-axis. These problems are a big inconvenience in electron tomography datasets since they add complications and ambiguity to the interpretation of structures.

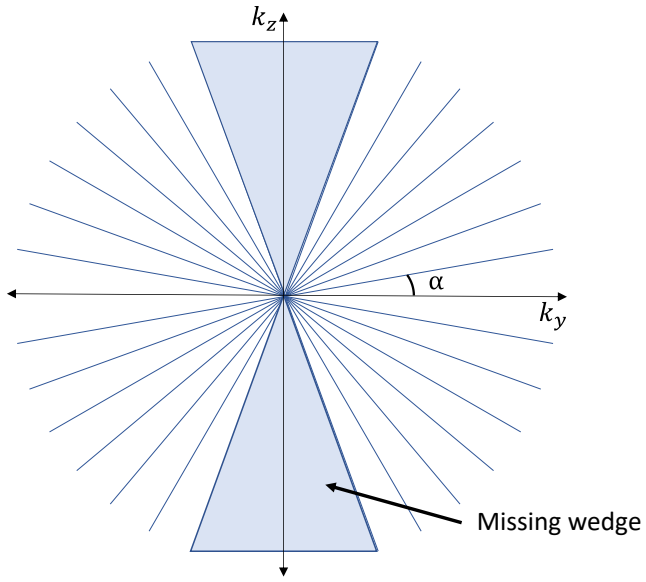

Figure 2-2 The missing wedge in the sampling of an object in the Fourier space.

One of the experimental strategies to minimize this problem in the single tilt setup is to choose more suitable TEM grids for the electron tomography experiments, i.e. ones with lower mesh density and appropriate geometry. Grids with low mesh densities, i.e. larger grid squares, such as 100-200 mesh have shown good promise for this purpose as well as geometries such as hexagonal grids. In order to obtain data from a larger range of tilt angles, it is necessary to choose features of interest in the samples that are located near the centre of the grid. Another good practice to improve the tilt range during the data acquisition is to load the TEM grid with their square sides at 45° with respect to the x-axis, so the grid square diagonals are perpendicular to the rotation axis, thus creating a wider area without the shadowing from the TEM grid. Using these strategies, it is possible to increase the range of feasible tilt angles to ±75˚.

Obviously, these experimental practices only improve the tilt range to the limits set by the inherent missing wedge, due to the mechanical and geometric limits of the microscope. To effectively improve the acquisition of information in ranges outside the conventional single-tilt limits, the dual-axis acquisition technique may be used, which allows for complementary data acquisition along two orthogonal axes[43]. In the dual-axis method, the grid is rotated 90° with

relation to the orientation of the first acquired tilt images set, resulting in a reduction of the missing wedge to a missing pyramid[42]. The tomograms are afterwards aligned with each other through 3D linear operations. The inverse 3D Fourier transform of these tomograms are then combined to form the final reconstructed object[42]. The downsides of this method are that the sample is exposed over a long period to the electron beam which makes it more susceptible to beam damage and also that the alignment step of the tomograms can introduce a fair amount of complexity to the reconstruction process.

Another solution that completely solves the missing wedge problem is the use of samples with a cylindrical geometry, such as a tungsten needle[44]. A sample with this symmetry allows access to the full range of tilt angles, however their fabrication still remains very challenging since tomography experiments require the milling of tips with perfect cylindrical symmetry and with apex radii on the order of nanometers.

Another artefact that comes from the electron tomography geometric setup is the increase in the specimen thickness with increasing the tilt angle[45]. A sample with thickness of 100 nm, for example, will be 2.9 times thicker when tilted at 70˚ - than when the sample is normal to the beam[36] – and this will degrade the image contrast due to multiple electron scattering signals.

Moreover, during the acquisition of series it is important to ensure that the electron microscope is well aligned and also that the stage is in the eucentric position, so when the holder is rotated around the x-axis, the sideways movement of the sample across the projection screen is minimized.

2.2.2 Automatic tomography acquisition

During electron tomography acquisition the microscope parameters need to be constantly adjusted and compensated according to the tilt angle. These corrections need to be precisely controlled in order to obtain a tilt series that will result in reasonable reconstruction. Therefore, although manual acquisition is feasible - and it has been done in the past[46] - the quality of the image series is critically dependent on a level of automation in the data acquisition, since manually tuned parameters are influenced by subjective errors from the microscope operator. Also, manual acquisition can be unsuitable for electron beam sensitive samples, since manual operation tends to be much less efficient and slower than automatic algorithms[47].

Automatic tomography acquisition can be performed by software developed in the academic domain (e.g. SerialEM[48], EMACT[49]) and commercial software (e.g. Thermo Scientific Tomography, Hitachi 3D tilt image acquisition)[47]. These softwares provide tools to automatically correct and compensate parameters during acquisition, such as translational shifts in the sample position (when the eucentric height is not accurate) or changing the focus, while deflecting the beam during these tasks, to prevent over exposure and beam damage[47].

Typically, the algorithms for these tasks use cross-correlation methods to track the features of interest while the sample is tilted during data collection[43] .

All of these tomography acquisition softwares rely on a microscope with good alignment[47] and proper parameter input. In general, a tomography experiment is quite time consuming, taking from 2 to 3 hours to be completed - beyond the time spent for STEM alignment.

2.3 Electron tomography series alignment

All the reconstruction algorithms assume that the projections represent slices from a 3D object rotated around a unique axis[50]. However, mechanical limitations and instability in the sample holder, result in shifts, rotations and potentially changes in magnification of the projections during acquisition of the tilt series. These will lead to blurring or smearing of the reconstructed objects[41] and therefore they need to be corrected prior to reconstruction.

In general, in order to obtain a well aligned tomography series it is important to: i) determine the direction of the tilt axis, ii) perform rotational, and iii) translational corrections[51].

The tilt axis direction can be determined by considering that the object of interest should follow a path that is perpendicular to the tilt axis in a single-axis geometry – and this can be checked by summing the entire set of images and verifying if there is an angle with the horizontal in the resulting image[52].

The most basic methods to align a tomography series are based on cross correlation, center-of- mass and the fiducial marker method.

The cross-correlation method measures the similarity between two subsequent images pixel by pixel and is generally used for coarse and translational corrections[53]. The distance between the correlation result center (which represents zero shift) and the correlation result maximum gives the lateral misalignment between the images. When performing the cross-correlation alignment, in order to detect the feature of interest in all the projections it is necessary to correct stretching in the image in the direction perpendicular to the tilt axis by $\frac{1}{cos\alpha}$, where α is the tilt angle between two consecutive projections[51]. Disadvantages of the cross-correlation technique are that a successful alignment is only obtained when the object has well defined density and high contrast in the image[36].

The center-of-mass technique calculates the lateral shift of each projection through its intensity center of mass. As such this technique is most relevant where the pixel intensities in each image are meaningful, as is the case for metal nanoparticles in HAADF-STEM.

It is common to use the cross correlation and/or center-of-mass techniques for the initial coarse alignment and then, if fiducial markers are available, the fiducial marker method for fine alignment.

In general, the fiducial marker technique consists of depositing gold nanoparticles of suitable diameter on the sample prior to the tomography experiment. The advantage of using fiducial markers is that the gold markers can be easily identified with subpixel precision due to their spherical shapes and they exhibit high contrast in ADF-STEM images even at high tilt angles. Also positional errors on individual markers can be averaged out when a large number of markers are used [54]. The gold nanoparticles need to have small sizes in relation to the image field-of-view used such that their center can be identified in each projection, but they have to be large enough to be detected in the images. Normally the sizes of the markers vary from 5-20 nm[55] and good alignment is possible using 8-10 markers. Disadvantages of this method are that sample preparation can be challenging when the markers interact with the substrates and agglomerate. This simultaneously makes it difficult to find regions of interest with enough markers and subsequent identification of single nanoparticles in each frame. Moreover, the detection of each marker in each frame can be very time consuming and the markers can interfere with the reconstruction causing artefacts.

The fiducial alignment works by building a 3D model that uses the 2D coordinates of the fiducial markers in each projection. Once the coordinates of the projections from the 3D-model are calculated, they are compared with the coordinates of the markers in the 2D projections. Final alignment is achieved by solving an optimization problem that consists of

computing the corrections for the translation, rotation and magnification that minimize the residuals between the coordinates and the model[29].

As mentioned above, some electron tomography series cannot be aligned using fiducial markers or cross correlation methods. For these series, one option would be to apply the common lines method[53]. This technique is applied for single-tilt series, and makes use of the Fourier Slice theorem, which will be presented in the next section, to find the common lines for each projection and therefore the whole stack is aligned to a common axis. However, this method only works well for free-standing objects with defined boundaries and with low noise in the vicinity of the object[53].

2.4 Mathematical background in tomography reconstruction

In order to understand the principles of a tomography reconstruction it is important to introduce two fundamental mathematical concepts: The *Radon transform* and the *Fourier Slice theorem.* These two concepts are introduced here for two-dimensional objects since it is easier to assimilate the reconstruction mechanism. Thus, in general terms, the *Radon transform* is built on the geometric problem of sampling projections of a 2D object at different orientations and calculating the corresponding 1D line profiles. The *Fourier Slice theorem* states that the Fourier transform of a projection from an object at a determined angle (Radon transform) is a central slice with the same orientation through the 2D Fourier transform of the 2D the object[52]. This formulation is the basis of all reconstructions algorithms and will be presented in detail in this section.

2.4.1 Radon transform

Consider a function $f(x,y)$ that describes an object in the Cartesian plane. Each point (x,y) can be projected onto a reference system orientated at the direction determined by the angle θ with respect to the x axis (Figure 2-3). The integrals along all possible lines that are perpendicular to θ form a projection curve that can be written as the line integral function $R_\theta(\theta,t)$:

$$R_\theta(\theta,t) = \int_{(\theta,t)} f(x,y)ds \tag{2.1}$$

Where θ and t are shown in Figure 2-3 and s is the coordinate perpendicular to t. The only region that needs to be integrated is the portion inside the object, the equation (2.1) can be rewritten using the delta function as:

$$R_\theta(\theta,t) = \int_{-\infty}^{\infty}\int_{-\infty}^{\infty} f(x,y)\delta(xcos\theta + ysin\theta - t)\,dxdy \tag{2.2}$$

$R_\theta(\theta,t)$ is the Radon transform of the function $f(x,y)$. The Radon transform is often called a *sinogram* since the curves obtained from objects located away from the axis of rotation follow a sinusoidal shape. The discrete Radon transform of a three-dimensional object is the equivalent to the experimental case in which 2D projections are taken at different angles.

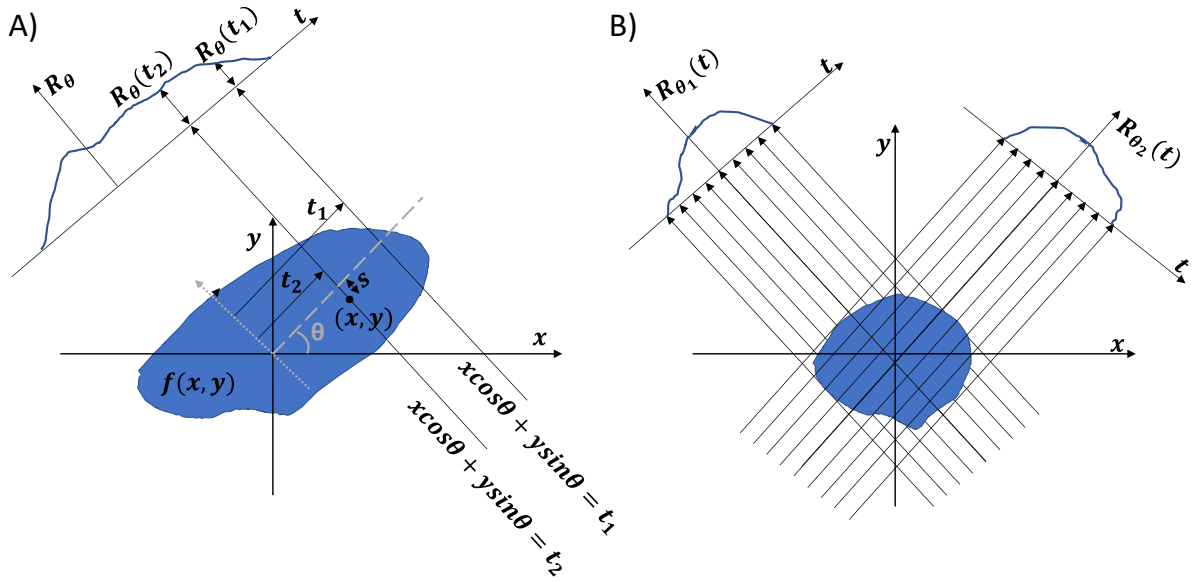

Figure 2-3 Schematic showing the concept of a Radon transform. A) A 2D object in a Cartesian xy system and its projection at angle θ. Each point of the projection curve (Radon transform) is formed by the line integrals taken within the object and along lines ($t1, t2$ ...) that are perpendicular to θ. B) Radon transforms taken at different θ. Adapted with permission from Pan S.X. and Kak A.C[56]. Copyright 1983 IEEE.

2.4.2 Fourier Slice Theorem

The Fourier slice theorem (or projection theorem) states that the 1D Fourier transform of the Radon transform of an object will result in a central slice in the 2D Fourier transform space of the object[36] - where this slice crosses the origin and is oriented by the same angle θ (Figure 2-4). This can be represented algebraically as:

$$F_{1D}[(R_\theta(\theta, t)](\omega) = F_{2D}[f(\omega cos\theta, \omega sin\theta)] \quad (2.3)$$

Where ω is the spatial frequency in Fourier space. Therefore, the slice of the object can be recovered from taking the 2D inverse Fourier transform. When a set of projections are

taken at different angles, they will form radial lines in Fourier space and the whole frequency series will enable full retrieval of information about the 2D shape of the object in real space.

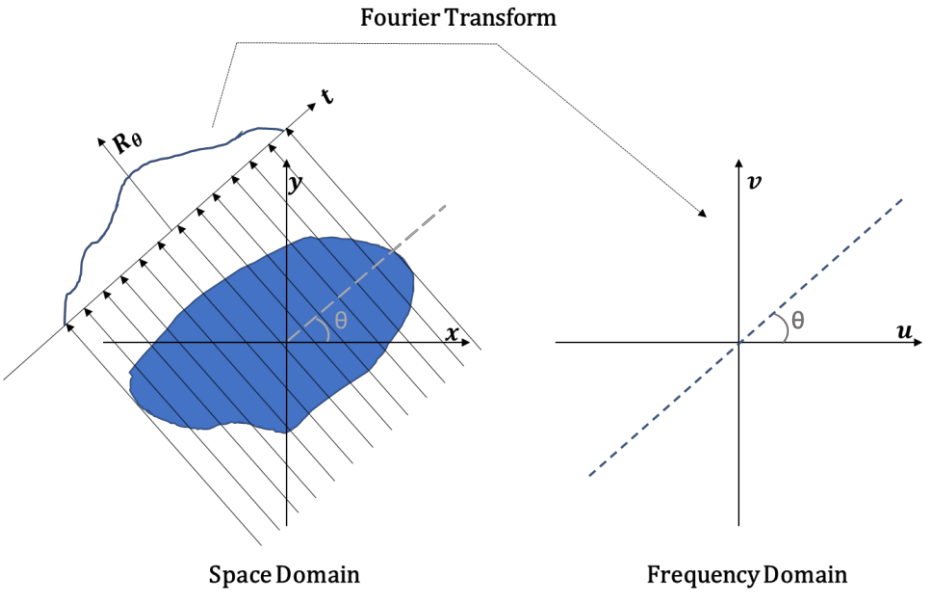

Figure 2-4 Schematic of the concept of the Fourier slice theorem. A projection of a 2D object in real space is converted to a line (1D) projected density. The 1D Fourier transform of the projection results in a central slice of the 2D Fourier transform of the original object. Adapted with permission from Pan S.X. and Kak A.C[56]. Copyright 1983 IEEE.

Thus, in a tomography reconstruction, the discussed concepts are valid for objects in 3D spaces with 2D projections. Each Fourier transformed image will form a plane in the 3D Fourier space of the object and all planes will intercept a central line (Figure 2-5). This central line has the same direction as the tilt axis and is commonly referred to as the *common line*[53].

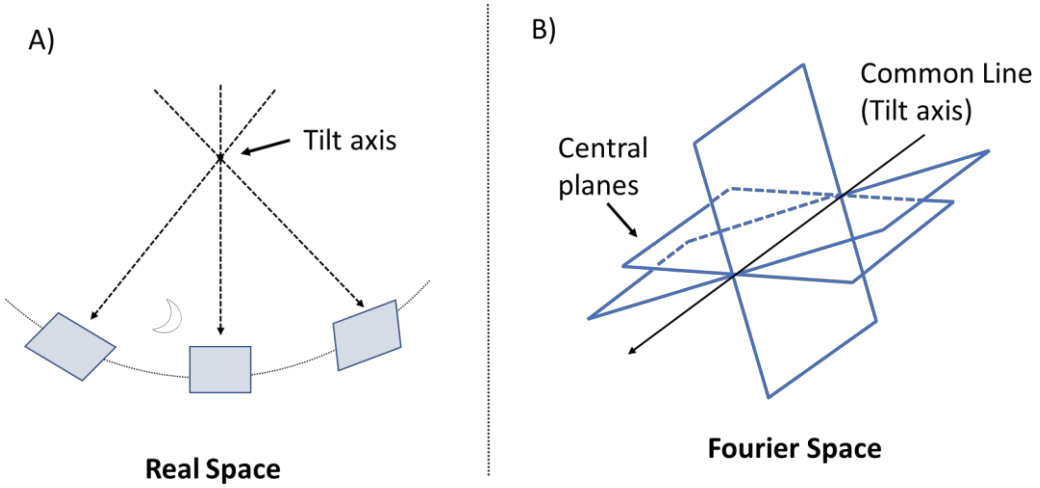

Figure 2-5 Projection theorem applied in a tomography experiment. A) Real space 2D-projections B) The intersection of the planes forms the common line and has the same direction of the tilt-axis of the series. Adapted with permission from Liu et al.[53]. Copyright 1995 Elsevier.

2.5 Reconstruction methods

In this section the most common procedures for reconstruction from 2D projections of an object are presented. In general, the reconstruction techniques are based on one of two methods: i) Fourier reconstruction, which is based on solving the reconstruction by the inverse Fourier transform and ii) direct methods in which the reconstructed 3D volume is calculated in real-space[29].

Any reconstruction method will have intrinsic imperfections, and although the alignment of the tilted image series is the most critical step for a satisfactory reconstruction, the final result will always contain artefacts regardless of the quality of the performed alignment.

2.5.1 Direct Fourier reconstruction

The Direct Fourier reconstruction method is a straight application of the Fourier Slice theorem in 3D[57]. As mentioned previously, taking 2D projections of the object over the full tilt range would be analogous to obtaining Fourier slices over the entire tilt range - and the 3D Fourier inverse transform would be able to retrieve the volumetric object[41]. However, the missing wedge is one of the factors that compromises the application of this method. Another big issue is that the inverse Fourier transform is not easily implemented due to the discrete nature of the tomography data, which is typically acquired at angles of equal increments[58]. The inverse Fourier transform requires an interpolation from polar to Cartesian coordinates (Figure 2-6), and there is no fast or direct method for this interpolation[59]. These problems make Direct Fourier methods difficult to implement and computationally intensive – and therefore less popular than the more efficient back-projection based methods[52].

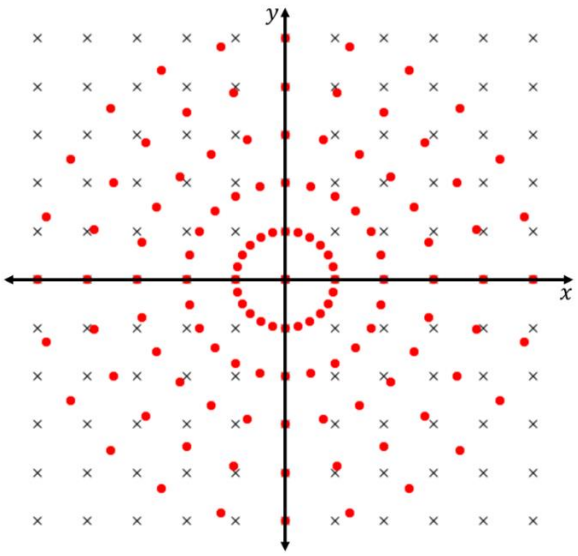

Figure 2-6 Superposition of polar (red dots) and Cartesian (black dots) coordinate systems. A tomography reconstruction with the direct application of the slice theorem requires an interpolation to convert the polar (experimental data) to the Cartesian (Fourier space) system, compromising the feasibility of this method.

2.5.2 Simple and filtered back projection reconstruction methods

The back-projection method is a real space technique that relies on the basic idea that the intersection of three lines will describe a unique point in the space – and more complex objects will need more lines to create a unique description of them[52]. Therefore, by inverting a sufficient number of projections the object may be retrieved. Basically, in the 2D case the 1D projections (Radon transform) are projected back to generate a reconstruction of the object. The main drawback of the simple back-projection method is also related to the discrete nature of the experimental acquired projections. To achieve a reasonable result using this technique many projections are required to reduce the artefacts caused by higher sampling at low frequencies which is shown in Figure 2-6, where there are a higher density of polar coordinates around the axes origin. Since the low frequencies represent smooth features in the object and the high frequencies account for the sharpest details, the resulting image of the back-projection will be blurred due to increased contribution from the low frequencies. A high pass filter needs to be applied to solve this problem, this constitutes a *filtered back-projection* (FBP) or *weighted back-projection* (WBP). The filtered back-projection is the most widely used method in x-ray tomography and industrial applications[31] since it can be applied to data series with irregular sampling and it is also efficient at reconstructing large datasets[52].

2.5.3 SIRT reconstruction

Another common reconstruction method is the Simultaneous Iterative Reconstruction Technique (SIRT). A SIRT reconstruction consists of iteratively updating an original WBP reconstructed series by comparing its projections (obtained by the Radon transform) with the experimental projections and therefore minimizing the artefacts[60].

The SIRT technique is the most popular reconstruction technique after the WBP and it is known for being effective when applied to datasets with low noise and high contrast[36]. Also, this method requires a large number of projections to result in a good reconstruction.

It is difficult to predetermine the number of iterations to achieve an optimal reconstruction using the SIRT technique. Since the reconstruction is relatively time-consuming, a good practice to find the right number of iterations is to progressively increase the number of iterations and reconstruct only a subarea where the results can be examined[61].

2.6 Tomography resolution

The most critical factor that affects the resolution of a reconstruction from an electron tomography dataset is the missing wedge. However, as described in the previous sections, there are many other experimental factors that contribute to resolution degradation, such as sample drift in the microscope when acquiring data, large sample thickness, beam damage, microscope conditions etc[36]. There are also post-acquisition factors such as series alignment and the chosen reconstruction method.

It is possible to estimate the best resolution for a determined dataset, though. Therefore, assuming a perfectly aligned series, the resolution along the x-axis is given by the original resolution of the projection series. The discrete nature of the dataset reduces the y-axis resolution - the axis perpendicular to both the rotation axis and the beam direction– and an estimation for the resolution is[62,63]:

$$D_y = \frac{\pi D}{N_p} \tag{2.4}$$

where N_p is the number of projections and D is the final diameter of the reconstruction. Therefore, for a nanoparticle with 50 nm, to obtain a resolution of 2 nm along the y-axis, at least 75 projections are required[45].

For single tilt acquisitions, where the missing wedge is an issue, the z-axis direction has the lowest resolution. As a result all the tomography reconstructions will have elongations in this direction[36]. The resolution in this axis is given by[63]:

$$D_z = D_y . e_{yz} = D_y \sqrt{\frac{\alpha + \sin\alpha\cos\alpha}{\alpha - \sin\alpha\cos\alpha}} \tag{2.5}$$

where α is the maximum tilt angle and e_{yz} is the elongation factor. Acquisition of a tilt series within the range ±70˚ will result in an elongation factor of e_{yz} <1.3, and this is a suitable threshold to obtain reliable tomography results[36].

2.7 Reconstruction artefacts

2.7.1 Reconstruction artefacts from tilt angles range

The previous sections presented artefacts which limit the resolution of an electron tomography reconstruction. In this section, simulations with isolated artefacts are presented in order to give more instructive examples of the effect of these artefacts on the images. Since a tomography reconstruction is an inverse problem that yields a three-dimensional object from the 2D projections, an ideal reconstruction is obtained with a full range of angles and with small angular increment. All tomography reconstruction methods are sensitive to the number of projections.

A simulated rectangular lattice was used to simulate the effect generated by an inconsistent angular range on the reconstruction and is shown in Figure 2-7. Figure 2-7-b and c show near perfect reconstructions when an angular range of [-90˚, 90˚] is used and a step size of 1˚ and 2˚, respectively. When a reconstruction is made with the full range of angles but with lower number of projections, the reconstructed image loses resolution - although the overall shapes have no deformations; this can be seen in Figure 2-7-d, where the tilt series has an angular increment of 5˚. If the angular step is increased further to 10˚(Figure 2-7-e), the reconstructed image has a further decrease in quality of the resolution, although the overall form of the shapes in the image remain consistent. As a result, low intensity features cannot be seen anymore. Figure 2-7-f shows an extreme case, where the tilt series has a 20˚ angular increment and whilst the reconstructed object keeps its symmetry, the resolution is so degraded that the features are barely visible. In STEM tomography, typically step sizes between 1-3˚ give good reconstruction results.

When the reconstruction is made without the entire range of angles, there are artefacts that change the resolution and cause deformation of the object. Figure 2-8 c-e show the effects when the series angular range is reduced to [-75˚, 75˚], [-50˚, 50˚] and [-40˚, 40˚], respectively. The reconstructions from incomplete angular tilt ranges show a resulting image with missing information, where some regions of the edges are undefined. There is also deformation (elongation) of the objects and intensity artefacts - where intensities of corners in the object are too high and also darker intensity regions surround these features.

To make these effects more evident, they are also simulated using a head *phantom* image (Figure 2-9). A phantom image is a standard figure used in reconstruction examples, which had its origins in x-ray tomography as it simulates a human head – and it is composed of the superposition of 10 ellipses, where the artefacts can be easily noted. Therefore, a simulation

with a phantom image was performed using an angular range of [-40˚, 40˚]. The results show very pronounced elongations, missing information and distortions, as shown in Figure 2-9.

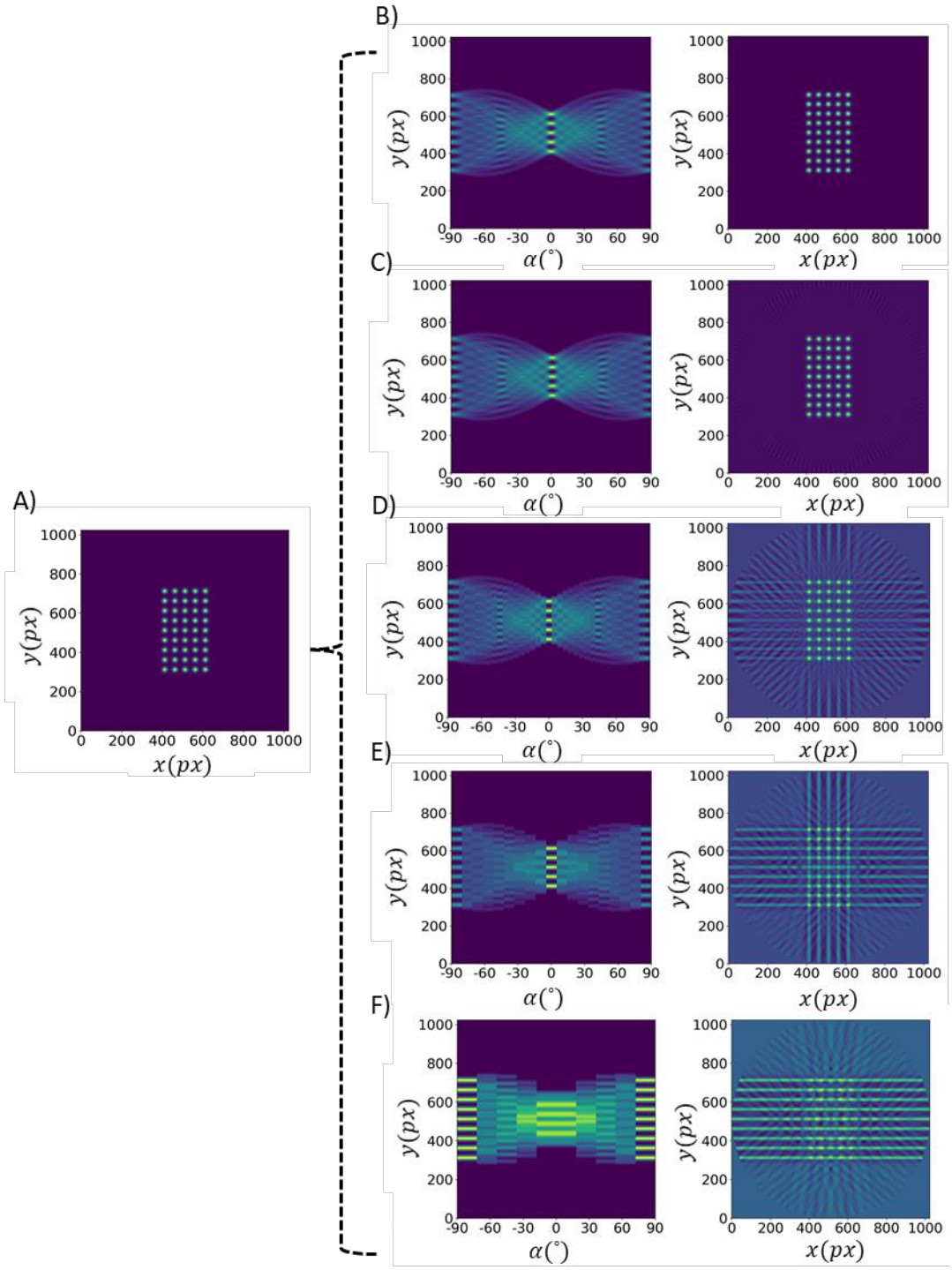

Figure 2-7 Simulations for the effects of discretization in the reconstruction of a rectangular lattice. (a) b) are the sinograms for a reconstruction over the angular range [-90˚,90˚] and with step of 1˚. c), d) e) and f) same angular range but with steps of 2˚, 5˚, 10˚ and 20˚, respectively.

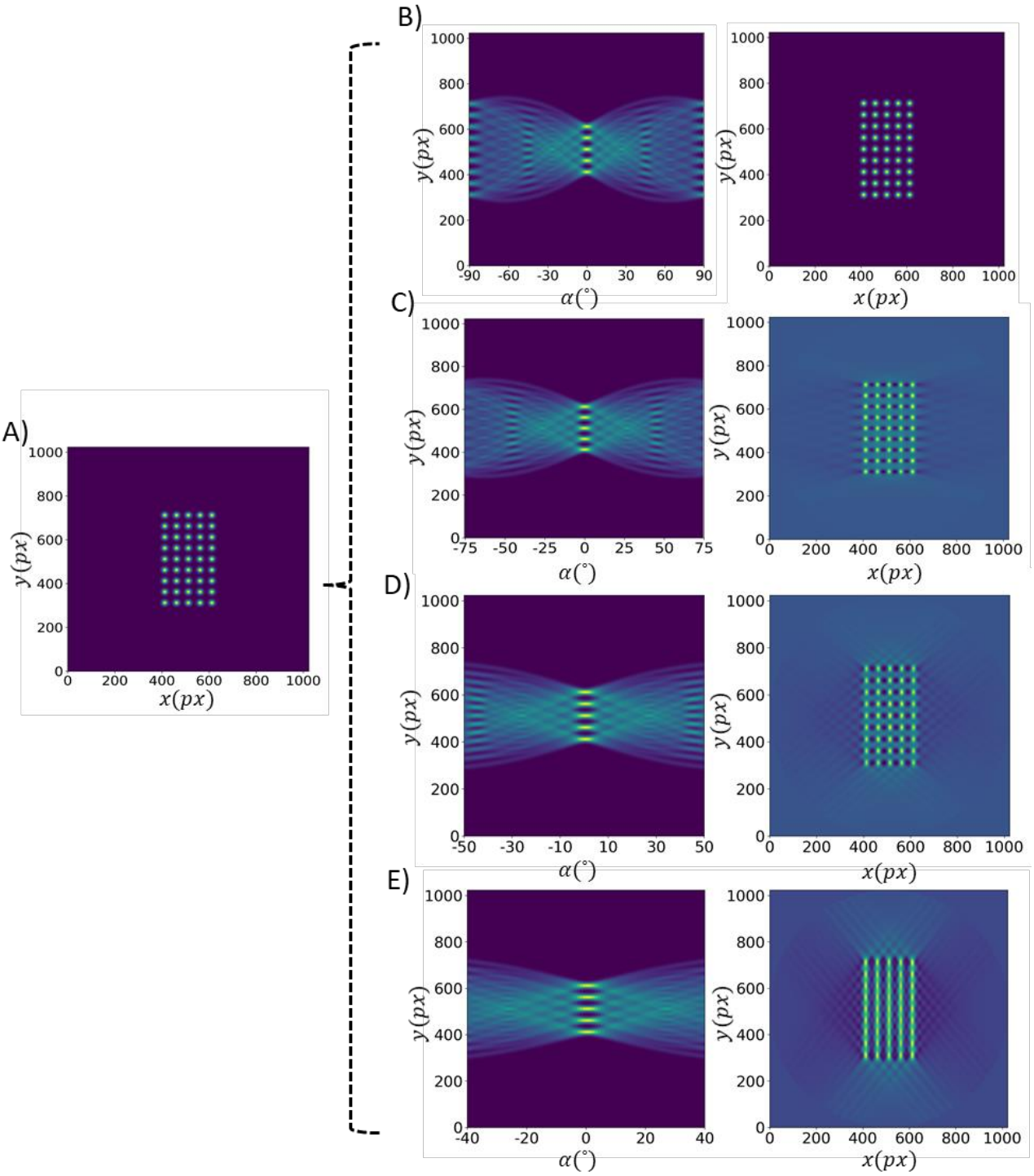

Figure 2-8 Simulations for the effects of reduced tilt range on the reconstruction. a) sinograms and b) reconstruction over the range [-90˚,90˚]. c), d) and e) same as b) but with ranges of [-75˚, 75˚], [-50˚, -50˚] and [-40˚, -40˚], respectively. All the simulations have a step size of 1˚.

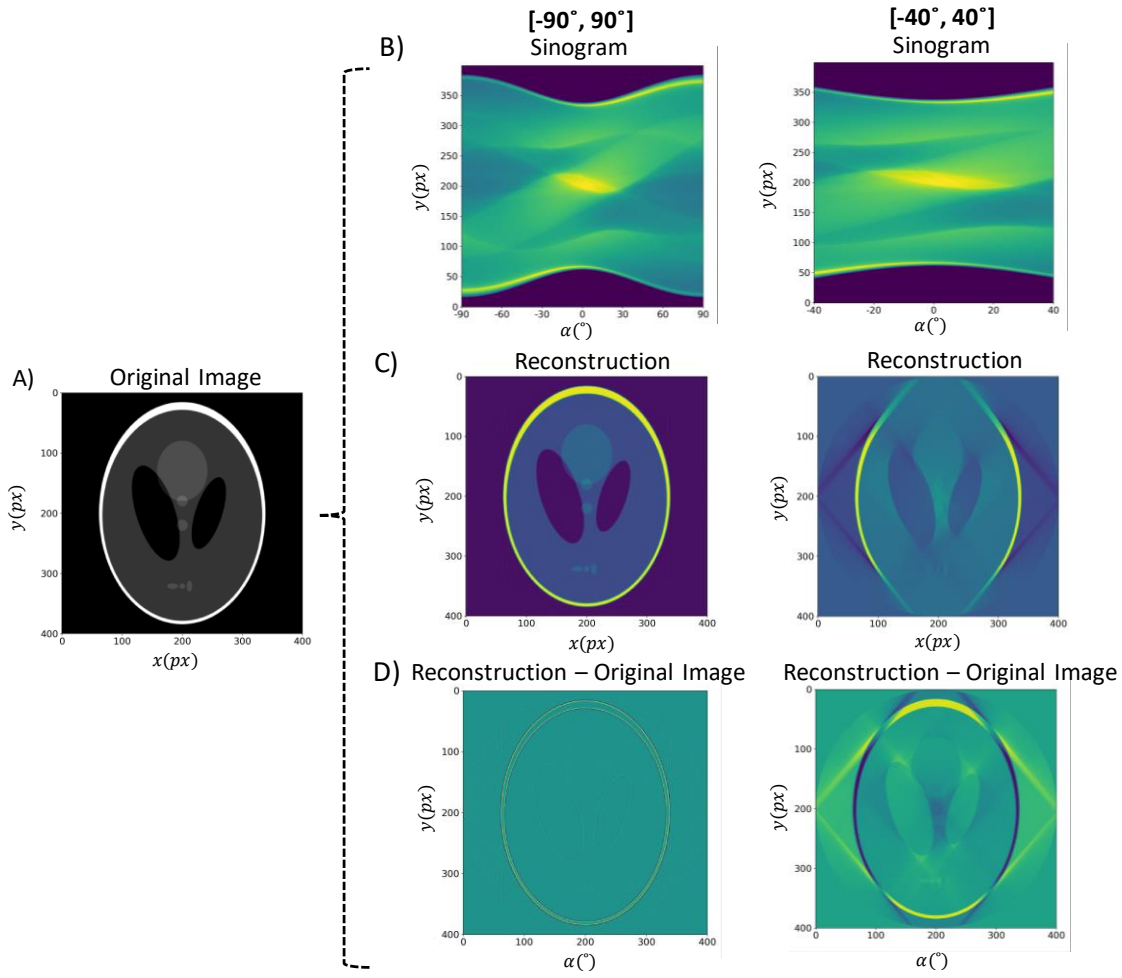

Figure 2-9 Simulations with a phantom image to evidence the distortions caused by using an incomplete angular range in the reconstruction. a) original image, b) shows the sinograms for a reconstruction in the range [-90˚,90˚] and [-40˚, 40˚], respectively. c) comparison of the reconstructions obtained from these angular ranges. d) the difference between the reconstructions and the original image. All the simulations have a step of 1˚

2.7.2 Reconstruction artefacts from errors in experimental parameters

As discussed in Section 2.3, the experimental errors present in STEM tomography can lead to diverse issues that contribute to misalignments, sometimes making the alignment a very challenging task. In this section some examples of misalignments, applied to a simulated rectangular lattice of atoms are presented.

One of the main issues in the alignment of a tomography series is that reconstruction algorithms, such as back-projection, assume that the rotation center is a horizontal line located along the center of the image. When the rotation axis is shifted from the center or is not orientated along a perfect horizontal line ($\theta_t = 0^{\circ}$) the result will be a reconstruction with artefacts. In the tilt series this can be perceived as an object that does not follow a vertical path over the stack. The reconstruction of such a series results in deformations such that a spherical object is reconstructed as an arc with an orientation that depends on the direction of the misalignment[52] - resembling a crescent moon (or the c-letter shape). Figure 2-10 shows these effects for shifts in different directions from the horizontal axis.

Due to mechanical imperfections in the microscope stage and possible miscalibration, another source alignment problems are systematic errors between recorded tilt angles and their real values[64]. To first order, the incorrect scaling of the angles can be represented by:

$$\alpha_m = e_s.\alpha + \alpha_{off} \tag{2.6}$$

Where e_s is the scale factor, α_m is the measured angle, α is its real value and α_{off} accounts for an angular offset. Figure 2-11 shows the case where the measured angles are 10% larger and smaller than their actual values with zero offsets. The effects of incorrect angular scaling can be observed at the borders of the reconstructed rectangles, where their shapes are also deformed and form arcs. The direction (in or out) of the arcs depend on whether the scale factor s is bigger or smaller than 1.

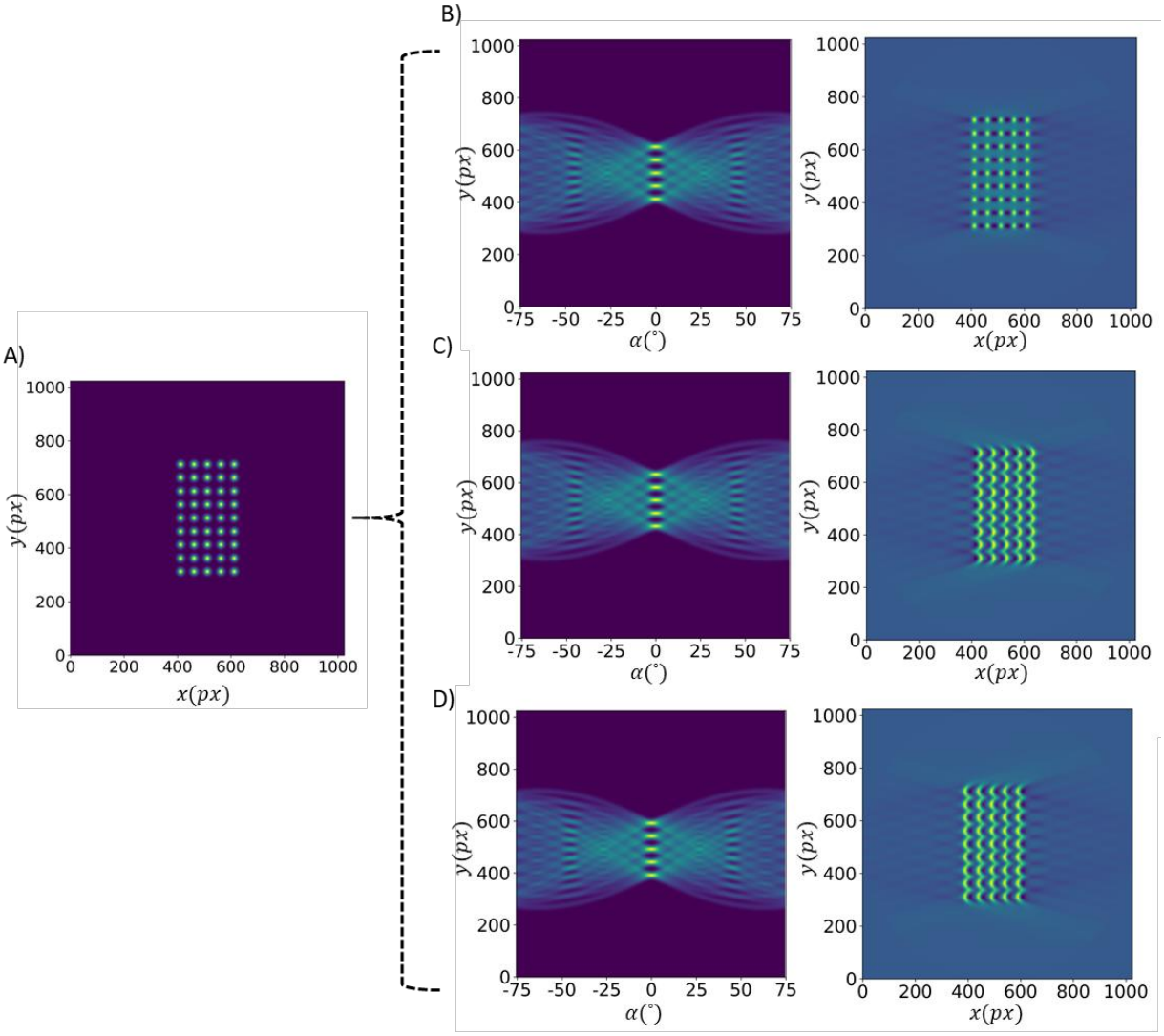

Figure 2-10 Simulations of a rectangular lattice showing misalignments of the tilt axis or scan distortions. a) original rectangular lattice, b) sinograms and reconstruction for tilt axis orientated at 0˚ and an angular range of [-75˚,75˚]. c) same as b) but with a shift in the tilt axis of -20 pixels from the central horizontal line. d) same as b) but with a tilt shift of +20 pixels from the central horizontal line.

An angular offset (Figure 2-11) will not introduce real artefacts in the reconstruction- although it laterally translates the center of the sinogram. An angular offset has only the effect of inducing a rotation of the reconstructed object with relation its original orientation.

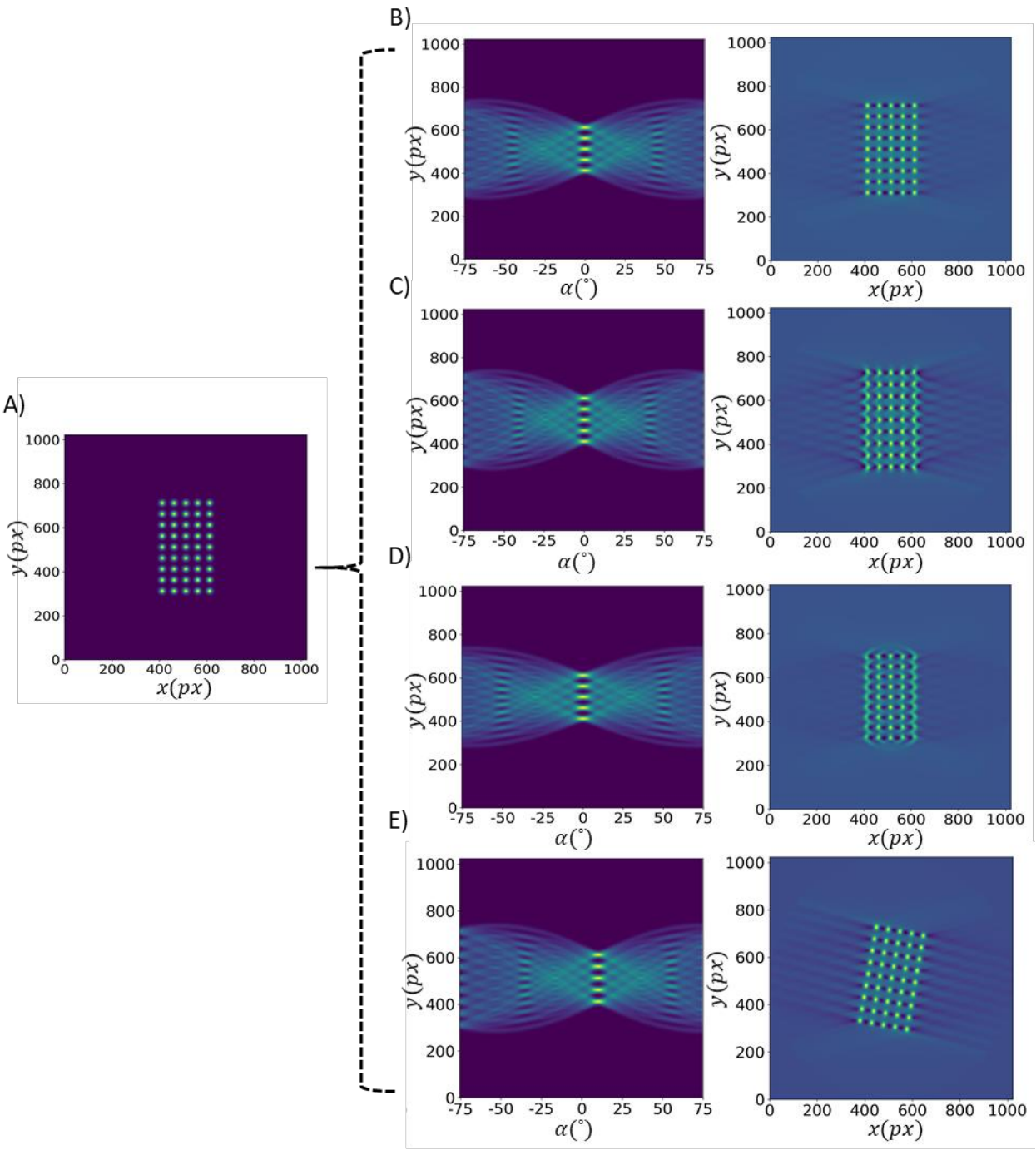

Figure 2-11 Simulations of a rectangular lattice showing incorrect angular scaling. a) original rectangular lattice, b) sinograms and reconstructed data for angles with correct scaling and over the angular range [-75˚,75˚]. c) same as b) but with an incorrect tilt scaling where the tilt angles are 10% bigger than their actual values. d) same as c) but the tilt scaling is 10% smaller. d) an angular offset (here exaggerated to improve the perception of the effects) will not introduce an artefact but rotate the object with relation to its original orientation.

Another typical experimental error in a STEM tomography comes from the use of the dynamic focusing during acquisition of the tilt series. Since tilting the sample results in different defocus values across the field of view (especially at high angles), the dynamic focus acts to keep the probe focused during the tilt series acquisition by changing the strength of the condenser lens at each scan line[65]. Defocus adjustment is required for each scan line instead of each pixel as the fast scan direction is typically parallel to the axis of rotation[66]. The defocus from the jth line to the next j'th is given by[66]:

$$\Delta z = (j' - j) d_p \tan\alpha \tag{2.7}$$

Where α is the tilt angle and d_p is the pixel size. Figure 2-12 is a schematic that shows this effect and the interpretation of Equation (2.7).

In the presence of misalignments in the objective lens rotation center, the sample will be shifted[1] in the y direction proportional to the beam misalignment angle (β) given by[67]:

$$\Delta y = \Delta z \ \tan\beta \tag{2.8}$$

Combining equation (2.8) with (2.7), results in the following shift:

$$\Delta y = d_p \cdot (j' - j) \tan\beta \tan\alpha \tag{2.9}$$

Figure 2-13 shows simulations for the case of $\Delta y = 0.05 \ \tan\alpha$, e.g. for the case that $S = d_p \cdot (j' - j) \tan\beta$ is constant and causes an error of 5% of the tilt angle in y.

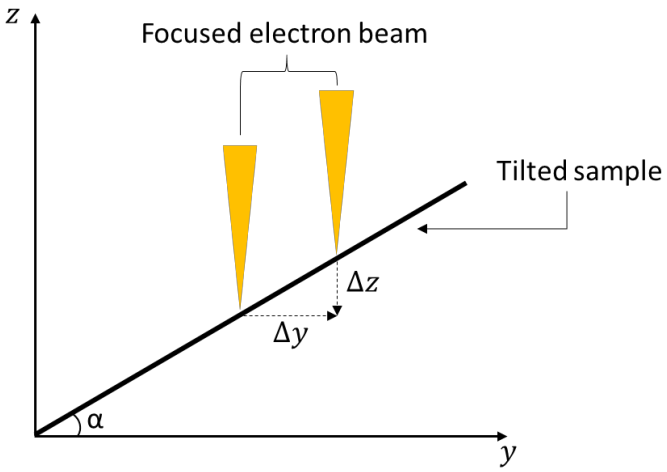

Figure 2-12 Defocus in a function of the sample position in a STEM microscope. Figure adapted from reference Feng at al[66].

The artefact caused by the dynamic focus in an experiment with misaligned rotation center can be partially corrected by scaling the angles in the sinogram. Although the optimal correction in the angles will have value of:

$$\alpha_{corr} = \alpha(1 - S \cdot \tan \alpha) \tag{2.10}$$

This value is normally not known a priori and needs to be found by inspection. Thus, the most efficient method to find it is performing the reconstruction for one slice and adjusting the scaling factor in the angles accordingly, until the artefacts presented in Figure 2-13 are minimized.

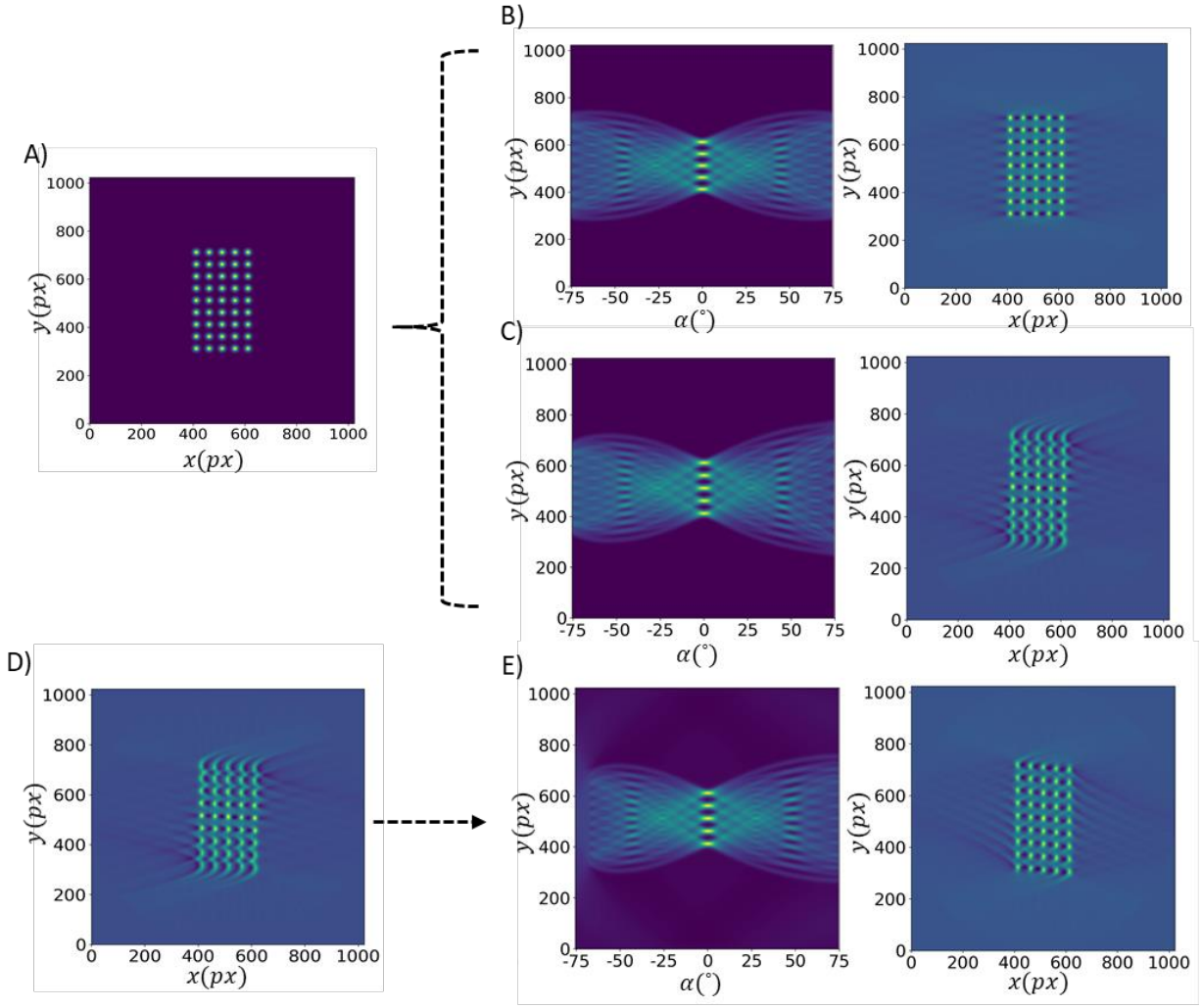

Figure 2-13 Simulations of a rectangular lattice showing the effect of error from automatic defocus in a STEM tomography. a) original rectangular lattice, b) sinograms and reconstruction for angles with no errors from the automatic defocus and over the angular range [-75˚,75˚]. c) same as b) but with an error $\Delta y = 0.05 \tan \alpha$, d) the incorrect reconstruction c) can be partially corrected e) by scaling the angles of the sinogram.

2.8 Four-Dimensional scanning transmission electron microscopy

Four-dimensional scanning transmission electron microscopy (4D-STEM) or *scanning electron nanodiffraction* (SEND)[68] is a position resolved diffraction technique[69] that consists of the acquisition of 2D diffraction patterns for each probe position (pixel) in a 2D-STEM raster scan, hence the name 4D-STEM[17]. Therefore, these experiments result in 4D data, composed

of two real space (x, y), and two reciprocal (k_x, k_y) coordinates[68] , as shown in Figure 2-14. In the context of this work, the 4D-STEM setup refers to a combination of an ADF detector with a pixelated camera**,** in place of a BF detector, as shown in Figure 2-15.

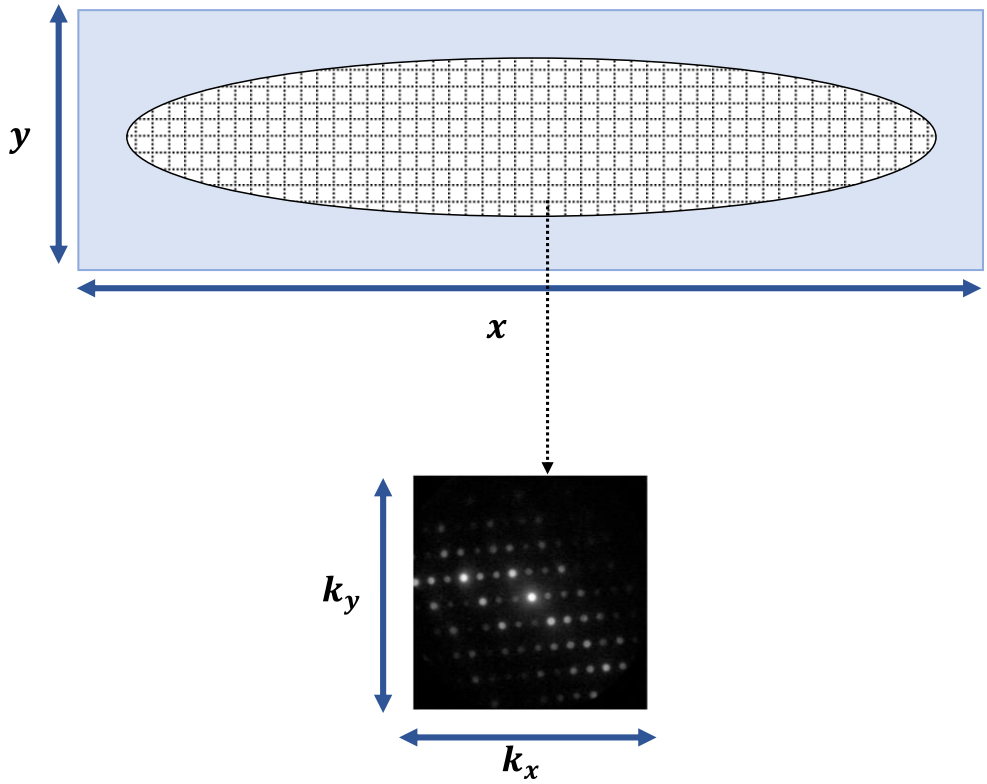

Figure 2-14 Schematic showing the data structure resulting from the 4D-STEM technique. A diffraction pattern image $(k_x \times k_y)$ is acquired at each pixel in the area of interest $(x \times y)$. The resulting data cube has dimensions $(x \times y \times k_x \times k_y)$.

The 4D-STEM technique may be used to create a map of the crystal orientations within materials, extracted from the combination of the real and reciprocal space images. The maps obtained from diffraction patterns are rich in fine details of the atomic arrangement and lattice parameters can be determined with high accuracy[70]. With 4D-STEM, the techniques mentioned earlier such as nanodiffraction, CBED, high resolution imaging and dark field electron holography[71,72] can be used to determine the strain in materials.

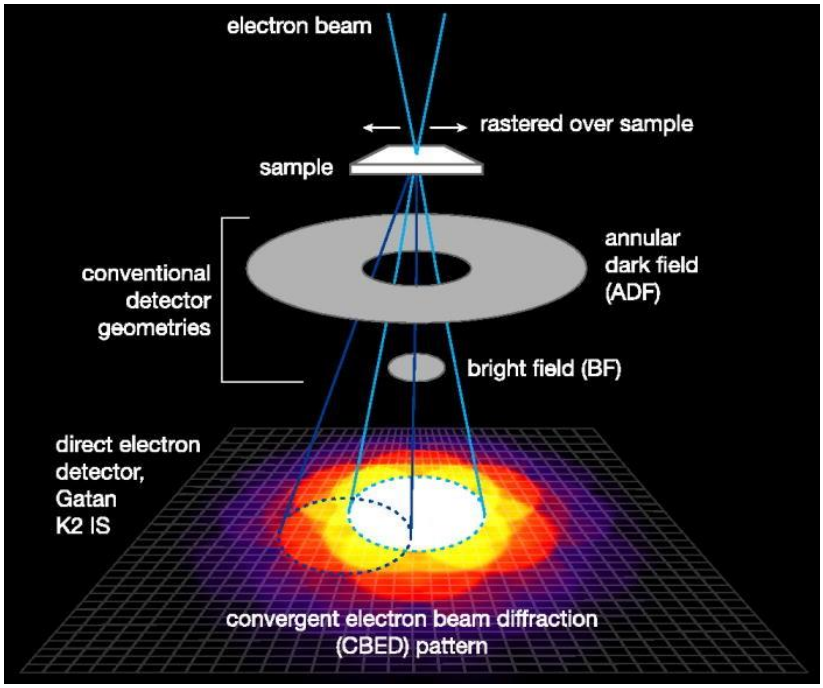

Figure 2-15 Schematic showing the 4D-STEM setup used in this thesis. A focused beam scans a sample and the signals are recorded by the ADF detectors, which record a single number per probe position. A pixelated camera replaces the BF detector and records a full CBED pattern for each probe position. Reprinted with permission from Ophus et al.[73]. Copyright 2017 AIP Publishing.

A recent review of the applications of 4D-STEM by Ophus[17] highlights the strengths of the technique. Precise lattice orientations can be determined from the recorded diffraction patterns which enables the high precision studies of material parameters, including grain orientations in metals and their changes under applied tension, local lattice structural change and misorientation, and strain mapping.

Some disadvantages of diffraction disk data are that the disk intensities are typically not uniform, which can make the accurate identification of their positions difficult. The spatial resolution can be improved when the convergence angle is increased, but, as discussed previously, it may cause the diffracted disks to overlap and also become more susceptible to non-uniform intensities[71]. Pekin et al[74], compared different correlation methods to estimate the measurement error due to nonuniform intensity of the diffracted disks. They concluded that prefiltering the diffraction patterns with a Sobel filter before performing cross-correlation or

performing a square-root magnitude weighted phase correlation returned the best results for disks which had internal structure. Another common issue is that 4D-STEM experiments result in large datasets, a gigabyte of data can easily be generated in under a minute[75]. The capacity to process big data with lossless compression is a challenge that has to follow the development of the field.

The analysis of 4D-STEM datasets will depend of the configuration of the experiment and the kind of diffraction patterns formed, so normally analysis tools are custom developed. However, there are some softwares available that can be used for analysis of such data, for example py4DSTEM[75]. Also computational tools developed to work with multidimensional data, such as HyperSpy[76], can be applied to analysis of 4D-STEM data.

2.8.1 Virtual dark-field (bright-field) reconstructions from the electron diffraction patterns

The diffraction disks in the data obtained through 4D-STEM experiments can be selected and combined in different ways; the resulting images are denominated as *virtual images*, and the combination of different disks may show different sample characteristics. A *virtual reconstruction* (VR) is a method that retrieves an object from the full set of diffraction images acquired in a 4D-STEM experiment. VR is performed by summing the intensities of the pixels within a selected region, for each diffraction pattern recorded at each probe position – and the region is limited by a digital *virtual aperture*[6], as shown in Figure 2-16.

The main advantage of VR is the versatility of selecting the features of interest from a full dataset, without the physical limitations in conventional TEM[7]. The virtual aperture can be customized according to the underlying crystal structure and can have any size and shape (e.g. circle, square, ring) defined by the user. Also, this technique is not limited to summing the

diffraction spots, but it is also possible to subtract the diffraction spots that obfuscate the features of interest.

Two types of reconstructions can be performed, depending of the region selected by the virtual aperture: virtual bright-field (VBF) or virtual dark field (VDF) reconstructions[6]. This is possible because each frame acquired by the CCD camera contains a complete set of disks: selecting the central disk (direct electron beam) will form a VBF, while selecting the diffracted disks will create a VDF reconstruction. However, it is important to note that the total signal is truncated by the data resolution – for example, an 8-bit image has 256 grey levels and therefore not all information can be retrieved[6]. Another drawback is that the images are susceptible to the distortions in the scanning beam.

The features present in these reconstructions are very similar to the ones in classical diffraction contrast TEM images. Therefore, these reconstructions can also be used for the analysis of crystallographic defects[6], as will be shown in chapter 3. The advantage of virtual reconstructions for this purpose is that different crystal features can be highlighted choosing the different diffraction disks, without the limitation of a physical aperture containing multiple and adjacent holes. Other advantages are that the virtual reconstructed images do not have their resolution limited by the size and lens aberrations. Also, virtual apertures can be customized and designed according to the underlying crystal lattice to optimize image contrast[7].

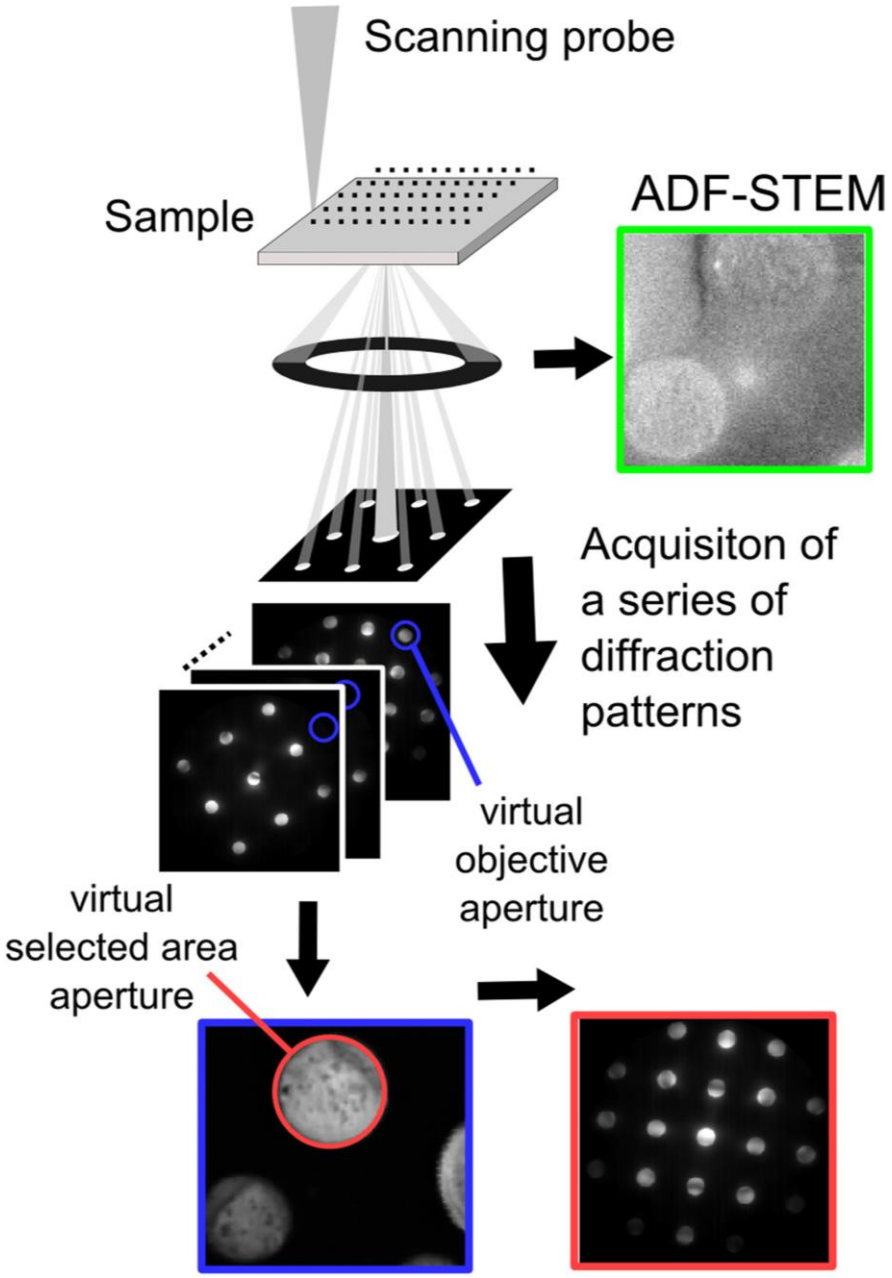

Figure 2-16 Schematic showing the virtual reconstruction technique in a 4D-STEM experiment. In addition to the ADF image, a diffraction pattern is recorded at each probe position. The sum of intensities within a virtual aperture (blue circle) can be calculated for each diffraction pattern and a dark-field image can be reconstructed. By selecting a certain area in the resulting image (red circle) and summing the corresponding diffraction patterns will result in a virtual selected area aperture. Reprinted with permission from Gammer et al[7]. Copyright 2015 Elsevier.

3 Electron tomography and 4D-STEM of chiral Te nanoparticles

This chapter presents electron tomography and 4D-STEM experiments of chiral tellurium nanoparticles as part of an investigation into crystal growth and polyhedral shape formation of these nanocrystals. The main result in this chapter demonstrates a new mechanism for the formation of chiral shapes without using chiral ligands, based on screw-dislocation-mediated growth. Section 3.1 gives an overview of the concepts of chirality and how it is inserted in the context of this work. Section 3.2 presents the results from the electron tomography datasets acquired for Te nanoparticles prepared under different conditions to investigate the role of the chiral ligands and the growth of these nanoparticles. Section 3.3 presents the 4D-STEM experiments performed on Te nanorods to explore whether evidence of screw dislocation mediated growth can be established. Finally, section 3.4 presents the conclusions from these experiments.

3.1 Chirality and the relation between chiral shapes and crystal structures

Chirality is the term used when two objects are mirror images of each other but are not superimposable. The two non-identical mirror versions of the chiral object are called *enantiomers* and they are assigned as *left* or *right-handed* according to their symmetry orientations. A mixture is said to be *racemic* when it has equal amounts of enantiomers[77]. However, in most chiral systems one of the enantiomers is predominant over its counterpart[78]. Indeed, most systems found in nature are *homochiral*, i.e. have their components composed by

the same enantiomer – and it is believed that they are originated from a small excess of one of the enantiomers and over time the difference in the proportions was amplified[78,79].

Shapes with chiral symmetry are present in different scales in the universe, from galaxies, to DNA molecules and nanoparticles[80,81]. In biological reactions, for example, organisms have a natural preference for the absorption of chiral amino acid molecules[82]. Understanding the chirality of nanoparticles is critical when considering drugs and chemical reactions, as is exemplified by the accident involving the tranquilizer Thalidomide ($C_{13}H_{10}N_2O_4$) in the 1960's, where the lack of understanding about the chiral properties of this molecule led to worldwide birth defects in up to 12,000 children and an unknown number of miscarriages, where the children's mothers had taken this drug. These effects were brought about by one of the two enantiomers. Thus, with better knowledge about the chiral properties of Thalidomide, and appropriate controls and restrictions, the suitable enantiomer could have been used successfully and safely in the treatment of cancer and cutaneous conditions (i.e. leprosy) [83].

An important property of chiral systems is that they exhibit optical activity when interacting with polarized light, absorbing left or right circularly polarized light to different degrees, according to its chiral orientation[84]. Therefore methods such as circular dichroism (CD) are widely used to determine the proportion of enantiomer orientations in crystals[85] .

It is interesting to note that chiral crystals, such as quartz and calcite, also selectively absorb chiral molecules on their surfaces, for example, when their interfaces interact with an aqueous solution[86]. This property is of great interest for geochemists, since these reactions are present in numerous natural processes such as soil formation and biofilm depositions[82].

When investigating chirality in inorganic crystals there are two possible situations to consider: chirality in the assembling of the atoms in the unit cell (e.g. Te, Se and Quartz), and the chirality in the overall geometric shape of the crystal (e.g. Quartz). A material is said as

having *cooperative chirality* when an overall chiral morphology is built from chiral units[87] . However, it is possible to have either lattice or geometric chirality without having the other - Te and Se often form achiral nanoparticles, for example[85]. Louis Pasteur, in his famous experiments with chiral tartaric acid molecules obtained chiral shapes, but subsequent experiments with other chiral molecules only resulted in achiral shapes, demonstrating that chirality in the unit cell is not enough to form overall chiral shapes[88]. On the other hand, there are many reports of chiral shapes for non-chiral crystal structures, such as chiral Au (FCC) shapes[89,90] (of which Chapter 5 provides a further example).

There are two main directions in the study of chiral crystals. The first one focusses on the analysis of the formation of minerals for phenomenological research. The second one is dedicated to investigate chemically synthesised samples, where metallic nanoparticles are often used as model systems[82], as is the case in this work.

Regarding the synthesis of chiral nanoparticles, there are two possible explanations for the formation of chiral shapes. In the first case the differential growth of crystal facets, induced by ligands[84,87,91], creates chiral facets. The most common chiral biomolecules used to passivate metallic nanoparticles are penicillamine, cysteine and glutathione. They act as reducing agents and shape control of the resulting nanoparticles can be achieved by the control of the reagents, temperature and the total reaction time[85,92].

The second hypothesis is based on the evolution of screw dislocations which determine the final shape of the nanoparticles. Screw dislocations are often assumed to be the cause of twisting in nanorods[93], but to our knowledge, have not been discussed in the literature for the formation of chiral polyhedral shapes prior to this work.

In this work, the system of interest consists of tellurium nanoparticles which were prepared under different conditions in order to investigate chirality in different polyhedral shapes. The unit cell of Te has a trigonal structure where the atoms are arranged in spiral chains

and packed in a hexagonal array[94], as shown in Figure 3-1. Tellurium crystallizes in the chiral space group of $P3_121$, which is formed by right-handed spirals or its enantiomorph $P3_221$ (left-handed orientation), as shown in Figure 3-1-b and c, respectively. The lattice constants for the unit cell of Tellurium are $a = 4.458$ Å and $c = 5.925$ Å.[95] Bulk tellurium is one of the rarest elements on earth and has applications in solar cells[96], thermoelectric[97] and optoelectronic devices[98].

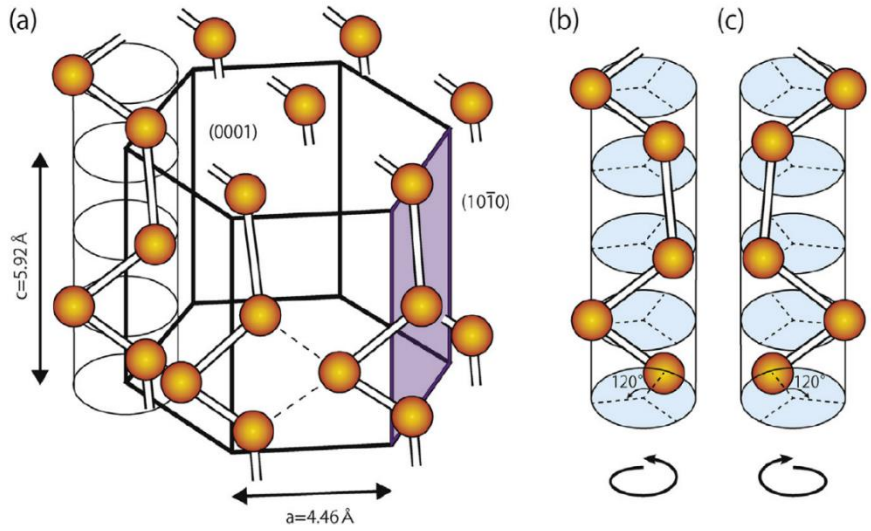

Figure 3-1 Schematics of the Te unit cell (a) and the chiral right (b) and left-handed (c) structures. Reprinted with permission from Okuyama et al.[99]. Copyright 2017 Elsevier.

Therefore, the experiments in this work explore chirality in the two different contexts introduced above, i.e., in the overall shape of these nanoparticles and the Te lattice, as the atomic assembly of Te can be arranged in one the two enantiomorphic space groups P_{3121} or P_{3221}. These experiments demonstrate that chiral morphologies form not as a result of the chiral crystal structure, or due to the presence of chiral ligands, but rather from growth mediated by screw dislocations.

The growth mechanism proposed here has the potential to form a basis for a more fundamental understanding of the driving forces involved in the synthesis of chiral crystals.

This can help not only to understand the relationship between macroscopic and microscopic chirality but could also enhance our ability for controlled synthesis of chiral nanoparticles from a variety of materials.

3.2 Electron tomography experiments

3.2.1 Sample preparation and electron tomography setup

The Te nanocrystals imaged in electron tomography were synthesized by our collaborator Assaf Ben-Moshe from the Alivisatos Group, at the Materials and Sciences Division - University of Berkeley. The reaction with the chiral ligands consisted of the reduction of tellurium dioxide in the presence of chiral thiolated penicillamine ligands with hydrazine (N_2H_4) used as a reducing agent. The handedness of the chiral nanoparticle is determined by using one of L- or D- penicillamine ligands in the reaction (left and right, respectively). D-penicillamine was the ligand used for the nanoparticles presented in this chapter, where the right-handed enantiomers are formed in a large excess (85%), but yet the mirror-image was also formed in a non-negligible amount.

Sodium dodecyl sulfate (SDS) was used to tune the nanoparticle thickness and shapes (Figure 3-2), since this component blocks lateral growth and results in different morphologies when added at different stages in the reaction. Twisted nanorods (Figure 3-2 A) with average length between 600 and 700 nm were obtained when SDS was added after 30 minutes, and growth was allowed to proceed for 2 hours. Even longer twisted nanorods (~1 μm) were obtained after 6 hours of reaction (Figure 3-2 B). The diameters of these twisted nanorods were increased when SDS was introduced after 45 minutes and nanocrystals growth proceeded for two hours (Figure 3-2 C). The twisted bipyramids were only obtained when SDS was added

after 75 minutes (Figure 3-2 D) and the largest nanoparticle sizes were obtained after 2.5 hours of reaction (Figure 3-2 E-F).

The bipyramids (Figure 3-2 E-F) were the morphology chosen in this work, since they have an interesting geometry that could not be completely understood under the 2D imaging from regular STEM imaging and required electron tomography to understand their geometry more fully. Also, these nanoparticles were found to be more stable under the focused electron beam, as expected since they are thicker than the nanorods.

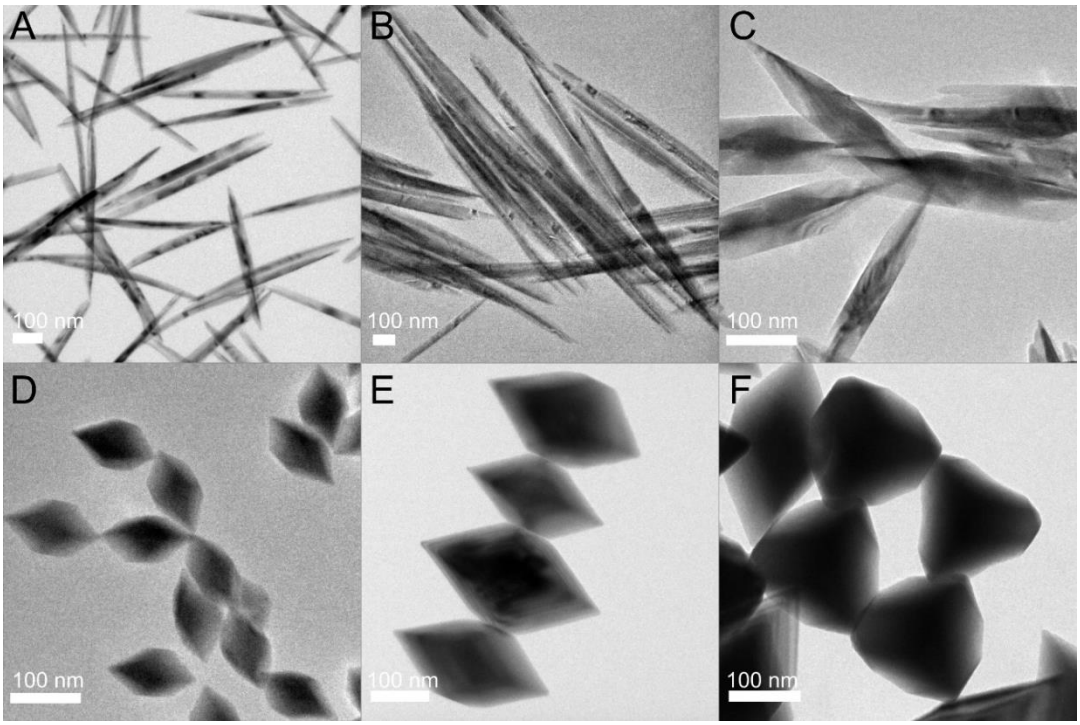

Figure 3-2 TEM images of different morphologies of Te nanoparticles obtained with SDS added at different stages of the reaction. a) Twisted nanorods (600-700 nm) obtained from the regular reaction when SDS was added after 30 minutes and growth was allowed for 2 hours. b) After 6 hours of reaction, longer twisted nanorods (1 micron) were obtained. (c) When SDS was added after 45 minutes and growth was allowed for 2 hours, thicker twisted shapes were obtained. (d) Small twisted bipyramids were formed When SDS was added after 75 minutes and the growth was immediately stopped. (e) Large twisted bipyramids obtained after 2.5 hours of reaction. (F) A view along the [0001] direction of several large twisted bipyramids. All of the nanocrystals depicted were obtained with the ligand D-penicillamine. Figure and syntheses of the nanoparticles were performed by Assaf Ben-Moshe.

The solutions with these nanoparticles were drop cast onto amorphous carbon film TEM grids (200 mesh), where they were allowed to dry under ambient conditions. After drying, a solution of Au nanoparticles (10 nm) used as fiducial markers was also drop cast.

All tomography datasets were acquired using a FEI Titan operated at 200 kV, with semi-convergence angle of α_c = 10 mrad and using an ADF detector with an inner collection angle of β_c = 84 mrad. The HAADF-STEM images were typically acquired with 1024 × 1024 field of view and dwell time of 15μs. The series was acquired using the Thermo Scientific Tomography software. Once the microscope was properly aligned, the software provided controls of parameters to minimize shifts in the x and y directions and changes in focus on the sample.

The tilt series was aligned using the IMOD tomography package (version 4.9.10). IMOD is a package for the 3D reconstruction and image processing of electron tomography series. The package contains tools for aligning the stack of images through an interface[61,100]. The main steps performed to reconstruct the tomography datasets are briefly described in the following paragraphs.

The first step is a coarse alignment using cross-correlation to find an initial translational alignment between successive images of the tilt data series. The IMOD interface provides the option to the user to perform only this alignment, in the case where the sample does not have fiducial markers, or where alignment by fiducial markers does not provide good results. The output coarse aligned series can be aligned further using a different platform or scripts, as was the case for some datasets in Chapter 4.

The next step consists of the creation of a 3D model based on the position of the gold fiducial markers, as is shown for one projection in Figure 3-3 to determine their center of masses. There are different options to generate a fiducial model, the one chosen here - that worked best in all the series - was the one where the starting points (seeds) are picked manually

in one projection and the program tracks the gold fiducial markers automatically over the tilt series.

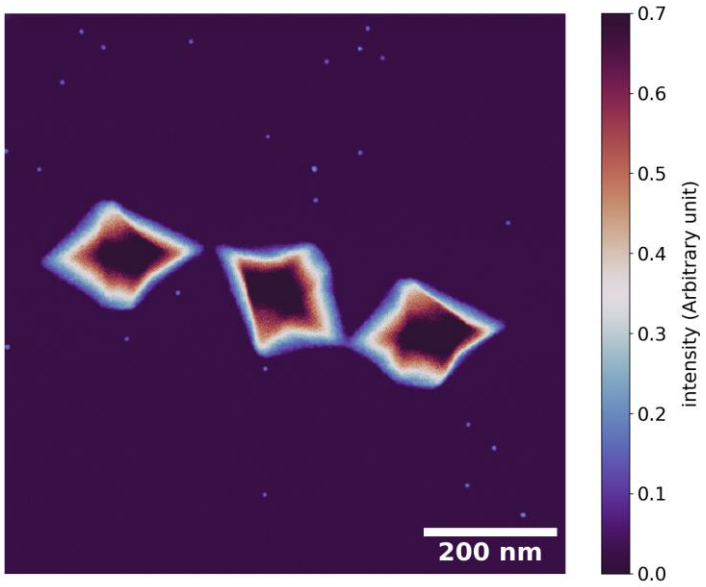

Figure 3-3 STEM tomography projection at 0˚ showing the Te bipyramids and the Au markers (the small light blue "dots") used for the fine alignment of the tilt series.

In many cases, there were missing data in the automatically traced trajectories of the fiducial markers over the tilt series. These missing points need to be edited manually as in order to achieve a satisfactory alignment it is important to ensure that most of the markers are tracked across the entire range of the tilt series. It is also important to manually fix incorrect positions in the center of markers assigned by the automatic tracking. After the fiducial alignment is generated, the fine alignment is performed to correct misalignments caused by rotations, tilts and variations in magnification in the series. The program displays the residual error which needs to be minimized to obtain a good final alignment. Finally, the data is down-sampled to reduce the computational time and memory used in data processing for the reconstruction using the back-projection or SIRT method**.**

All the volume rendering and visualization was performed using Tomviz 1.5.0+, an open source application for the rendering and visualization of 3D tomographic data.

3.2.2 Electron tomography of Tellurium bipyramids with chiral ligands

The first experiment consisted of preparing Te nanoparticle samples with the chiral ligand, penicillamine, to check whether these nanoparticles also had a chiral shape. Reconstructions of two of the tomography datasets are shown here, where in the first series, 1024 ×1024 images were acquired in the angular range of -65˚ to 70˚, with a step size of 1˚ , a pixel size of 1.15 nm and with an electron beam dose of 1.6×10^3 $e^- nm^{-2}$ $frame^{-1}$. In the second series, 1024 ×1024 images were acquired from -69˚ to 70˚, with a step of 1˚, a pixel size of 0.82 nm and with an electron beam dose of 3.1×10^3 $e^- nm^{-2}$ $frame^{-1}$. The resulting reconstructed volumes from the tomography series are shown in Figure 3-4 and Figure 3-5, respectively. It can be observed in the reconstructed volumes of these nanoparticles that, they have a chiral shape, where the facets are asymmetric along the *c*-axis.

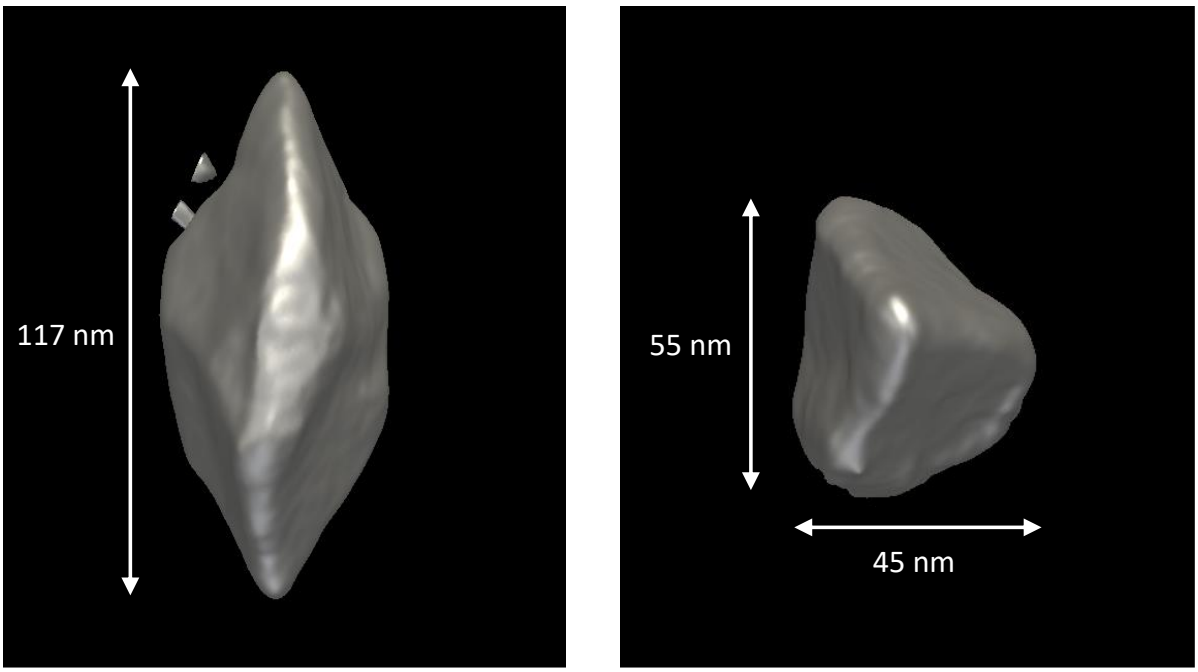

Figure 3-4 A surface rendering of a STEM tomogram from a bipyramid with chiral ligands along the $[2\bar{1}\bar{1}0]$ direction (left) and along the [0001] direction (right).

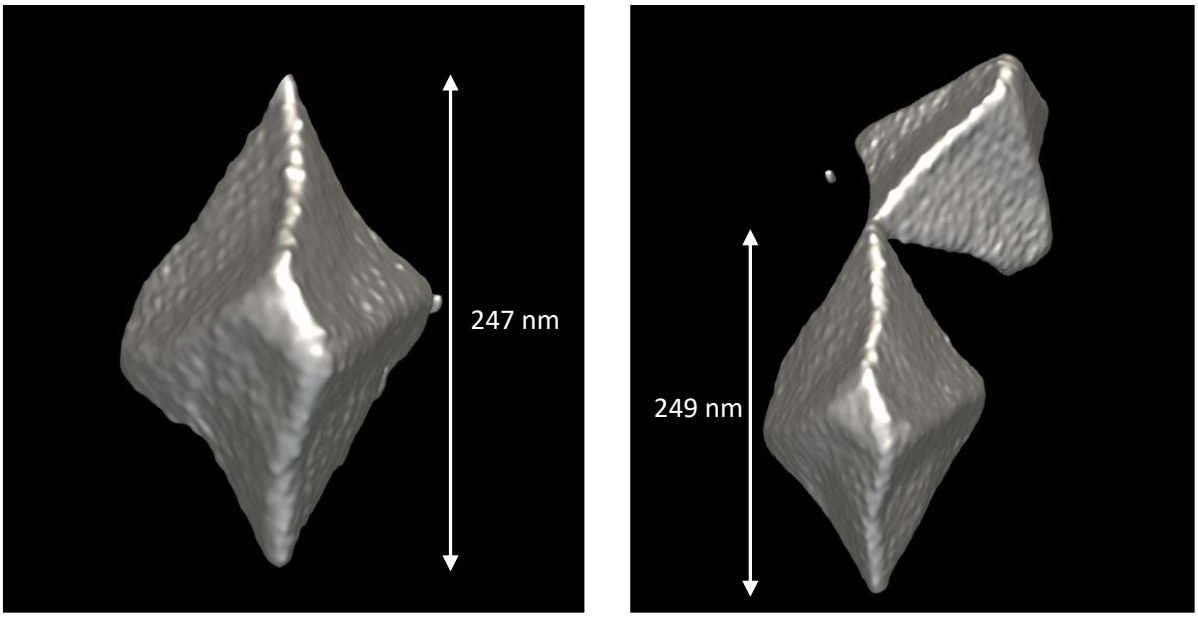

Figure 3-5 Another surface rendering of a STEM tomogram from bipyramid nanoparticles with chiral ligands and trigonal symmetry.

It is interesting to note that depending on the type of ligand (pure D or pure L) used in the synthesis, one of the mirror images was produced in excess. This was verified through the statistics of a large nanoparticle population (approximately 300 nanoparticles per sample) from SEM images, performed by a collaborator, A. Mueller. Both cases, i.e. samples produced with pure D or pure L ligands, resulted in a roughly 85% fraction of nanoparticles with the same orientation as the ligand used in the synthesis – the other 15% had the mirror-image orientation. It was also observed that the nanoparticles of the less abundant orientation, were on average smaller, indicating that the chiral ligands interfered not only in the nucleation process, but also in the growth rates of these nanoparticles.

When comparing the tomography reconstruction with SEM images (Figure 3-6), it is apparent the edges of the reconstructed Te nanoparticles are not as sharp as viewed in the SEM images. The smoothed edges of the reconstructed nanoparticles are due to the limited resolution of the data as well as post-processing with a gaussian filter (σ=2) to reduce noise.

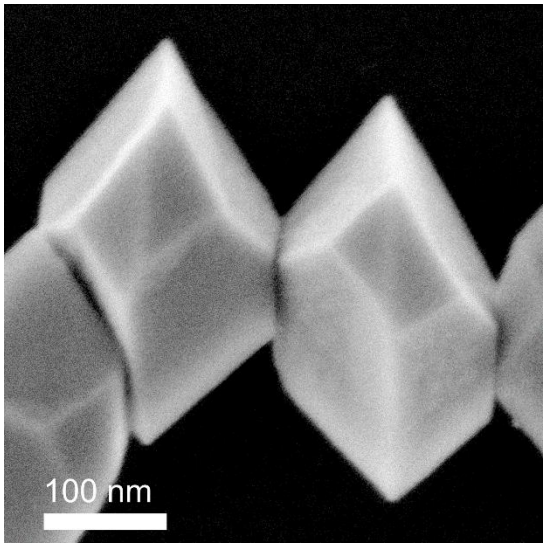

Figure 3-6 SEM image of two Te bipyramidal nanoparticle enantiomers. Image performed by A. Mueller.

Figure 3-7 shows the cross sections cut along the *c*-axis of one these nanoparticles, evidencing the trigonal symmetry of the bipyramids and the twisting of their vertices around a fixed trigonal axis, indicated by the white dashed lines superimposed onto the cross sections.

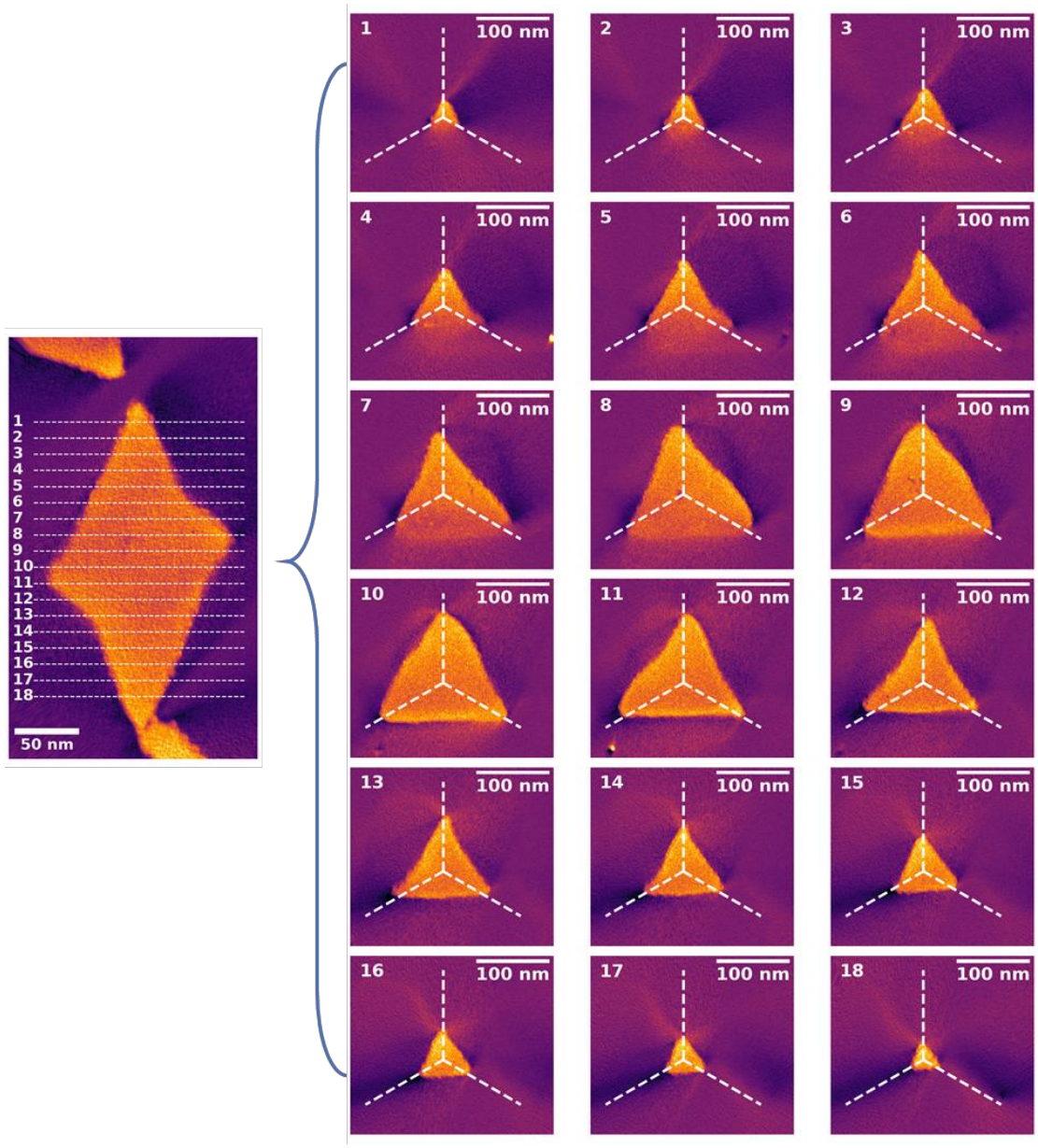

Figure 3-7 Cross section slices from the reconstructed volume of one of the Te nanoparticles. Left: view along the $[2\bar{1}\bar{1}0]$ direction showing the cuts along the c-axis. Right: view along the [0001] direction showing the respective cross sections with a twisted-trigonal symmetry and variations in the locations of vertices along the growth axis. The white dashed lines are constant along the slices and here is used as reference to highlight the twisting of the vertices.

Interestingly, another feature observed in the reconstructed Te bipyramid volumes, was the presence of voids, as shown in the wireframe rendered view in Figure 3-8. Figure 3-9 also shows STEM images showing these voids in both nanorods and bipyramid morphologies. As can be observed in these figures, the voids had an almost spherical shape and were located in

regions near the center of each nanoparticle. These features were detected in most of the imaged nanoparticles formed though this synthesis method. Beyond the fact that these voids were observed in the majority of hundreds of nanoparticles during the setting of the tomography experiment, the presence of voids was also confirmed by checking the acquired STEM images, where 92% of 25 nanoparticles exhibited central voids. This indicates that the formation of these voids might be related with the growth mechanism of these nanoparticles.

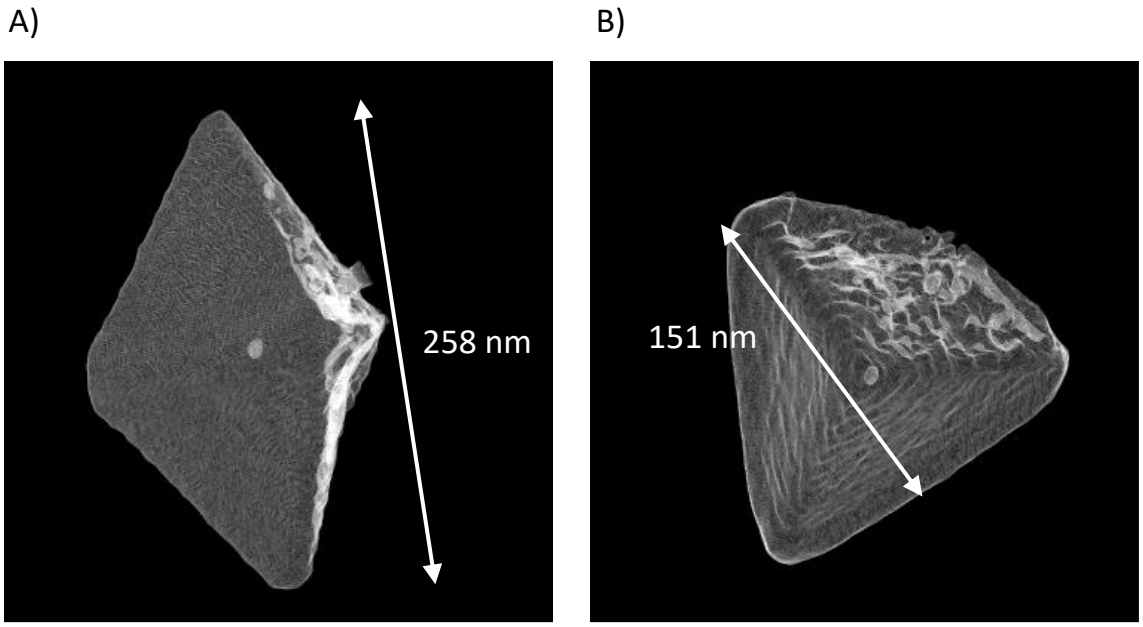

Figure 3-8 Wireframe rendered volume from the electron tomography of a Te nanoparticle showing a spherical void inside the bipyramid.

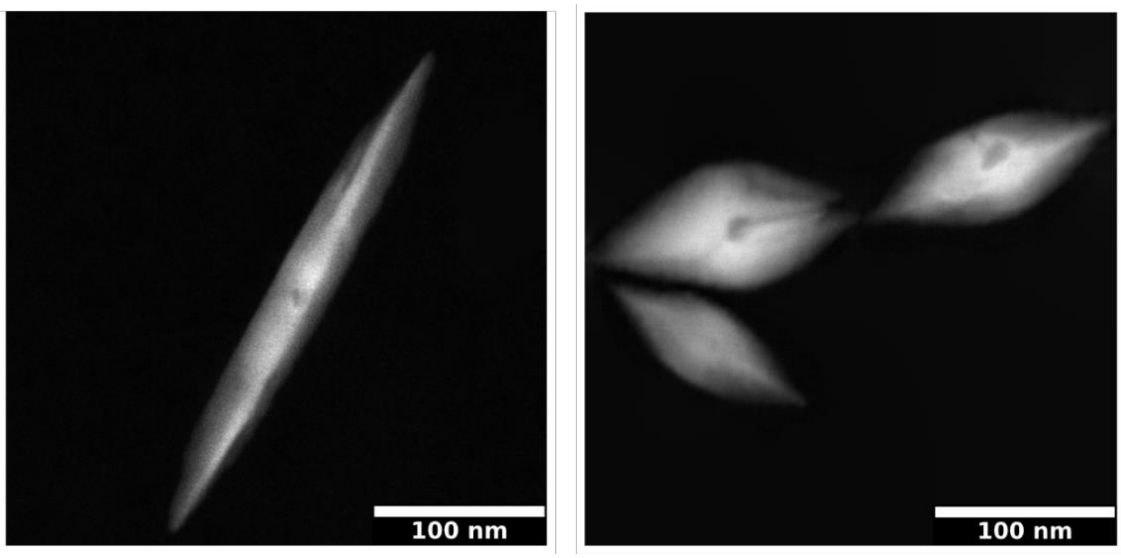

Figure 3-9 ADF-STEM images showing voids on thin Te nanorods and bipyramids.

In order to estimate the dimensions of these voids, line profiles from two nanoparticles (labeled as NP1 and NP2) were extracted along each orthogonal direction (x, y, z), as indicated in Figure 3-10. The line profiles show regions of low intensity where there is a void and their locations were calculated using the function *signal.argrelmin* from the scipy python package[101]. This function compares each point in the data with a number of neighbours, defined by the user and gives the peak position. For the line profiles in Figure 3-10, the chosen number of neighbours was N = 100.

Once the locations of the voids were determined, their size was calculated using the *signal.peak_widths* python function. This function calculates the width of a peak at a relative distance to the peak's prominence. For both nanoparticles, the relative height at which the peak width was measured was half of the prominence. The calculated void diameter in each orthogonal Cartesian direction was 10 ± 1 nm, thus the voids are approximately spherical within errors. The errors were estimated as the difference between the maximum and minimum width obtained for reasonable fits of peak.

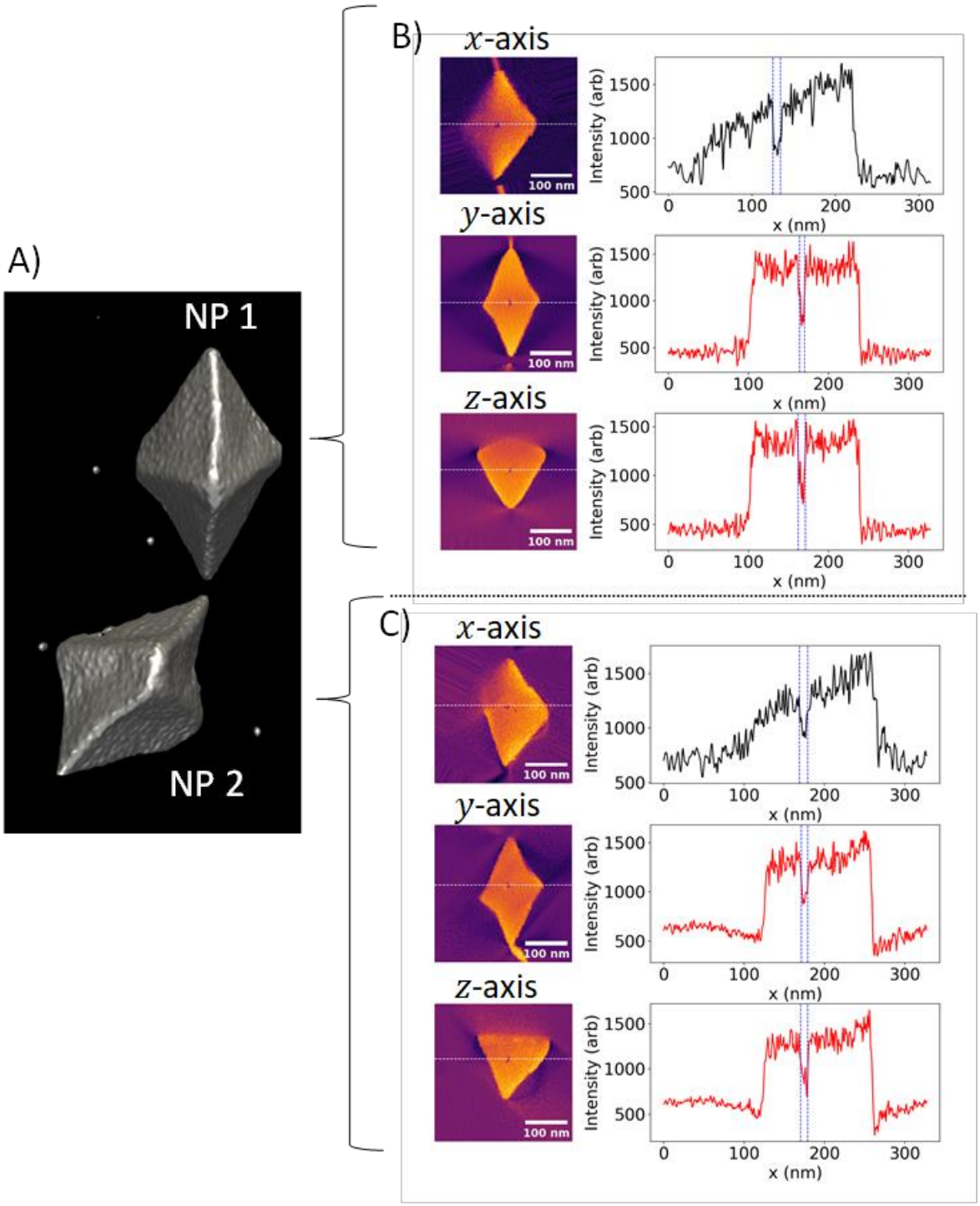

Figure 3-10 Line profiles through the voids observed in the STEM tomography reconstructions for two Te nanoparticles. a) rendered volume of nanoparticles labelled as NP1 and NP2. b) NP1: Volume cuts normal to the three Cartesian coordinates (x, y, z), where z is along the c-axis of the nanoparticle; and corresponding line cuts through the voids, indicated by dashed white lines. c) NP2: same figures as before. Void diameters are found to be 10 ± 1nm along all directions, thus the voids are spherical within errors.

3.2.3 Electron tomography of chiral Te bipyramids with achiral ligands

In order to investigate whether chiral ligands are necessary for the formation of chiral shapes, a second synthesis of Te nanoparticles was performed under similar conditions, however penicillamine was replaced with mercaptopropionic acid, which is an achiral ligand.

The tomography series was acquired over the range of -75˚ to 70˚, with 2˚ step size and a pixel size of 0.91 nm and with an electron beam dose of 2.5×10^3 $e^- nm^{-2}$ $frame^{-1}$. Interestingly, the nanoparticles also formed a chiral shape (Figure 3-11). However, as shown in Figure 3-12, although the cross-sections along the *c*-axis exhibit a trigonal symmetry in the regions near the apex of the nanoparticle, they progressively converged into a hexagonal geometry in the middle sections. Another difference between these nanoparticles and the ones prepared with chiral ligands, is that the synthesis with an achiral ligand resulted in a racemic nanoparticle solution, i.e. the left and right-handed orientations were present in the same proportion, as was confirmed by CD experiments performed by A. Moshe.

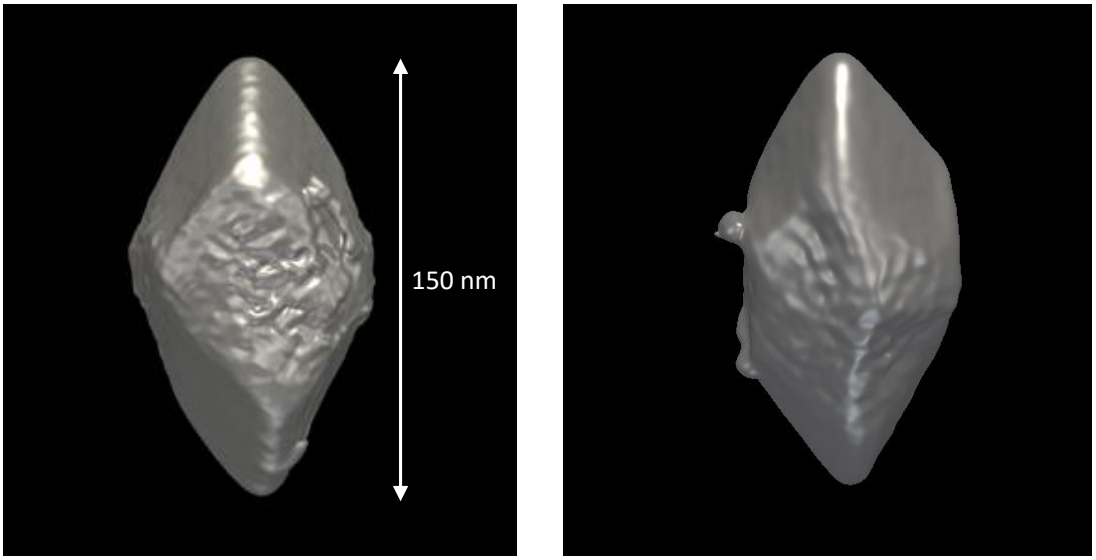

Figure 3-11 Frontal and back views of a reconstructed Te chiral nanoparticle. The bipyramidal shape resulted from a synthesis performed with an achiral ligand (mercaptopropionic acid).

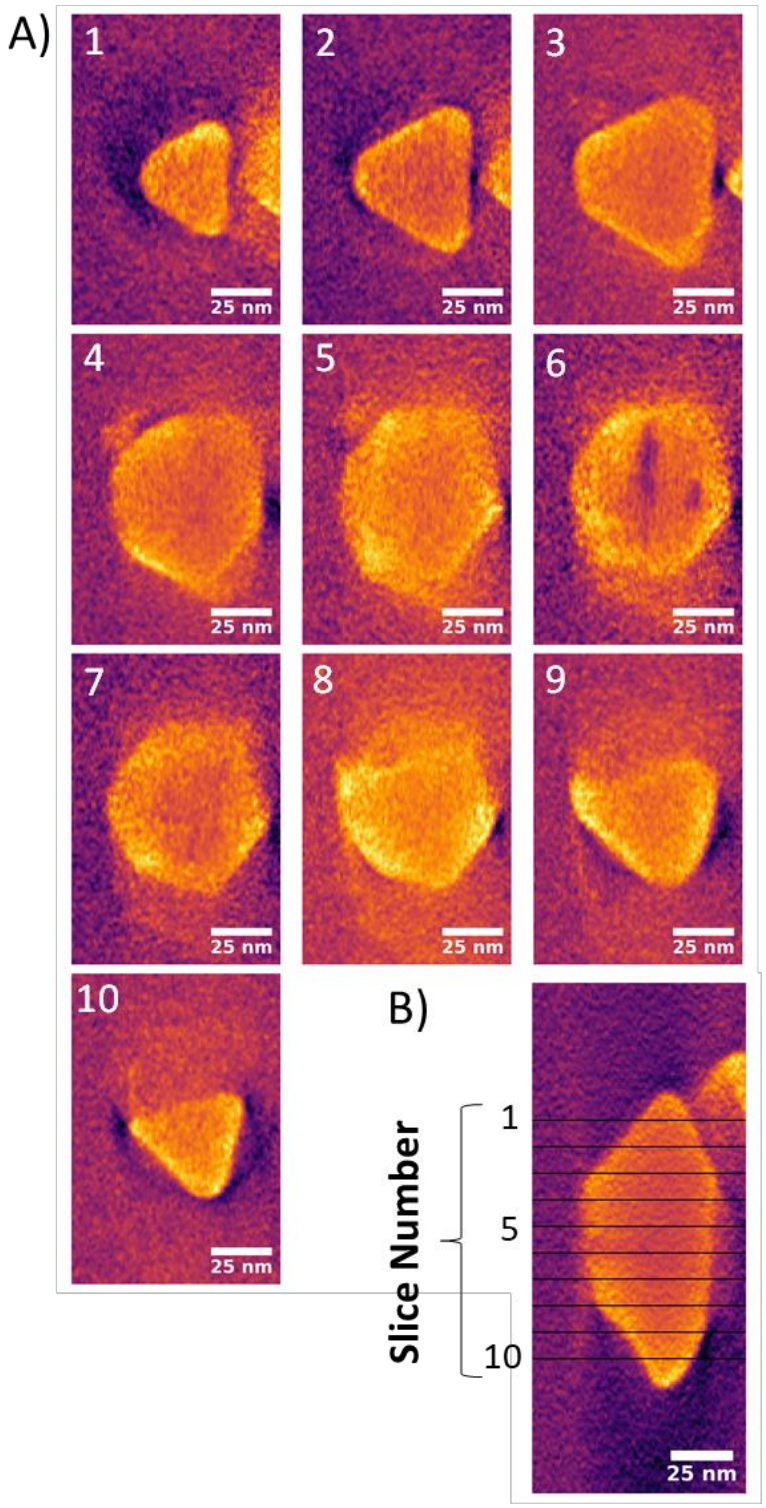

Figure 3-12 Cross sections from the same nanoparticle show in Figure 3-11 a) The slices along the *c*-axis show a three-fold symmetry (1-3), which progressively converges to a six-fold symmetry (4-8) and ends up again with a three-fold symmetry. In this chiral nanoparticle, some voids can also be noted (6). b) shows where these cuts are made in this Te nanoparticle side view.

This result implies that the chiral ligands are enantiomer modifiers and tune the proportions of the mirror-imaged nanoparticles, instead of being the cause of the chiral shape by itself. This result is important since it proves that the growth of a chiral crystal cannot be fully explained by the presence of chiral ligands, as has been suggested in previous models[87,102].

Voids were also observed in reconstructed volumes of these nanoparticles - and were also detected in 64% of 39 nanoparticles present in STEM images. However, they were present in a different form from the ones observed in the Te nanoparticles prepared with chiral ligands. As it shown in Figure 3-13, there are multiple voids per nanoparticle and they have non-spherical elongated shapes, which is different from the single spherical void localized in the core of the bipyramid, as presented in the previous section. The presence of voids in both syntheses, i.e. with and without chiral ligands, may be related to the growth mechanism of the formation of the chiral polyhedral shapes.

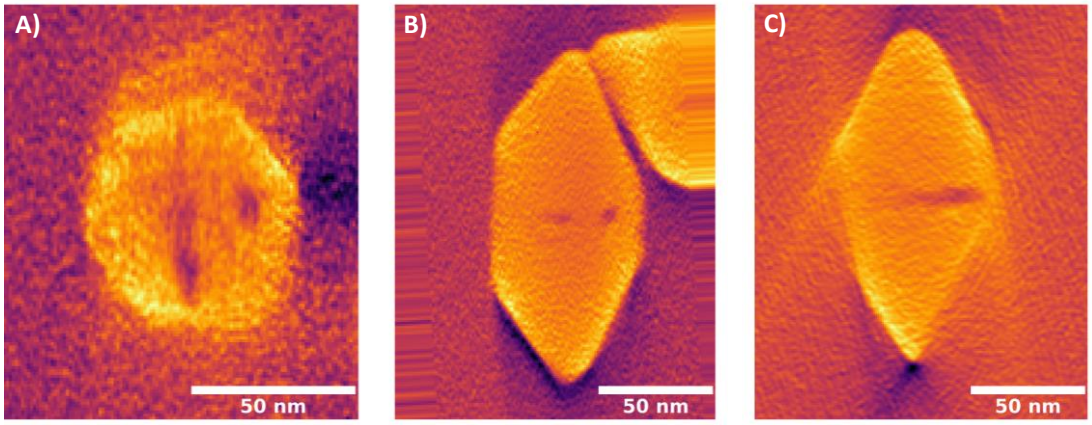

Figure 3-13 Slices from the same nanoparticle show in Figure 3-11 showing multiple and elongated voids. a) is a cross section normal to the c-axis and b) and c) are the other two perpendicular cuts through the same nanoparticle.

Therefore, the results from this experiment require an alternative explanation to that commonly put forward in the literature to describe the formation of chiral polyhedral shapes. Our interpretation is that the chiral polyhedral shapes are formed by a growth mechanism that

develops from screw dislocations. Screw dislocations are widely used to explain twisting structures, such as nanorods[103], nanoplates[104] and the slope of pyramids[105–108]. Our hypothesis is that a screw dislocation is formed in the early growth stages, with a Burgers vector given by:

$$\vec{b} = c[0001] \tag{3.1}$$

And it is dissociated in partial screw dislocations:

$$\vec{b} = \frac{c}{3}[0001] \tag{3.2}$$

This hypothesis was supported by a model that simulates a Te crystal with a dissociated screw dislocation and confirmed through atomic resolution STEM imaging, both performed by other members involved in the project and shown in appendix A. STEM imaging confirmed the discontinuity in atomic rows of the crystal that would result from the presence of a dissociated screw dislocation.

The formation of voids in the core of the nanoparticles is also associated with a growth mediated by screw dislocations in the literature[109–112]. A screw dislocation generates a strain in their surroundings material. Voids may be formed when this strain energy is larger than the surface energy required to generate an internal surface.[103,113,114]

The current theoretical explanation for the formation of screw dislocations also predicts that they are preferentially formed under low saturation rates, i.e. under slow reduction rates of Te[115]. Therefore, it was important to check the outcome from a synthesis with high monomer saturation. If the higher monomer saturation will suppress the formation of screw dislocations, and the presence of screw dislocations is the main reason for the observed chiral shapes, then it may be expected that non-chiral shapes form under these growth conditions. The results of high monomer saturation synthesis are presented in the next section.

3.2.4 Electron tomography of Te bipyramids with chiral ligands and higher monomer concentration

As mentioned earlier, the next experiment was performed to test whether the formation of screw dislocations is necessary for the formation of chiral shapes. It has been predicted that screw dislocations only form under slow growth conditions. Therefore, Te nanoparticles were prepared with a higher tellurium dioxide reduction rate and this was achieved by using a larger volume of hydrazine (6 mL) to the prepared solution (5.5 ml), contrasting with 2 mL which was added to produce the chiral bipyramids presented previously.

The tomography dataset taken from these nanoparticles was acquired over the tilt range of -75˚ to 75˚, with a step size of 2˚ and a pixel size of 1.82 nm. The electron beam dose was 6.3×10^2 $e^- nm^{-2}$ $frame^{-1}$.

The rendered reconstructions of these nanoparticles (Figure 3-14) indeed show achiral shapes. It is important to highlight that these achiral morphologies were formed even when using chiral ligands, and with the same concentration as the reactions that form chiral shapes.

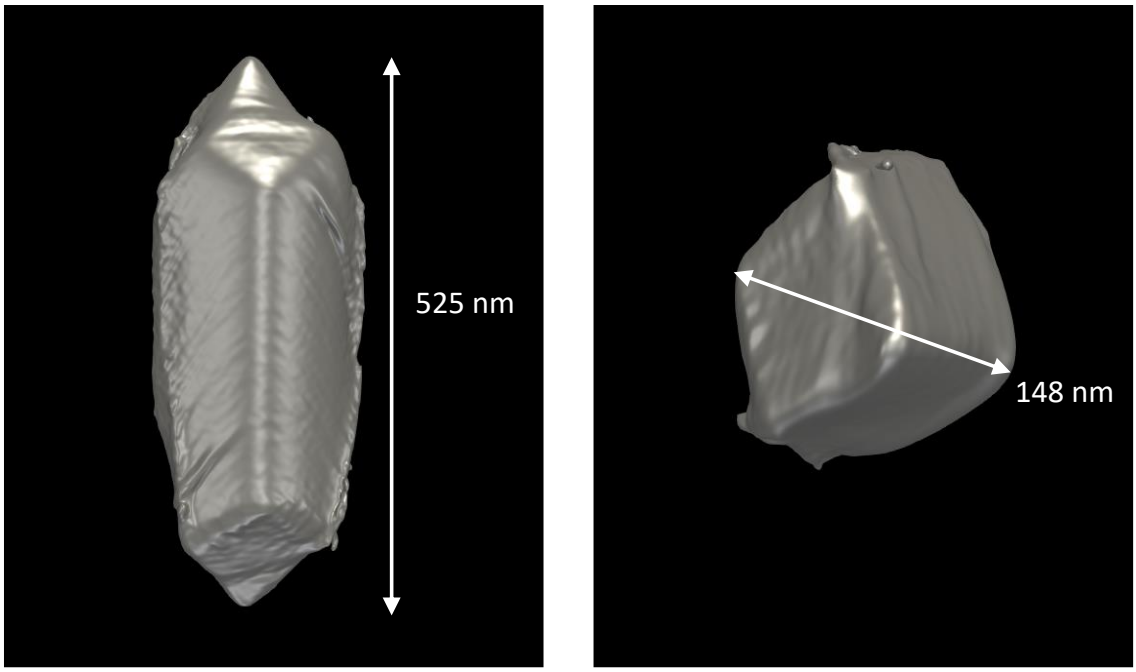

Figure 3-14 Rendered STEM tomogram of achiral Te particle grown with higher monomer concentration chiral penicillamine ligands and top view of nanoparticle with chiral ligand but synthesized with higher monomer concentration.

These achiral nanoparticles also revealed a trigonal symmetry towards their apexes which evolved into hexagonal symmetries towards the nanoparticle center. The cross-sections of a representative nanoparticle are shown in Figure 3-15. No internal voids are detectable in the reconstructed volume, which is in agreement with the hypothesis that voids form due to the presence of screw dislocations and screw dislocations are not present in this case due to the rapid growth conditions, as evidenced by the lack of chiral geometry.

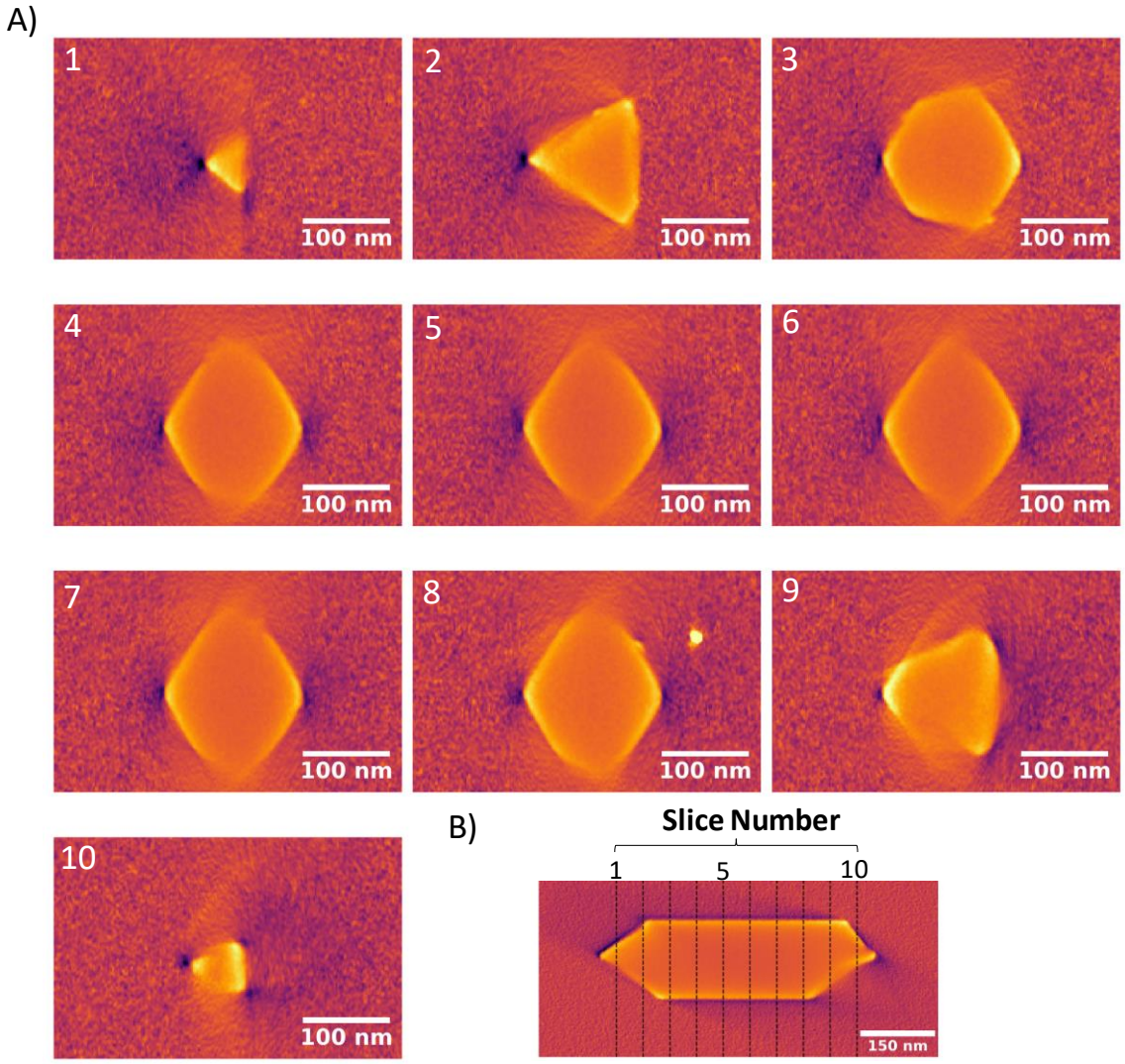

Figure 3-15 Cross sections from a reconstructed achiral Te nanorod synthesized with chiral ligands but higher Te dioxide rates. a) The first slices along the *c*-axis show a three-fold symmetry (1-2), that progressively evolves to a six-fold symmetry (3-8) and ends up again with a three-fold symmetry (9-10). b) shows where these cuts are made in this Te nanoparticle side view.

3.3 4D-STEM experiments

In the previous sections the experiments performed to investigate the origin of chiral shapes led to the interpretation that screw dislocations are responsible for the formation of chiral polyhedral nanoparticles. The evidences for screw dislocations will depend of the growth conditions[116] and are not always easily detectable, since screw dislocations are often unstable

and mobile[104]. Previous work has shown that screw dislocations in semiconducting materials, such as Tellurium, may have their mobility increased under the effect of an electron beam[117]. Lavagne et al. found that mobility of screw defects in ZnS nanowires increased with beam dosage. The beam dosages used in these experiments were ~100 times higher than used in the following study for Te nanocrystals[118].

In the particular case of the analysed nanoparticles studied in this work, the typical contrast lines from screw dislocations could not be identified through classical TEM diffraction contrast experiments. Another indication for growth mediated by screw dislocations is the Eshelby twisting of the lattice. The Eshelby twist τ in a 1D nanowire generates a twist per unit length and is given by[104]:

$$\tau = \frac{|\vec{b}|}{\pi r^2} \tag{3.3}$$

where $\vec{b}$ is the Burgers vector of the screw dislocation and r is the radius of the nanowire. Since τ is inversely proportional to r^2, it is difficult to measure a twist for thick nanoparticles. Therefore, in order to be able to detect the Eshelby twist and give more support to the interpretation of growth mediated by screw dislocations, 4D-STEM experiments were performed on Te nanorods. As presented in section 3.2.1 (Figure 3-2 (a-c) and Figure 3-9) these nanorods were prepared with the same conditions as the bipyramids, but with the reaction interrupted at earlier stages.

Therefore, if screw dislocations are present from early stages of growth, they are expected to be present in the nanorods. The aim of the 4D-STEM experiments was to quantify the twist in the lattice of the Te nanorods.

3.3.1 4D-STEM experimental setup

In the 4D-STEM experiments, the data was acquired with a near-parallel probe, using a convergence angle that was set to 0.48 mrad. In this configuration the diffraction disks did not overlap and, a convergent nanobeam electron diffraction (NBED) pattern was formed. Although during the experiment there was no tilt in the electron beam or in the sample direction, scanning the electron probe over the nanoparticle resulted in mistilts of the zone axes that were evidenced as circular patterns, the ZOLZ disk, as shown in Figure 3-16.

All the experiments were performed using a FEI Titan TEM, operated with a FEG at 300 kV, with C2 aperture size of 40 μm and spot size 11. At this voltage, the electron beam has a wavelength of 1.9 pm, as calculated from Equation (1.3). The diffraction patterns images (512 × 512 pixel) were acquired with a Gatan Orius CCD camera. The data was acquired with a python script, written by Christoph Gammer[1], that moved the beam.

[1] Code may be obtained from Christoph Gammer: Christoph.Gammer@oeaw.ac.at

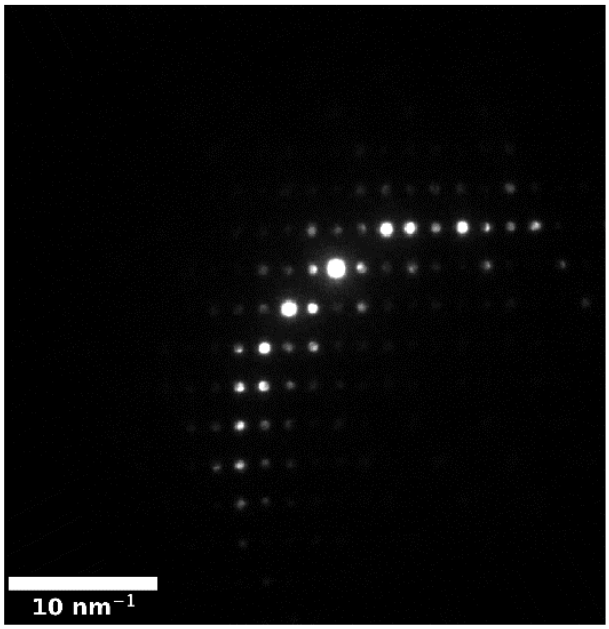

Figure 3-16 NBED pattern taken with a convergence angle α_c = 0.48 mrad and camera length L = 130 mm.

3.3.2 ZOLZ circle fitting of electron diffraction patterns

Since the NBED patterns, taken with α_c = 0.48 mrad, had non overlapping disks, the misorientation of the crystals could be quantified by measuring the distance of the center of the ZOLZ circles to the direct electron beam (central disk in the images)[119], indicated in Figure 3-17 as C_L and C_B, respectively.

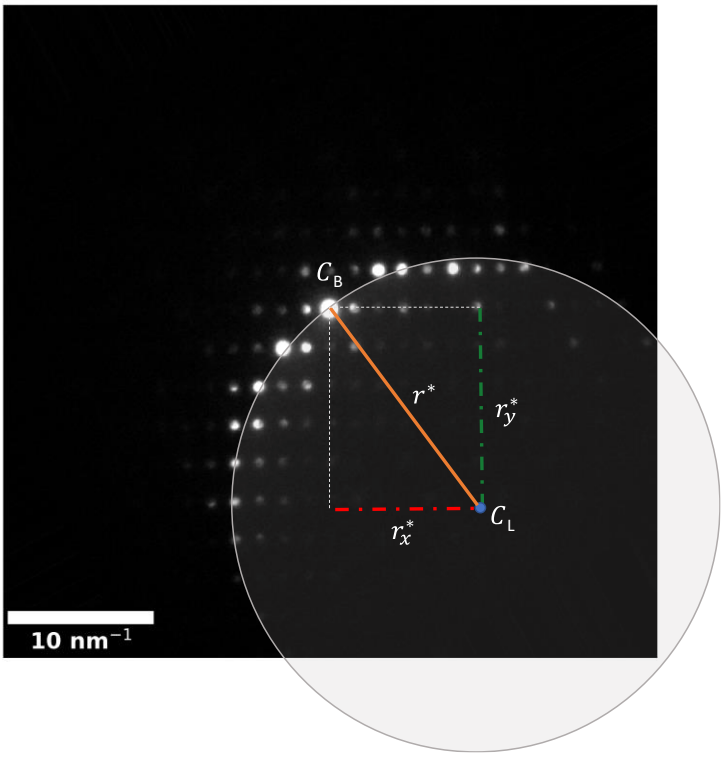

Figure 3-17 Schematic showing a diffraction pattern and the distance r^* between the central beam and the center of the ZOLZ circle. r_x^* and r_y^* are the horizontal and vertical components of the distance vector, respectively.

The relation between the misorientation $\emptyset$ and the radius r^* of the ZOLZ circle is given by the equation[120]:

$$\emptyset = r^* \lambda \tag{3.4}$$

Where λ is the electron beam wavelength. Decomposing r^* into its horizontal and vertical components (as indicated in Figure 3-17) results in:

$$\emptyset_x = r_x^* \lambda \quad \text{and} \quad \emptyset_y = r_y^* \lambda \tag{3.5}$$

The [0001] growth direction of the Te nanorod was indexed in the diffraction patterns and as such $\emptyset_x$ gives the out-of-plane bending of the c-axis and $\emptyset_y$ gives the rotation around the c-axis, respectively, as illustrated in Figure 3-18. The in-plane rotation γ around the zone axis is given by the rotation of the diffraction pattern[121].

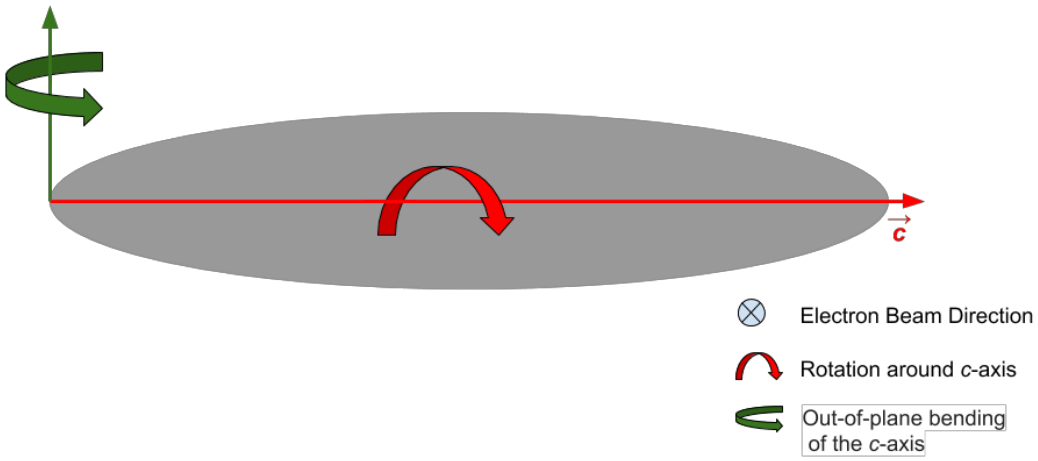

Figure 3-18 Scheme of orientations used for rotation mapping of the Te nanoparticles.

Although the diffraction data was recorded within a rectangular section containing the nanoparticle, the scripts were optimized to run only in the regions of interest, i.e. in the area inside the nanoparticle. This was implemented through a mask that was built using VDF reconstructions, as presented in section 2.8.1. As an example, VDF and VBF reconstructions from a Te nanoparticle are presented in Figure 3-19. Probe positions external to the nanoparticle did not result in any diffracted intensities as the probe was incident only on amorphous carbon, and as such these positions were not analysed.

Thus, to select the data where the code should be applied, thresholding was performed using VDF reconstructions, and a mask was applied to attribute non-zero values only inside the nanoparticle.

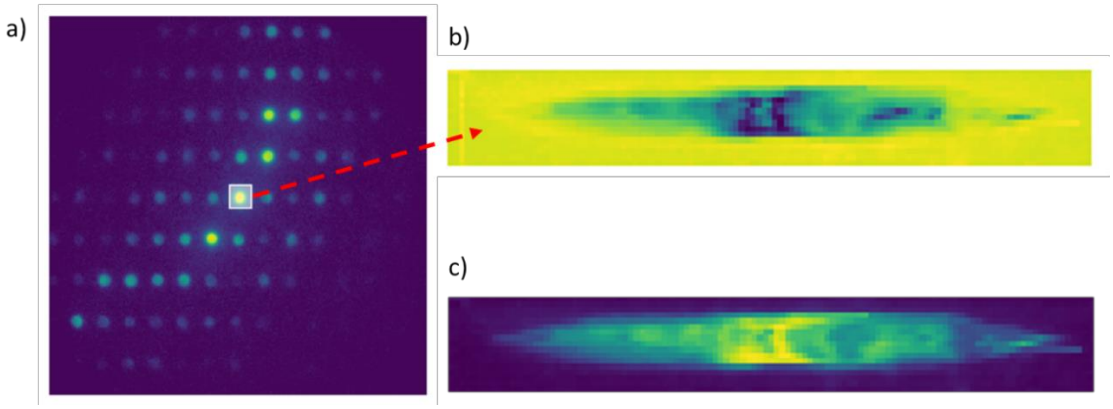

Figure 3-19 VR from the NBED pattern frames acquired from a chiral Te nanoparticle a) Diffraction pattern b) The VBF reconstruction from the direct beam disk, and within the box shown in the image for each pixel in the nanoparticle c) VDF reconstruction with all the spots excluding the direct beam disk.

Therefore, for each diffraction pattern acquired *inside* the nanoparticle, the detection of the most intense spot peaks was performed prior to the Laue circle fittings. To detect the most intense peak a combination of local maximum and edge detection filters were used. The local maximum filter was used to select the most intense peaks in the image, and the *peak_local_max* function from the skimage library was used for this purpose (Figure 3-20,b). This python function uses a local maximum filter to identify and return the coordinates of local peaks contained within an image[122].

Although the local maximum filter can efficiently select the most intense single pixels in the image, it does not determine the disk centers with sufficient accuracy. In order to solve this problem and refine the positions of the peaks, a *canny* filter was used for the edge detection and then each peak was fitted using Hough circles[123] (Figure 3-16, c). Both tasks were performed using functions from the skimage library (*feature.canny* and *transform.hough_circle_peaks*, respectively) and thus the center of the most intense circles (detected with the maximum filter) could be determined more precisely (Figure 3-16, d).

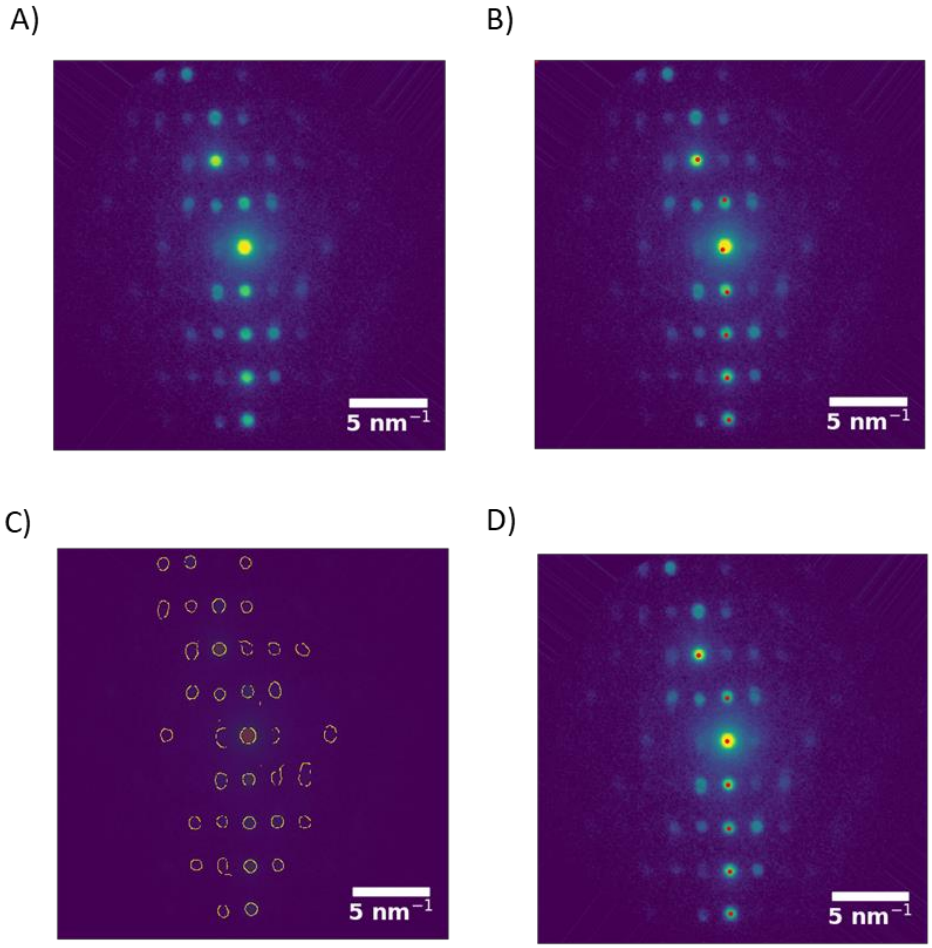

Figure 3-20 Image processing procedure to determine the positions of the peaks in the diffraction patterns acquired in the 4D-STEM experiment. (a) One of the diffraction patterns images from the dataset taken with α_c = 0.48 mad. b) The peaks are detected using a local maximum function. Although it effectively detects the brightest spots, it results in imprecise center positions. c) a Canny filter (σ = 5) is used to detect the edges of each disk d) The center of each disk is identified from the edges using the Hough circles method.

Once a set of peaks were detected the next step was the fitting of the ZOLZ circles. The fitting of a circle to a noisy dataset of points is an old and quite complex problem that is present in many fields[124–126]. The larger the angle of the arc to be fitted is, the higher is the precision of the estimated parameters, therefore yielding a lower variance of the fit parameters[127]. In the case of the ZOLZ circles, when the sample is not aligned with the beam, we obtain half circles, whereas when it is close to the zone axis positions whole circles could

be fitted. The approach implemented in this work was the minimization of the sum of the squares of the errors between the data points and the circle function, and therefore this non-linear least-squares (Levenberg-Marquardt)[126,128] problem has the objective function J:

$$J = \sum_i \varepsilon(x_i, y_i)^2 \tag{3.6}$$

Where the residuals $\varepsilon(x_i, y_i)$ are given by:

$$\varepsilon(x_i, y_i) = \sqrt{(x_i - x_c)^2 + (y_i - y_c)^2} - r \tag{3.7}$$

Where (x_c, y_c) and r are the center coordinates and the radius of the fit circle, respectively; and subject to the constraint that the circle perimeter intersects the direct beam [0000] diffraction disk.

The equation (3.6) was solved using the function *optimize.minimize* from the python library scipy and using the *Sequential Least Squares Programming method* (SLSQP). Since this method requires a reasonable first estimation for the solution, an algebraic solution for the circle parameters (r_0, x_{c0}, y_{c0}) that pass through three selected points contained in the DP was used for this purpose. The three points selected were, as illustrated in Figure 3-20: $P_1 = (x_1, y_1)$, the [0000] direct beam; $P_2 = (x_2, y_2)$, the most distant point to the direct beam and $P_3 = (x_3, y_3)$, the most distant point to P_2. The coordinates (r_0, x_{c0}, y_{c0}) of circle that circumscribes P_1, P_2 and P_3 were calculated algebraically by finding the intersection of the perpendicular bisector lines of the segments $\overline{P_1P_2}$ and $\overline{P_2P_3}$, as also shown in Figure 3-21.

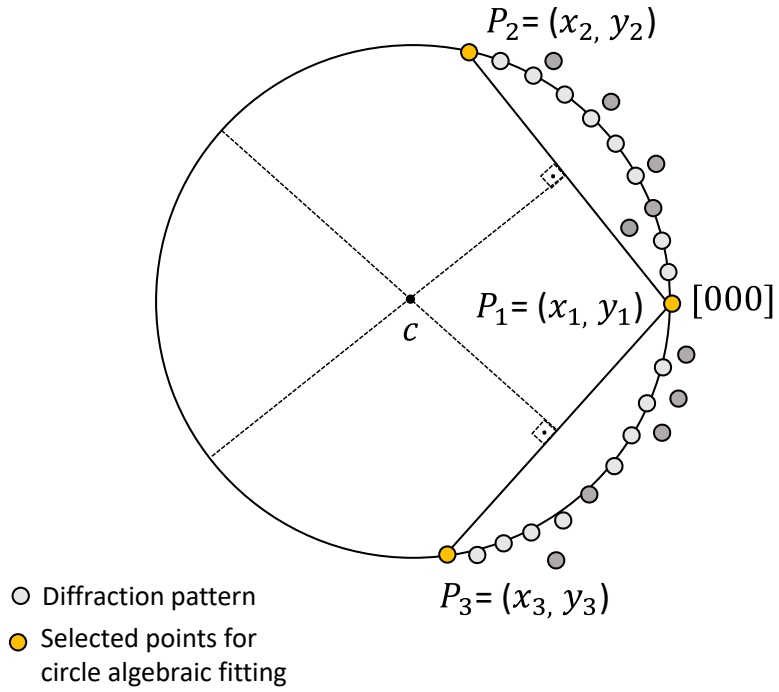

Figure 3-21 Scheme showing DP and points selected for the first estimate for the fitting of the circle through the least square method. The three points selected were: P_1, the direct beam [000]; P_2, the most distant diffraction point to P_1; and P_3, the most distant diffraction point to P_2. The coordinates of the center and radius of the circle were determined through the intersection of perpendicular bisectors of $\overline{P_1P_2}$ and $\overline{P_2P_3}$.

Once the optimal circle (r, x_c, y_c) was determined through the minimization of equation (3.7), the coordinates of the fitted circle center allowed the determination of the out-of-plane bending ($\emptyset_x$) and the rotation around the c-axis ($\emptyset_y$) via equation (3.5).

In order to facilitate the visualization of lattice orientation changes in the nanoparticles, a map of the calculated mistilts at each pixel position of the VDF reconstruction was built. Figure 3-22 shows the results from a Te nanorod with width of 292 nm length, where the 4D-STEM data was acquired with a camera length L = 245 mm. The scanned region had an area of 17 by 115 pixels with a step size of 3 nm, with an electron dose of 2.7×10^5 $e^- nm^{-2}$. The ADF image and VDF reconstruction of this nanoparticle are shown in Figure 3-22-a and b, respectively. Three different probe positions along the particle, shown in Figure 3-22-c, show

a clear change in mistilt about the zone axis direction along the nanoparticle c-axis. The map of the twist associated with the rotation of the atomic arrangement around the c-axis, i.e. that gives evidence of the presence of a screw dislocation, is shown in Figure 3-22-d (top). In addition to this twisting, it is possible to extract out-of-plane bending presented as a colormap in Figure 3-22-d (bottom).

In order to estimate an overall twist value and associated errors, fits with different numbers of diffraction disks were performed to obtain an average fit. The fitting presented in Figure 3-22 was calculated using 15 disks, so additional minimizations were performed using 10 and 12 disks. Figure 3-23 shows a line profile across the nanoparticle with the mean twist values across the short axis for each of these three fits. Linear regressions were used to calculate the mean twist rate and error. Interestingly it can be seen in the line profile that the twist rate is roughly linear across the central region of the nanoparticle but deviates at the ends. Therefore, the slope of the line that best fits to the data gives the average twist rate, however it should be noted that the twisting rate is not constant over the whole nanoparticle length. As it is predicted that the Eshelby twist of a material is inversely proportional to its radius, this may be the reason that the degree of twisting increases at the nanoparticle apexes, where the diameter tapers.

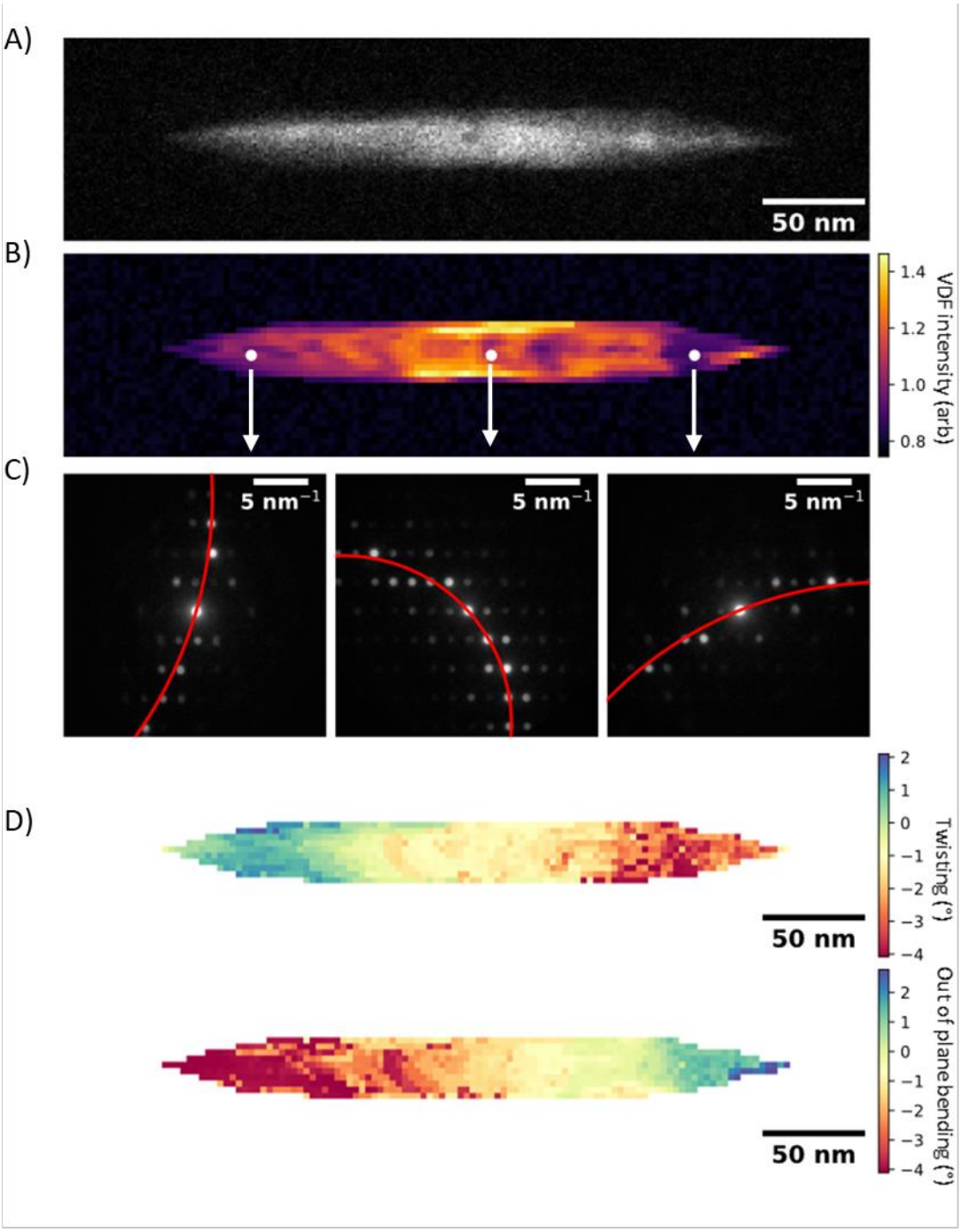

Figure 3-22 Orientation maps of the Te crystal orientations at each pixel acquired from the 4D-STEM data acquired with L = 245 mm and convergence angle α_c = 0.48 mrad. The NBED patterns were recorded for beam positions in a rectangle with dimensions 17x115 pixels and step size of 3nm**.** (A) A STEM image of the Te nanoparticle that the data was taken from (B) A VDF image from the same particle. (C) Diffraction patterns from three different pixels along the particle, showing, twists along two different axes. (D) Top: A map of the twist along the c-axis. This is the Eshelby twisting associated with the screw dislocation. Bottom: In addition to this twisting, it is possible to extract the out-of-plane bending.

There are two possible linear regressions for the data. The first one, indicated by the red curve is the line that passes through the maximum and minimum twist values, and is equivalent to taking two points at the extremes of the nanoparticle and dividing the angular difference by the length, which yields 0.023 ± 0.001 degrees/nm. The second regression, indicated by the black line is the linear regression that best fits the whole line profile (smaller residuals) and has a lower twist rate of 0.011 ± 0.001 degrees/nm, instead.

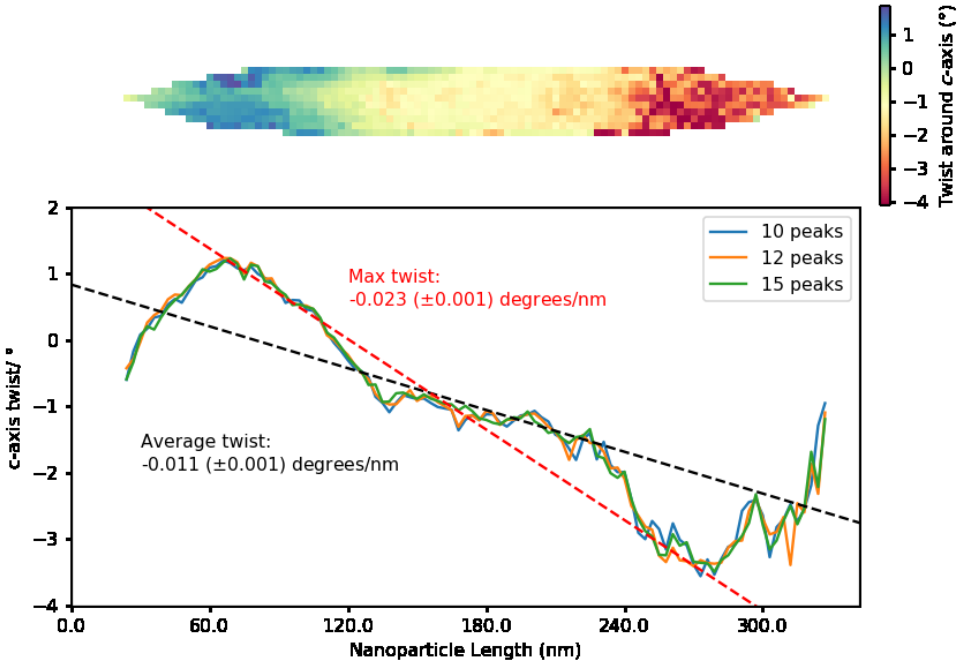

Figure 3-23 Maximum and average twist around the c axis for a Te nanorod with length of 292 nm.

3.3.3 VDF reconstructions for the identification of diffraction contrast of screw dislocations

In addition to the Laue circles fitting analysis, further evidence of the presence of screw dislocations can be investigated through virtual reconstructions.

The presence of screw dislocations distorts the crystal lattice bending it laterally and through the specimen[1], producing dark lines of contrast due to the additional diffracted electrons[104]. In conventional TEM, the diffraction contrast associated with a screw dislocation

is invisible when the sample is oriented in such a way that all the excited reciprocal lattice vectors ($\vec{g}$) are perpendicular to the Burgers vector, i.e. $\vec{g}.\vec{b} = 0$. The dislocation contrast will only be visible when the sample is oriented with the Burgers parallel to the cross-product of two non-collinear $\vec{g}$ vectors that make the dislocation invisible ($\vec{b} \times (\overrightarrow{g_1} \times \overrightarrow{g_2}) = 0$)[104]. This condition is known as two-beam condition. Achieving this imaging condition to observe a screw dislocation is sometimes very difficult due to the instability and mobility of screw dislocations. The limited tilt range in TEM is another inconvenience that makes the identification of screw dislocations more difficult.

Another way to identify the presence of screw dislocation is through the presence of twist contours, which are another diffraction effect from the disturbance of the screw dislocation in the lattice. The object has to be oriented in a way that the two $\vec{g}$ vectors that are non-collinear with the axial direction are excited[103,113,129,130]. The real space twist angle τ is then calculated by[104]:

$$\tau = \frac{\Delta\theta}{l} = \frac{\lambda}{2l}\left|\frac{\overrightarrow{g_2} - \overrightarrow{g_1}}{sin\ \beta_g}\right| \tag{3.8}$$

Where λ is the electron beam wavelength (1.9 pA for 300 kV), l is the measured real space distance between the bands and $\overrightarrow{g_1}$ and $\overrightarrow{g_2}$ are the $\vec{g}$ vectors in the reciprocal space and β is the angle between $\overrightarrow{g_1}(\overrightarrow{g_2})$ and the axial direction.

Meng at al.[131] have recently studied the twisting rate of Copper nanowire through twist contours. In their SAD study of twist contours, an aperture was used to isolate specific reflections which showed as localized contours across the nanowire diameter. The local twisting magnitude was calculated from two sets of these contours and was found to be of the same order as the expected Burgers vector for copper. A similar result was found for ZnO

nanowires[130] demonstrating the material independence of the technique. As a virtual aperture in 4D-STEM is analogous to an aperture in electron diffraction, twist contour analysis can be performed from 4D-STEM data if the nanomaterial in question exhibits a twist.

As mentioned earlier, virtual reconstructions can also help to overcome the mechanical limitations just mentioned above, since in a 4D-STEM experiment an entire set of signals is acquired. The selection and combination of specific spots to make these reconstructions[6] allow the identification of screw dislocation features that would otherwise be invisible using conventional TEM diffraction-contrast imaging. A very instructive reference for the use of virtual reconstructions for this purpose, i.e. to allow the identification of defects, is the work published by Rauch and Véron, where they show multiple examples using different materials, that screw dislocations and defects could be evidenced with the reconstructions depending of the selected diffraction spots[6].

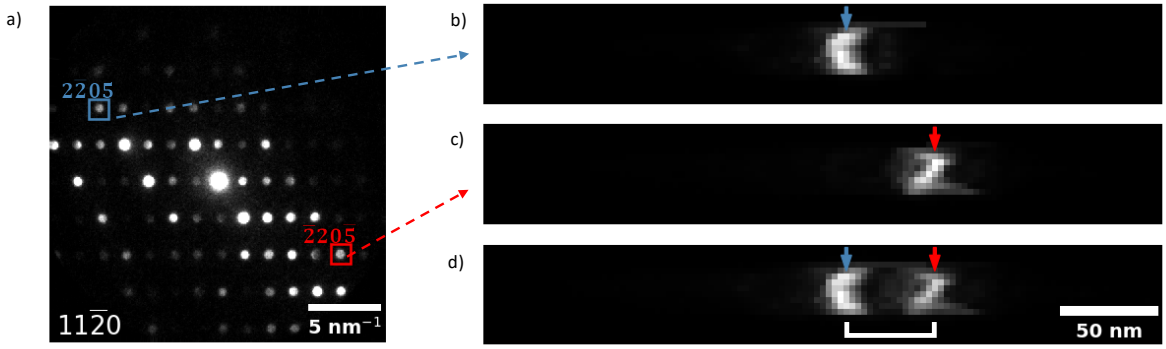

Figure 3-24 VDF reconstructions evidencing the twist bands contained in the same Te nanorod shown previously. a) One of the NBED pattern acquired in the 4D-STEM experiment, b) The VDF reconstruction from the spot $2\bar{2}05$ reveals a twist band c) a second twist band is evidenced from the collinear disk $\bar{2}20\bar{5}$. d) the VDF reconstruction from both disks.

The analysis performed using the virtual reconstructions of the same nanoparticle analysed in the previous section revealed the presence of twist band contours, as shown in Figure 3-24. From equation 4.13 the resulting Eshelby twist is $\tau = 0.04\ (\pm 0.01)^{\circ}/nm$, since

$\lambda = 1.9$ pm (for an electron beam energy of 300 kV), the measured real space distance between the bands is $l = 45$ nm, the difference between the $\vec{g}$ vectors in the reciprocal space $|\overrightarrow{g_2} - \overrightarrow{g_1}| = 2 \times 0.99\ (\text{Å}^{-1})$ and $\beta_g = 27.5^{\circ}$. Since the value of τ depends of the twist band location, the errors were determined from the standard deviation of three different twists using distinct band distances l_1, l_2 and l_3. The distance l_1, was determined by two points in the external edges of the twist band, l_2 was measured with two points chosen in the middle of the bands and l_3 was determined from two points in the internal edges of the band.

The calculated real space twist (τ) coincides with the local twist measured in the Laue circle analysis, demonstrating consistency between the results obtained from these techniques.

Using another pair of disks for the VDF reconstructions (Figure 3-25), the local calculated twist was $\tau = 0.03(\pm 0.02)^{\circ}/nm$, for a measure distance between these bands is l = 27 nm, and the difference between the $\vec{g}$ vectors in the reciprocal space $|\overrightarrow{g_2} - \overrightarrow{g_1}| = 2 \times 0.77\ (\text{Å}^{-1})$ and $\beta_g = 90^{\circ}$.

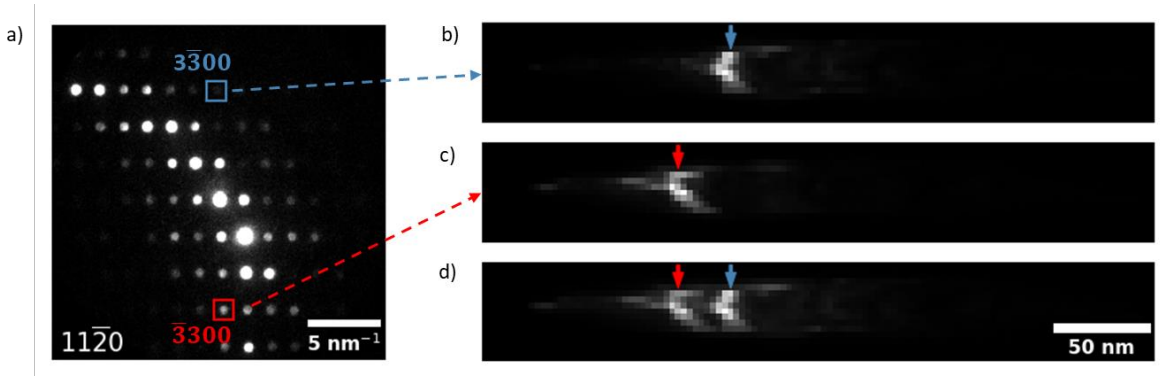

Figure 3-25 Additional VDF reconstructions evidencing the twist bands contained in the same Te nanorod shown previously. a) One of the NBED pattern acquired in the 4D-STEM experiment, b) The VDF reconstruction from the spot $3\bar{3}00$ reveals another twist band c) a fourth twist band is evidenced from the collinear disk $\bar{3}300$. d) the VDF reconstruction from both disks.

3.4 Conclusion

This chapter presented the investigation of the mechanisms for the formation of chiral morphologies in Te nanoparticles. The growth process in chiral nanoparticles is a longstanding subject of interest in the multidisciplinary literature but with very little in-depth understanding of its mechanisms.

The results from the first tomography dataset from the Te bipyramids prepared with chiral ligands and the additional statistics performed from the SEM images, suggested that the presence of chiral ligands induces the formation of one of the two enantiomers, and therefore left and right-handed nanoparticles do not form with the same abundance. It is intriguing and still an open question what the exact role of the ligands is, i.e., if they interfere in the chirality of the crystal lattice and via this route determine the handedness of the screw dislocation, or whether they actually directly affect the handedness of screws, without changing the chirality of the atomic crystal structure.

Another important mechanism presented was the chiral shape formation in crystals without chiral ligands. This result was never previously reported in the literature and the origin of the chiral morphology can be supported by the nanoparticle growth mediated by a screw-dislocation. Although the screw dislocations were not identified through TEM imaging, strong indications of their presence were found, such as: i) the chiral shape at low supersaturation, ii) the non-chiral shape at high supersaturation, and iii) the presence of voids in the chiral nanoparticles, suggest that the screw dislocations might have suffered plastic deformation.

The 4D-STEM measurements complement the results from the analysis of the electron tomography experiments and gave more evidence that polyhedral chiral shapes originate from screw dislocations in Te – and makes more remote the possibility that chirality of the shape originates from differential growth rates of facets; since this type of growth would be induced

by chiral ligands or by the chiral crystal structure, as growth processes mediated by these factors should not be accompanied by lattice twisting.

Moreover, the versatility of the 4D-STEM technique was demonstrated, where a rich range of crystallographic information can be extracted from these datasets. A new analysis technique was presented where the zone-axis mistilt along the nanoparticles could be quantified through fitting the Laue circle. Moreover, another significant analysis method developed was the observation of contour bands using VDF and VBF for quantification of the lattice twist. The main advantage of the use of 4D-STEM is that a wide range of information can be acquired from these datasets without the mechanical limitations of conventional TEM. It is worth noting that the techniques implemented here are based on fundamental electron microscopy knowledge and because of their general applicability, they can be used to investigate the 3D structure of different materials.

Furthermore, the chiral shapes of nanoparticles are of relevance for many fields - such as optics, chemical catalysis and drug-delivery [85] – and the concepts presented in this thesis bring important contributions towards the fundamental knowledge of crystal synthesis.

4 Electron tomography of polymer grafted gold nanoparticles

This chapter presents the STEM tomography of 3D gold polymer grafted nanoparticles (PGNP) and the investigation of their lattice structures.

The structure of this chapter is as follows: Section 4.1 gives an overview of the studied nanoparticle crystals and the features of interest. Section 4.2 is dedicated to explaining the details of the experimental setup. Section 4.3 shows the tomography datasets as well as the alignment and reconstruction techniques performed for each nanoparticle. Section 4.3 presents the main results from the 3D reconstructed data and details of the lattice structures of these nanoparticles. Finally, in section 4.4 the main conclusions from the experiments and analysis are discussed.

4.1 Polymer grafted gold nanoparticles

Self-assembly is any process where the disordered units of a system are assembled forming an ordered larger structure spontaneously and without external intervention[132].

Self-assembly of smaller building blocks into ordered crystalline solids is a very interesting problem that can be observed on diverse scales and fields**.** Normally, the term *self-assembly* is employed to individual structures that are bonded via weak forces, such as Van der Waals forces or hard-particle interactions, instead of primary bonds such as covalent bonds [133]. On the micrometer scale for example, opals are formed from silica microparticles. The difference between a common colorless opal and its rare colorful variety is that the former is composed from the amorphous aggregation of silicon particles, whilst in the latter these particles are assembled into crystalline structures. The level of order in these crystals and the

size of the constituent particles (1.7-3.6 μm), determines the diffracted colors (and of course their price!).[134]

On the nanometer scale this type of system is formed from inorganic nanocrystals and similar to the case of atoms in nanoclusters, the ensemble of nanoparticles can display different properties from the individual nanoparticles and bulk materials, which depend on the material, size and geometric crystal arrangement (e.g. FCC, BCC and HCP)[135,136]. The three dimensional ordered assemblies of nanocrystals are also commonly referred to as *superlattices* in the literature[137–139].

Self-assembly of colloidal nanoparticles can occur when the surfaces of the nanoparticles are passivated by soft organic ligands[140] – often sulfur-based ligands, such as thiol groups due to their high affinity for noble metals[133,141] – which prevents disordered nanoparticle aggregation[142]. These functionalized nanoparticles are then immersed in a solution that favors their ordered association.

There are many techniques for the deposition and assembly of the nanoparticles, where arguably the simplest and most common technique is driven by evaporation of the solution on a substrate (*drop cast* method)[143] . During these processes the nanoparticles organize spontaneously forming structures while the solvent is drying[144], and nanoparticle structures form on the liquid/gas boundary due to high nanoparticle concentrations. The level of order in these structures depends on the assembly environment and the interactions between the nanoparticles. Normally, monodisperse colloidal nanoparticles assemble into ordered structures under slow evaporation rates or destabilization of the solution[137], however the evolution of processes that lead to structure formation is still not fully understood.

Since there are many parameters that need to be controlled – including the solvent, ligands, temperature, evaporation rates, etc. - these techniques currently have limited control

over the resulting structures and geometries, leading to the presence of amorphous aggregates in varying proportions, depending on the energy of evaporation of the solvent[145].

Other techniques to guide the self-assembly of colloidal nanoparticles, during the evaporation process include DNA nanotechnology[146,147], and polymer grafted nanoparticles. The DNA technique consists of using synthetic DNA to carry information to guide the nanoparticle assembly[132]. The drawbacks of this method are that the DNA molecules normally have poor electrical and thermal properties. Substrate immersion methods are also often used[148].

Evaporation techniques can lead to the formation of 2D monolayers[133] and 3D lattices with various crystalline structures such as FCC, HCP and BCC[140]. There are several conditions which affect the structure of the assembled nanoparticle, such as the structural and chemical properties of the ligands, solvent composition and the substrate. Normally, superlattices of spherical nanoparticles and short ligands[149] assemble as FCC or HCP[150] - where FCC is slightly more stable (10^{-3} k_BT/nanoparticle) than HCP[151]. Because these structures have very close free energy, often they form simultaneously and the experimental conditions determine which one predominates[150]. Normally, when the growth of crystals is treated as hard-spheres, thermodynamic effects lead to FCC structures, since it is the most energetically favourable structure. Kinetic effects might favour the generation of HCP structures, but since the energies between HCP and FCC are so close, the resulting structure will often be random hexagonal closed-packed (RHCP)[152,153], which has equal FCC and HCP stacking probabilities between layers. The overall small differences in energy also leads to the presence of faults, such as 1D vacancies and line defects[153].

Bcc structures are normally formed when ligands with longer lengths are used[149]. In fact, the ratio between the ligand length and the radius of the nanoparticle ($\lambda_s = L_{lig}/r$) is a critical parameter to determine the resulting structure. A common generalization in the field is that when λ_s is less than 0.7 the nanoparticle self-assembly can be described by a hard-sphere

assembly model and therefore will result in the formation of FCC/HCP structures. On the other hand, at higher λ values, the nanoparticles behave like soft-spheres and will organize with non-closed packed structures, which is the minimum energy structure[154]. However, Yun et al. have shown that this is not always the case. They demonstrated that PS coated nanoparticles with λ_s higher than 3 transitioned from BCC to FCC when increasing the grafting density Σ (i.e. the number of bound polymer per surface area) from 1.10 to 1.53 chains/nm[154].

It is important to note that controlling the length-to-core ratio is effectively controlling the polymer molecular weight, as shown by Ye et al[155]. In their work, by varying the molecular weight, the interparticle distances and structure of the nanoparticle could be controlled.

The choice of solvent also has an important role in the resulting lattice structure. Wei et al showed that the crystalline structure of 3D silver colloidal nanocrystal superlattices evolved from BCC to FCC when the solvent was changed from hexane to trichloroethylene (TCE)[156].

In the work shown in this chapter, self-assembled gold nanoparticles were prepared with the addition of polymers in an attempt to optimize their growth rates. The addition of polypropylene (PP) and uncontrolled solvent evaporation led to the formation of the 3D layered structures. By comparison, the formed structures were 2D monolayers without addition of PP. Moreover, varying the polymer ligand generated different structures and electron tomography was performed to better understand the overall lattice structure. In the next section the data acquired for different growth conditions are shown.

4.2 Electron tomography experiments and reconstruction

4.2.1 Electron tomography data acquisition

The samples were prepared by Yiwen Qian from the group of Professor Ting Xu, in the Department of Materials Science and Engineering at University of California, Berkeley.

The Au polymer grafted nanoparticles were synthesized by ligand exchange with thiol end-functionalized polystyrene (PS) and they were dispersed in toluene solution. The experiments were performed with different ligand molecular weights (M_n) and in this thesis two of them are shown, namely M_n= 1300 g/mol (1.3k) and M_n = 3800 g/mol (3.8k). The core size of the resulting nanoparticles was 4.0 nm and the capping polymer used was PP. The solution was drop-cast onto a TEM grid and allowed to dry under ambient conditions, forming the Au self-assembled superlattices.

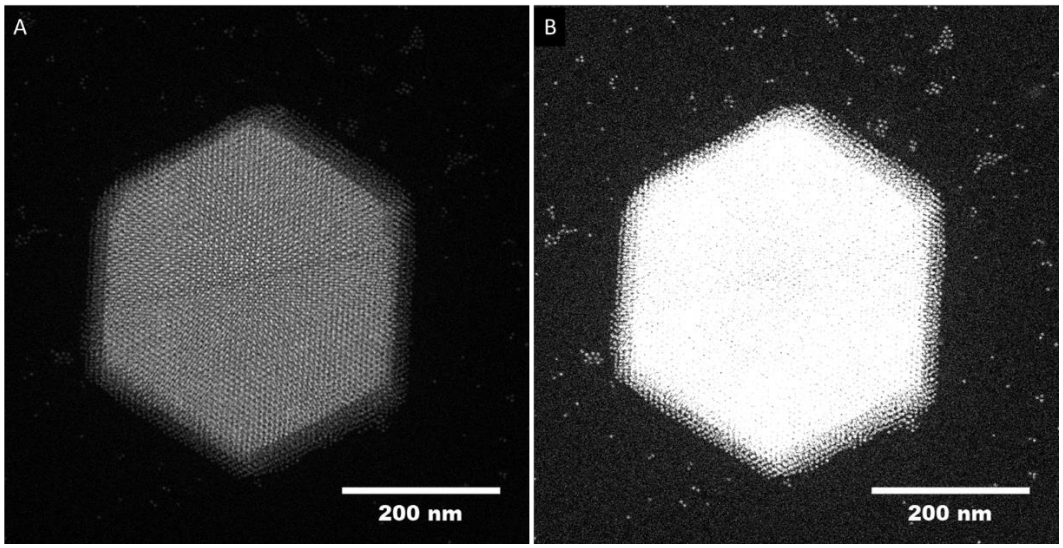

Figure 4-1 ADF-STEM images from one of Au PGNP datasets (4.0nm, 1.3k) from which the tomography data was acquired. A) An image with the full range of intensities and where the NP assembly features are more evident B) The same image with different contrast, where the maximum intensity was clipped, in order to show the single nanoparticles dispersed on the grid (fiducial markers).

Since there were many single nanoparticles dispersed on the grid, which were dissociated from the main self-assembled superlattice, these were used as fiducial markers, to align the tomography series (Figure 4-1).

Both tomography experiments were performed using an FEI Titan microscope operated at 300 kV. The ADF-STEM images were acquired with a 10 mrad probe semi-convergence angle and ADF detector with inner collection angle of β_c = 55 mrad. Typical images were 1024x1024 with a dwell time of 15 μs.

The tomography dataset from the 4.0nm (1.3k) Au nanoparticles was acquired over the range of -75˚ to 70˚ with a step size of 1˚, pixel size of 0.91 nm and with an electron beam dose of 2.5×10^3 e^- nm^{-2} $frame^{-1}$. However, these samples had carbon contamination growth during data acquisition – and this could not be improved even after electron beam showering and plasma treatment (Figure 4-2). Therefore, the projections higher than 66° needed to be excluded because they generated undesirable artefacts as the blurring caused by the contamination affected the tracking and dynamic focusing performed by the acquisition tomography software.

The tomography experiment from the 4.0nm (3.8k) Au NCs was accomplished over the tilt range of -70˚ to 70˚, with 2˚ step size, pixel size of 0.63 nm and with an electron beam dose of 5.3×10^3 e^- nm^{-2} $frame^{-1}$.

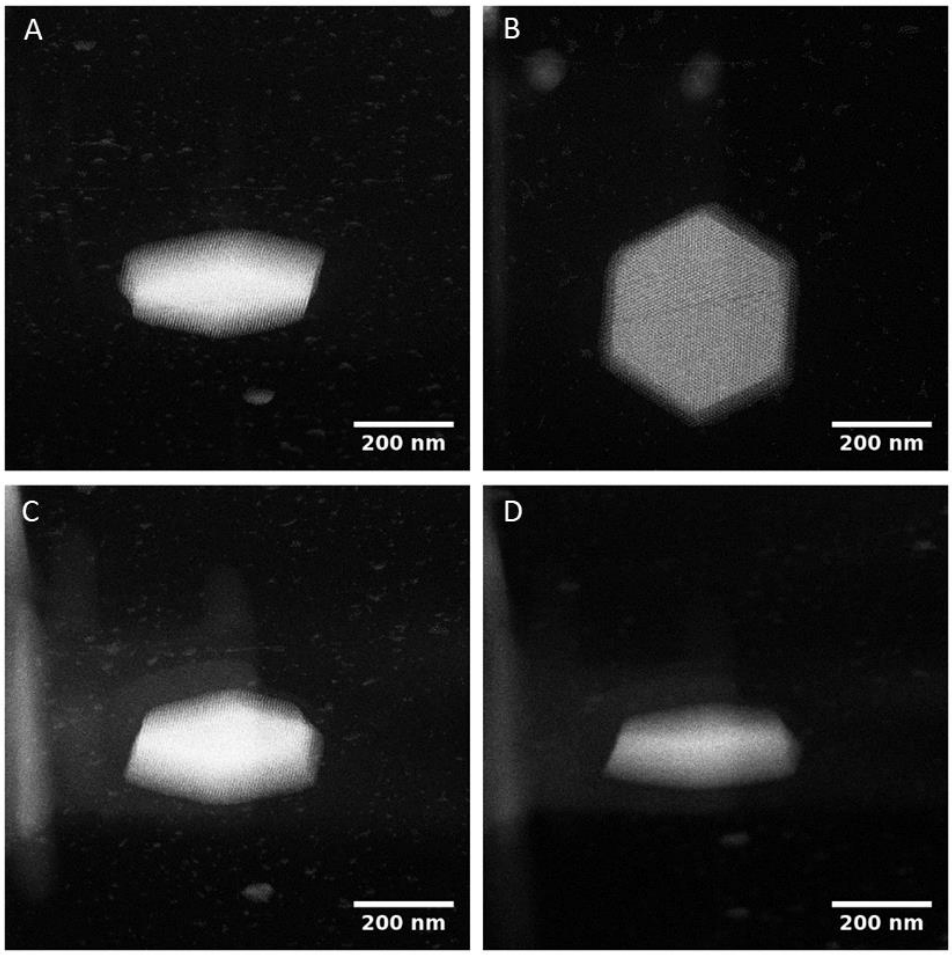

Figure 4-2 STEM projection images from a 4.0nm (1.3k) Au nanoparticle showing contamination growth during the acquisition. A, B) ADF-STEM image acquired at -75°, the first tilt angle of the data series, and at 0°, respectively. C, D) Projections acquired at 66°, the last projection used for the reconstruction, and 70°, respectively.

4.2.2 Electron tomography alignment and reconstruction

The alignment and reconstructions of both tilt series were firstly tried on IMOD (version 4.9.10), as performed for the other datasets presented in the previous chapter.

However, the alignment of these samples with fiducial markers resulted in reconstructions with artefacts. The main reason for this is that the nanoparticles used as markers varied their positions under the electron beam. Therefore, the nanoparticles in the nanoparticle crystal reconstructed using the fiducial alignment had distorted (moon) shapes - typical of a

misplaced rotation center and scanning distortions, as presented in section 2.7. Figure 4-3 shows these slices for the 4.0nm (3.8k) nanoparticle. These problems could not be fixed using the fiducial alignment functions and parameters contained in the software and therefore, a second sensible trial was to perform a fiducialess alignment, also using IMOD, using cross-correlation. Although the results were better than the alignment using the Au markers, the final result was also unsatisfactory, as can be seen in Figure 4-4, where the vertical cuts show a consistent increase in deformation of the spherical nanoparticle along these slices. Since both trials did not succeed, custom python scripts were written to perform the fine alignment from the cross-correlation aligned stack from IMOD.

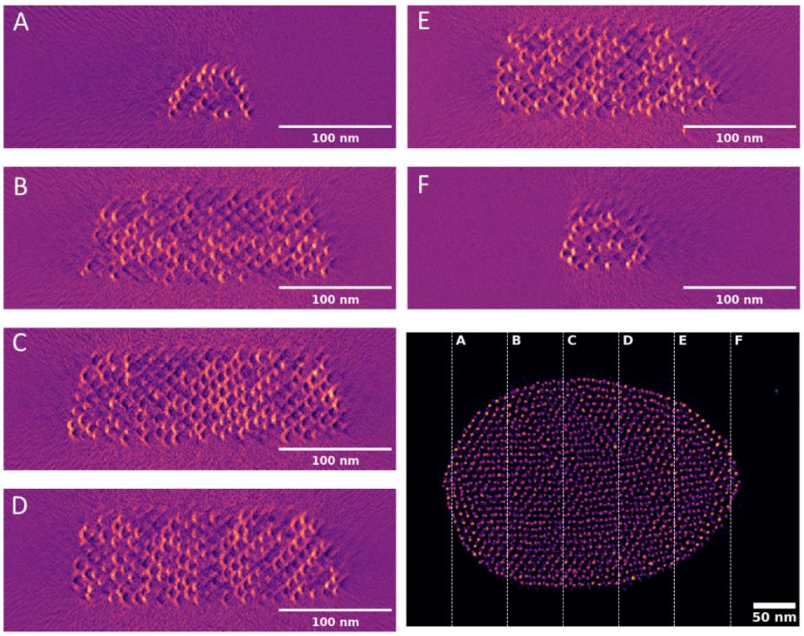

Figure 4-3 STEM tomography reconstructed images showing consecutive vertical cuts along the nanoparticle (as indicated in the bottom right figure). The reconstruction was performed with a fiducial alignment on IMOD and from A) to F) the consistent presence of misaligned artefacts (moon shaped nanoparticles) can be observed.

Considering the vertical cuts shown in Figure 4-4 in the context of the discussion presented in section 2.7.2, it is apparent that the respective sinograms need to be shifted

vertically by linearly increasing amounts from the left-most to the right-most cut. This corresponds to correcting for an image shear in the projections, which could have had its origin for example in sample drift or slightly inaccurate scan-coil calibrations. Figure 4-5 shows the slices after these corrections in the sinograms of the series. The individual cuts were reconstructed applying the *iradon* function from the skimage python package to the adjusted sinogram, and the cuts were assembled to a 3D reconstructed volume.

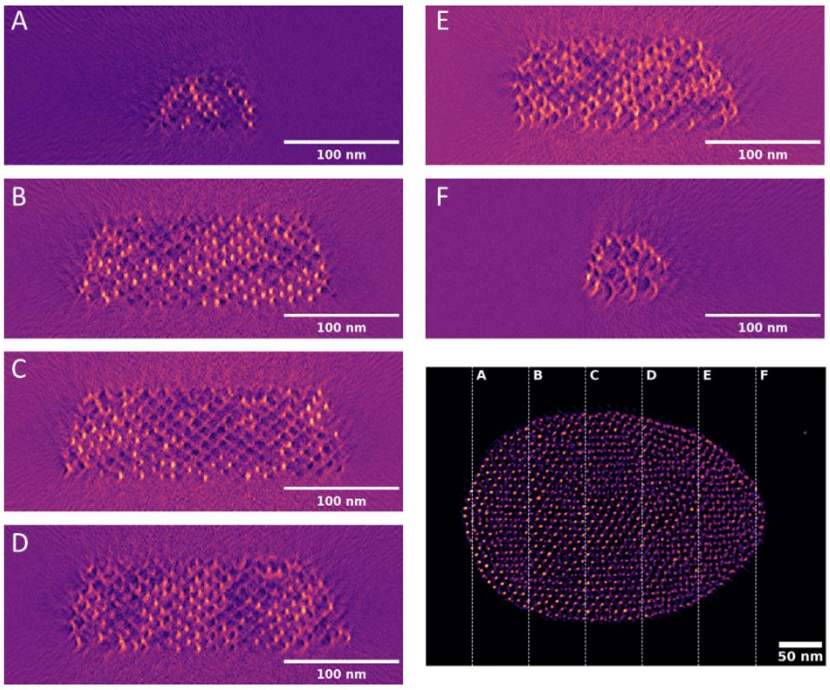

Figure 4-4 STEM tomography reconstructed images showing consecutive vertical cuts along the nanoparticle (as indicated in the bottom right figure). The reconstruction was performed with a cross-correlation alignment on IMOD and from A) to F) consistent increasing of the misaligned artefacts over the cuts can be observed.

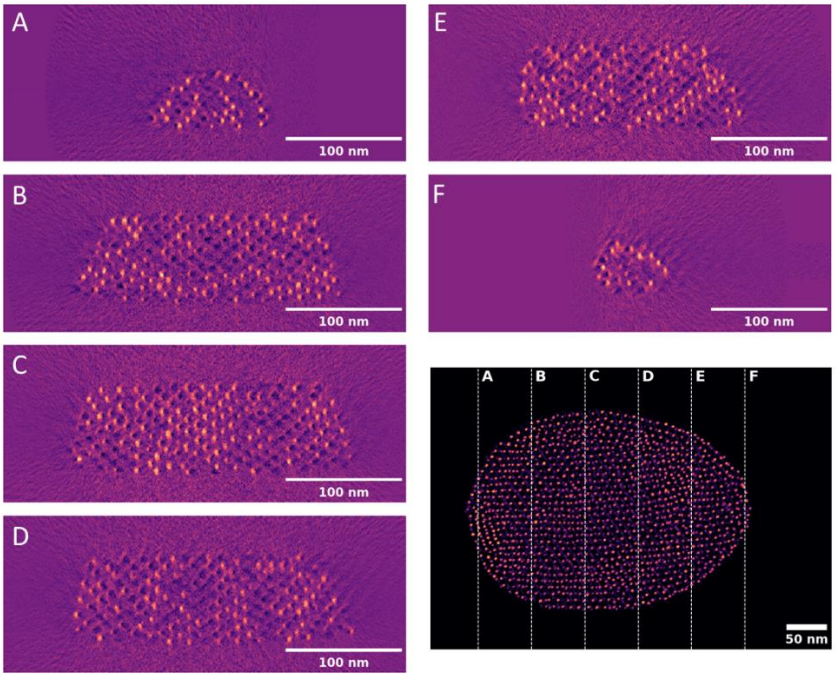

Figure 4-5 STEM tomography reconstructed images showing consecutive vertical cuts along the nanoparticle (as indicated in the bottom right figure). The reconstruction was improved by checking the sinograms and correcting the tilt series and the scanning shifts.

4.3 Electron tomography Results

4.3.1 4.0 nm (PS = 1.3k) Au nanoparticles

As mentioned previously, once the reconstructions were performed, further image processing needed to be implemented to improve the visualization of the overall features of the superlattice, since the high density of constituent nanoparticles obfuscated the perception of depth in the 3D images. Figure 4-6 shows a rendering that improves this aspect by filling the interparticle distances but conserving the larger defects and morphology features. The filled volume was created from the original reconstruction data by simulating the nanoparticles in the lattice as Gaussian peaks and convoluting this data with a spherical kernel.

As shown in Figure 4-6, the overall shape of the nanocrystal shows that the number of layers decreases from bottom to top. This could be an indication that these assemblies are formed by the deposition of Au nanoparticles - contained in the air-solution interface - onto the contact line of the drop and the substrate (or accumulation zone)[157–159].

The distribution of sizes of the nanoparticles were calculated using two functions from the skimage package. First, the function *measure.label* was used to label the individual nanoparticles contained in the volumetric data array, since they are connected regions of pixels. The volume was thresholded to isolate the nanoparticles and the individual constituent nanoparticles were labelled. Two pixels are connected and labelled when are correctly thresholded, have the same value and share a common face.

Once the nanoparticles were labelled, their properties were measured by the function measure.*regionprops*, which allowed the nanoparticle diameters to be calculated. The distribution of the nanoparticle diameters is shown in Figure 4-7. The resulting peak of this distribution, 4.3 ± 0.2 nm agrees with the nominal value of 4.0 nm.

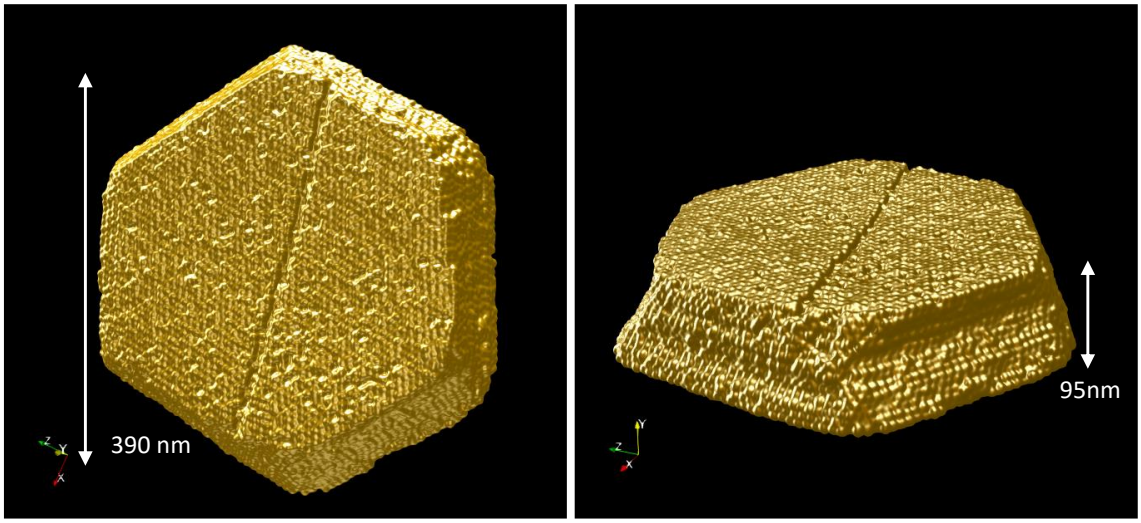

Figure 4-6 Surface rendered views of reconstructed 4.0nm (PS = 1.3k) PGNP tomography dataset. The rendering was made to fill the spaces and show a solid surface in order to evidence the overall morphology of the nanoparticle.

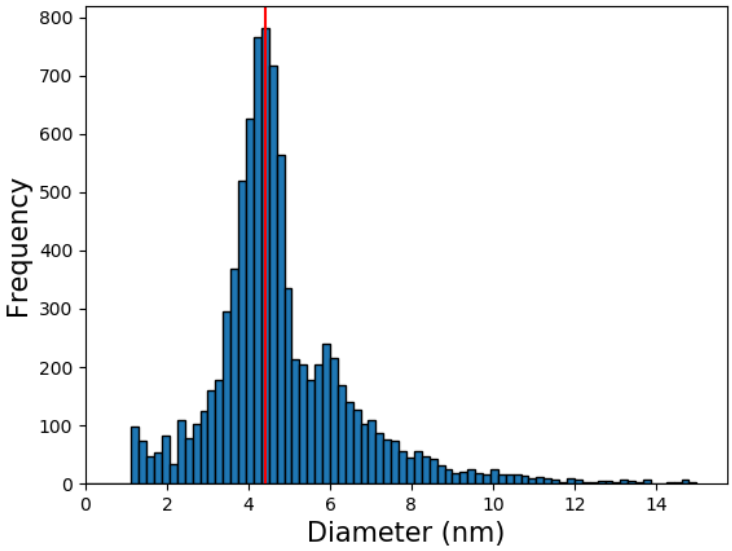

Figure 4-7 Size distribution of the 4.0nm (1.3k) Au nanoparticle. The red line shows the peak diameter which was calculated to be 4.3 ± 0.2 nm. The error on the mean particle diameter was calculated by considering different thresholding techniques including Otsu's adapted threshold[160], the triangle algorithm[161] and Yen's algorithm[162].

The crystal structure of this nanoparticle has a high degree of crystallinity, but its arrangement was not constant throughout the crystal with varying amounts of space between layers and variable packing density in different regions of the superlattice. The variability in local lattice structure is consistent with the fact that nanoparticles assembled with soft organic ligands will always result in some lattice softness.

Another characteristic of the superlattice's shape was that its top and bottom surfaces were bent, as can be seen more clearly in Figure 4-8 (a). Therefore, the surface was flattened only for the purpose of improving the visualization of the top and bottom views. The analysis of the lattice parameters was performed on the original data. The flattening was performed by a custom python script that fits a 2D polynomial mesh grid surface to the top and bottom layers. The nanoparticles are then rolled by the amount given by the deviation of their positions and the flat mesh. The results for the top and bottom surfaces can be seen in Figure 4-8 (b and c).

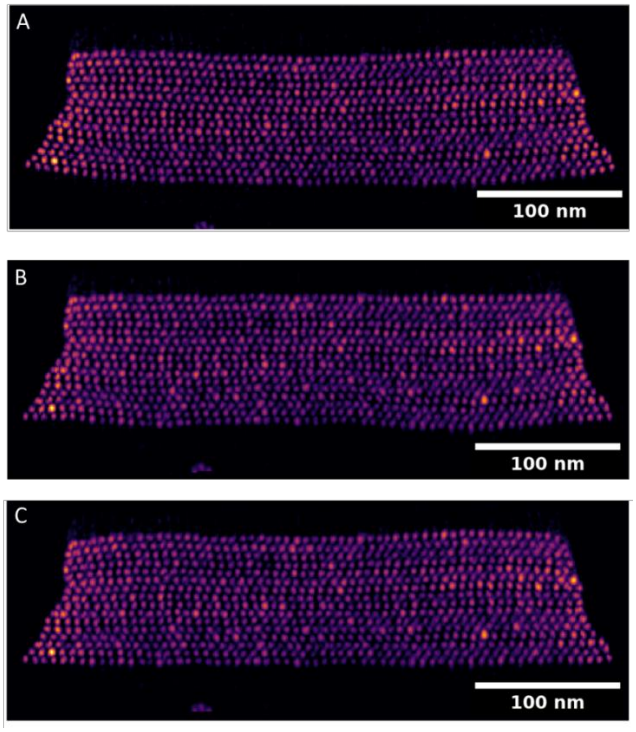

Figure 4-8 Flattening of the 4.0nm (PS = 1.3k) Au nanoparticle surface for the improvement of the top and bottom view visualizations. a) Original side view of the shape b) and c) show the side views of nanoparticle with the flattening of the top and bottom regions, respectively.

Figure 4-9 shows the base and top single layers from the nanoparticle after the flattening, where these views show a distorted hexagonal structure. Ignoring the exact nature of the distortion, this is a dense planar nanoparticle packing which is compatible with BCC(111), HCP(0001) and FCC(111). Therefore, the lattice stacking of the nanoparticles in other orthogonal directions needed to be evaluated to determine the overall lattice structure.

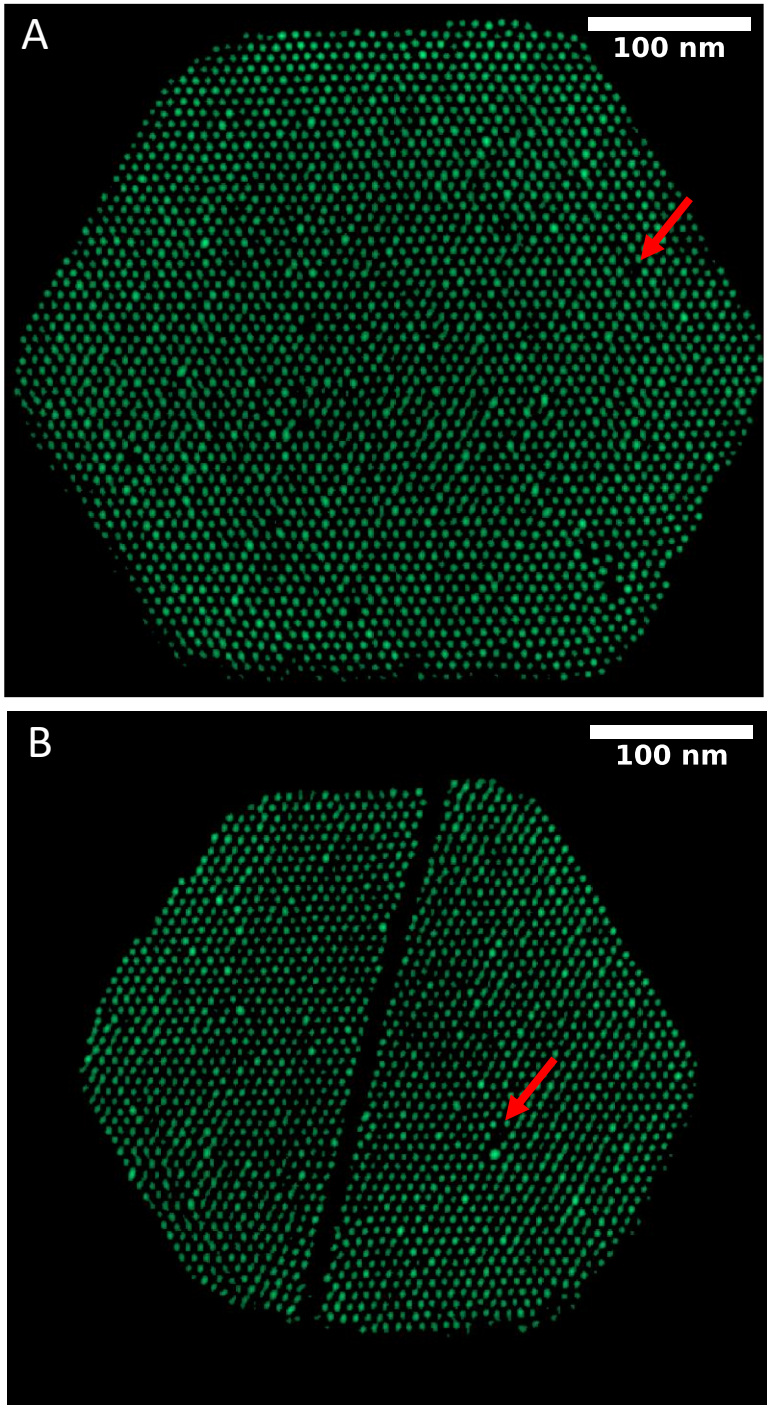

Figure 4-9 In-plane views from single layers of 4.0nm (1.3k) Au nanoparticle A) Bottom plane layer, B) top layer. Both layers show a distorted hexagonal lattice, whereas a big line defect can be observed in the top layer. It is also interesting to note that many single vacancies can be found in both layers. Two examples are indicated by the red arrows.

It was also observed that the structural order increases from the bottom to the top layer, as shown in Figure 4-10 and Figure 4-11. In typical HCP and FCC stacking, the nanoparticles

in the adjacent layer sit in the three-fold hollow of the layer below. Hollow-site stacking is observed towards the center of the bottom two layers. However at the edges of the layer, as shown in Figure 4-10-a, the nanoparticles sit in the bridge-site of the layer below, possibly indicating a transition to BCC structure. This pattern disappears in the upper layers, as shown for the top two layers, which have nearly perfect hollow-site registration (Figure 4-11).

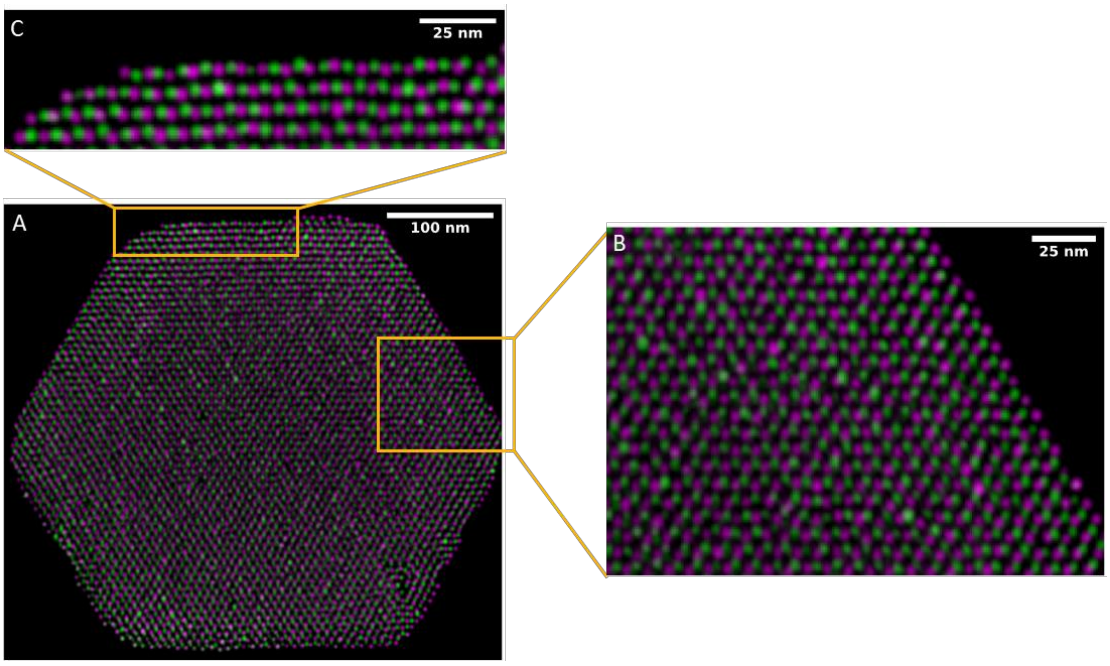

Figure 4-10 a) shows a composite of base and next layer, with different colours representing different layers along the top view. b) This zoomed in region shows the typical NP arrangement observed in most regions, with the 2nd layer NPs located near the center of three 1st layer NPs (hollow site). c) Towards the upper edge the NPs progressively assemble with bridge sites.

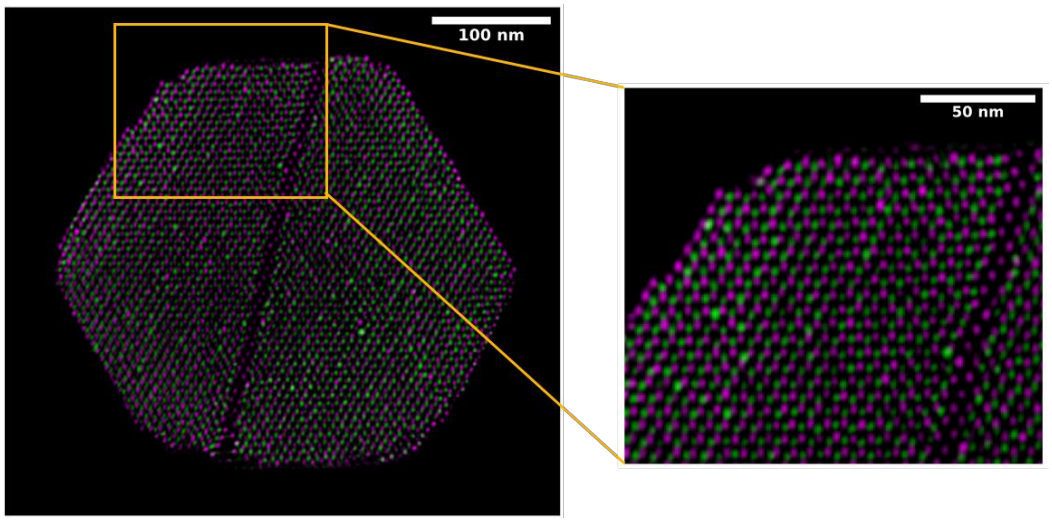

Figure 4-11 a) composite of top and next layer. b) The zoomed in cut shows that the nanoparticles assemble in arrangements nearly perfect hollow on the upper layers.

Figure 4-11 also shows that the top layer has a line fault across the whole nanoparticle diameter. At first look, one could think that this is due to the cracking of the nanoparticle at late stages of the solvent drying. The presence of cracking in nanoparticles is indeed a common defect and occurs when the assembly of the nanoparticles is initialized on the solvent-air interface. Since the nanoparticles contained in the liquid are deposited on the substrate as the evaporation continues, the contraction of the lattice with the solvent evaporation would compete with the adhesion of the nanoparticle bottom plane to substrate[135]. Then, when the solution surface reaches the substrate, the lattice suffers a rupture due to the difference between the curvatures of the liquid interface and the flat substrate[138].

However, further analysis of the nanoparticle structure within the top four layers reveals that the stacking on opposite sides of the line fault are different, as shown in Figure 4-12.

Therefore, it seems more reasonable to interpret these faults as line defects dividing FCC and HCP. The same kind of defect line, acting as an interface between FCC/HCP stacking, has been previously reported on the studies of hard spheres assembled through sedimentation of a colloidal solution[163]. As described previously, the formation of such defects is due to the

competition between kinetic and thermodynamic effects. Kinetic effects result mainly in RHCP structures, whilst thermodynamic effects produce predominantly FCC lattices. However, in systems where kinetic effects are predominant and therefore the overall structure is RHCP, it has been reported that line faults induce the local formation of FCC stacking[152], as is observed for the 4.0nm (PS=1.3k) Au nanoparticles here.

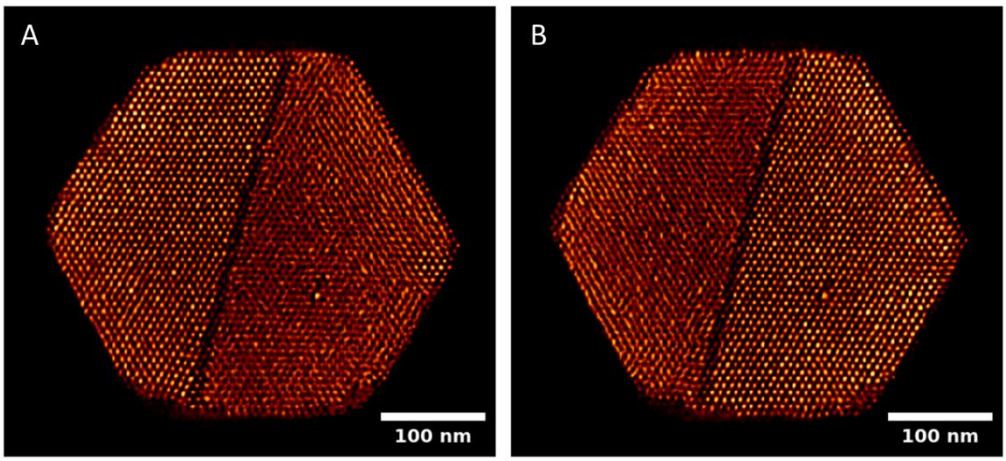

Figure 4-12 Electron tomography slices from the 4.0nm (PS = 1.3k) PGNP showing different stacking in the left (HCP) and right sides (FCC) of the line fault on the nanoparticle. a) Overlay of the first and third layer showing an ABA stacking organization on the left (HCP), and ABC on the right (FCC). (The second common layer (B) was previously shown in Figure 4-11). b) Overlay of the first and fourth layer showing on the left ABAB and right ABCA.

When looking at the overall stacking of the nanoparticle from a lateral view (Figure 4-13), stacking patterns of FCC and HCP with stacking faults (white dashed lines) can be observed. One could interpret the structure as HCP with a moderate number of stacking faults. However, it seems that the stacking faults are randomly inserted, or indeed the stacking sequence itself is random - and therefore it is more accurately described as RHCP, as it seems that FCC and HCP stacking can be observed with equal probabilities[153,164,165].

In RHCP structures, although the periodicity of the stacking along a plane is random, there is long-range positional correlation, since the nanoparticle will always lie in one of the

positions *A, B* or *C*[153], as observed in this nanoparticle. There are different ways to calculate the level of order of a RHCP. One of them is to calculate the probability of finding a FCC stacking among three randomly consecutive layers[153], and in this case for the arrangement shown in Figure 4-13, the probability of finding FCC stacking is 0.43.

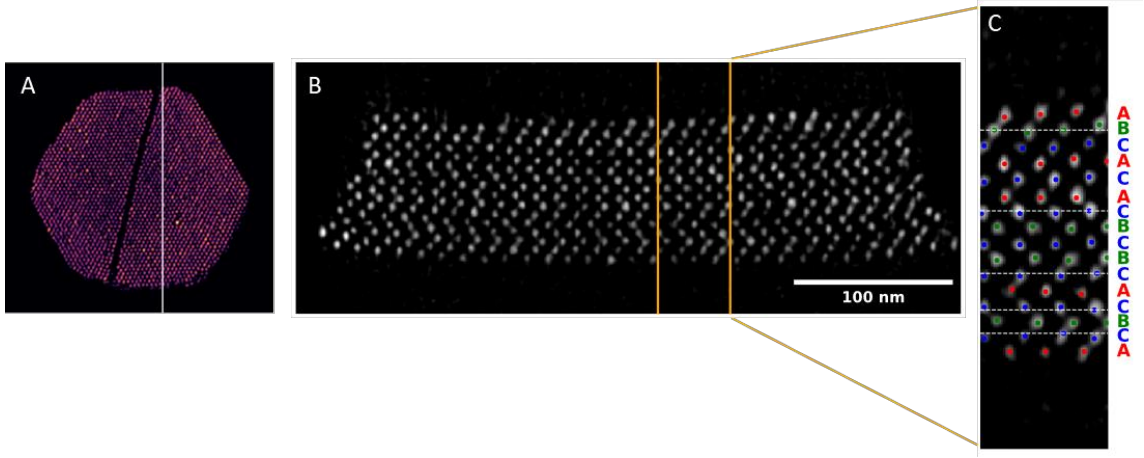

Figure 4-13 Assembling of the layers from a single vertical cut from the reconstruction volume of the 4.0 nm (1.3k) Au nanoparticle crystal. (a) shows an in-plane view with the line cut indicated by the white line. b) and c) show the stacking of the layers, which are a mixing of HCP and FCC stacking.

To perform more accurate statistics from the lattice parameters of the 4.0nm (1.3k) Au nanoparticle, a nearest neighbourhood (NN) analysis was performed.

To give an overall idea of how the algorithm worked for this analysis, the query of the NN was performed using the function *KDTree* from the scipy package[122], which organizes the data into a tree structure. The two-point correlation function then calculates of the cumulative NN distribution as a function of r, $F_{nn}(r)$, and the gradient of this function $dF_{nn}(r)/dr$ calculates the radial distribution function (RDF)[166]:

$$RDF(r) = \frac{1}{4\pi\rho r^2}\frac{F_{nn}(r)}{dr} \tag{4.1}$$

Where ρ is the average density of nanoparticles, i.e. the ratio between the total number of nanoparticles and the total volume of the superlattice (N/V). The total number of nanoparticles was calculated using the functions *blob_log* from the skimage package, while the volume was calculated using the *convex.hull* class from scipy. The calculated number of individual nanoparticles in the 4.0nm (1.3k) Au superlattice was 32878 nanoparticles. The surface area and volume of the superlattice were calculated to be $4.3 \cdot 10^5$ nm^2 and $1.7 \cdot 10^7$ nm^3 respectively from its convex hull. This yields a number density of $\rho = 2 \cdot 10^{-3}$ nanoparticles/nm^3 and a surface area to volume ratio (S/V) of 0.026 nm^{-1}.

The RDF function was calculated for $0 < r < 30$ nm and is shown in Figure 4-14-a. Thus, the peaks in the RDF indicate shells of neighbours and the valleys indicate the shell limits. For this dataset r = 9 nm indicates the end of the first shell. The first peak corresponds to the first shell of NN and it is at r = 7.2 nm. This value corresponds to the mean interparticle nearest-neighbour distance.

To check the consistency of this value, a histogram was plotted, from a query from the *KDTree* performed by the function *query_radius,* where a radial distance of 9 nm was used to calculate the number of NN. (Figure 4-14-c). The modal number of neighbours within the first shell, i.e., 1st nearest neighbours, is 12. This is consistent with both HCP and FCC lattices, and therefore is further evidence indicating and RHCP structure.

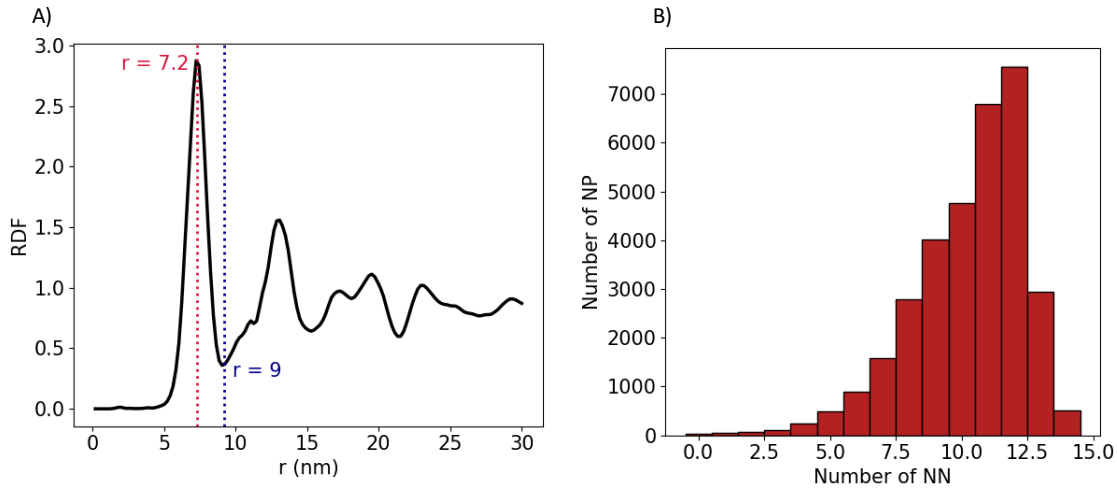

Figure 4-14 a) RDF function showing the average radius of the first NN shell (r = 7.2 nm) and b) the end of the first NN shell (r = 9 nm).

The histograms of the NN in three orthogonal directions are shown in Figure 4-15-a. Simulations from FCC and HCP structures generated with the in-planes [111] and [0001] directions, as well as the orthogonal directions to these axes, are also show in Figure 4-15-b. These simulations were performed using the Atomic Simulation Environment (ASE)[167] python library. The projections of the NN data in the zx direction matches with the HCP $[11\bar{2}0]$, giving more evidence of a RHCP structure. The small differences between the experimental patterns and the simulations likely arise due to the softness of the superlattice, meaning that there are small discrepancies in stacking positions as discussed previously.

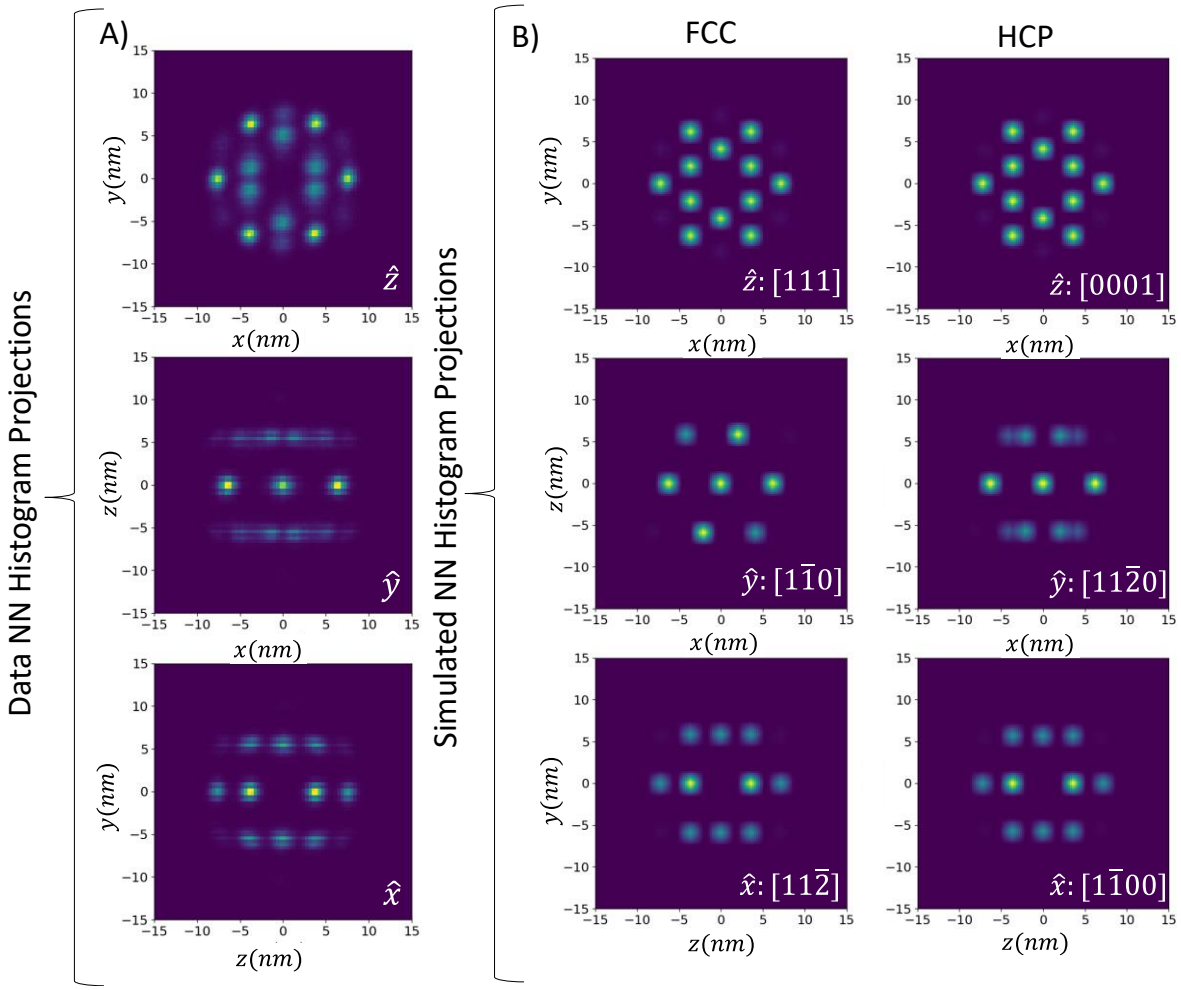

Figure 4-15 Histograms projections of the NN for a shell with radius r = 9 nm. a) from original data b) simulated data for FCC and HCP lattices at the directions indicated (left lower corner). The projections of the NN data in the zx direction matches with the HCP [11$\bar{2}$0].

4.3.2 4.0nm (3.8k) Au nanoparticles

As mentioned previously, the second nanoparticle was synthesized with a higher polymer molecular weight. The 4.0 nm (PS = 3.8k) Au nanoparticles had a different morphology and lattice arrangement. The overall 3D shape can be seen in the rendered view in Figure 4-16.

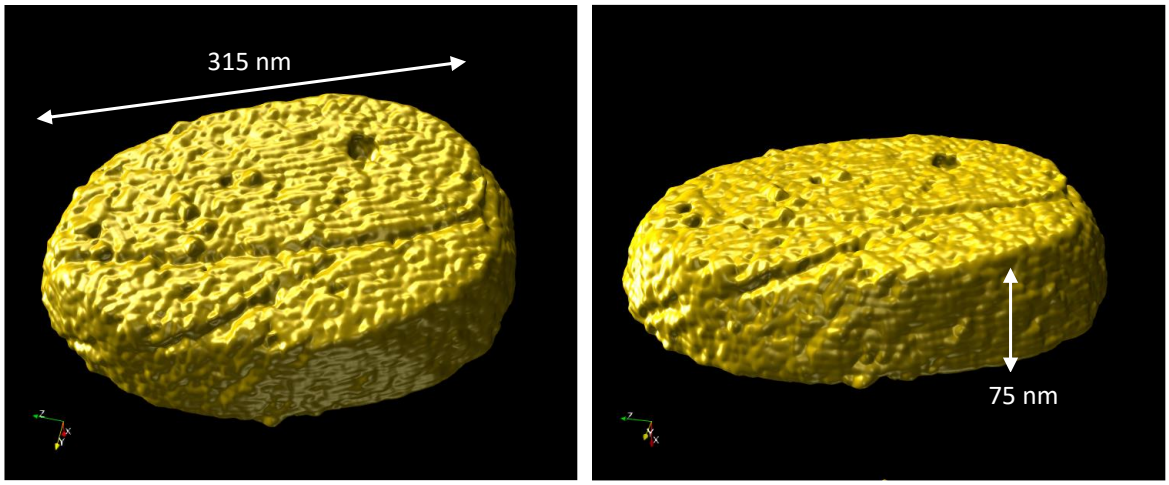

Figure 4-16 Rendered volume of the 4.0 nm (PS = 3.8k) Au nanoparticle. The rendering was made to fill the spaces between the nanoparticles and show a solid surface in order to evidence the overall shape of the nanoparticle as well as the defects on the top layers.

A size distribution (Figure 4-17) was calculated from the reconstructed volume using the same method as described in the last section. It yields a nanoparticle size of 3.8 ± 0.2 nm, in agreement with the nominal value.

In this superlattice, the planes parallel to the growth direction also showed a distorted hexagonal lattice, as shown in Figure 4-18. The registration between the layers is predominantly bridge sites, thus the in-plane view from nanoparticle lattice is compatible with the BCC[111] crystal structure. The crystal lattice of this nanoparticle also shows the presence of vacancies and lines defects.

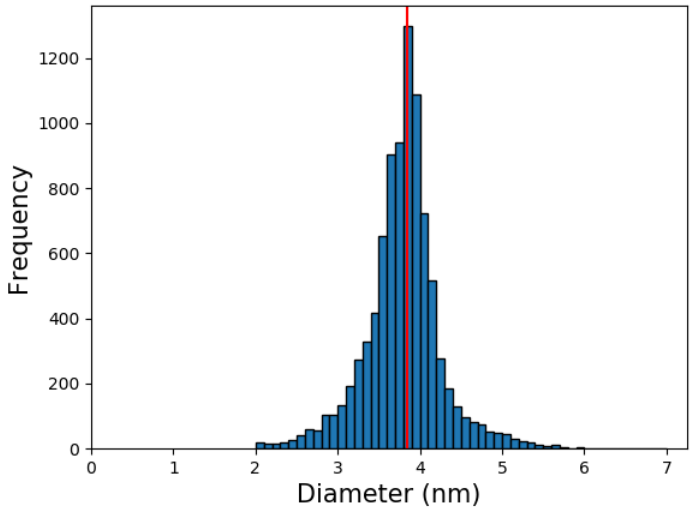

Figure 4-17 Size distribution of the 4.0 nm (3.8k) Au nanoparticle. The red line shows the diameter peak at 3.8 ± 0.2 nm. The errors were estimated using in the same technique as in Figure 4-7.

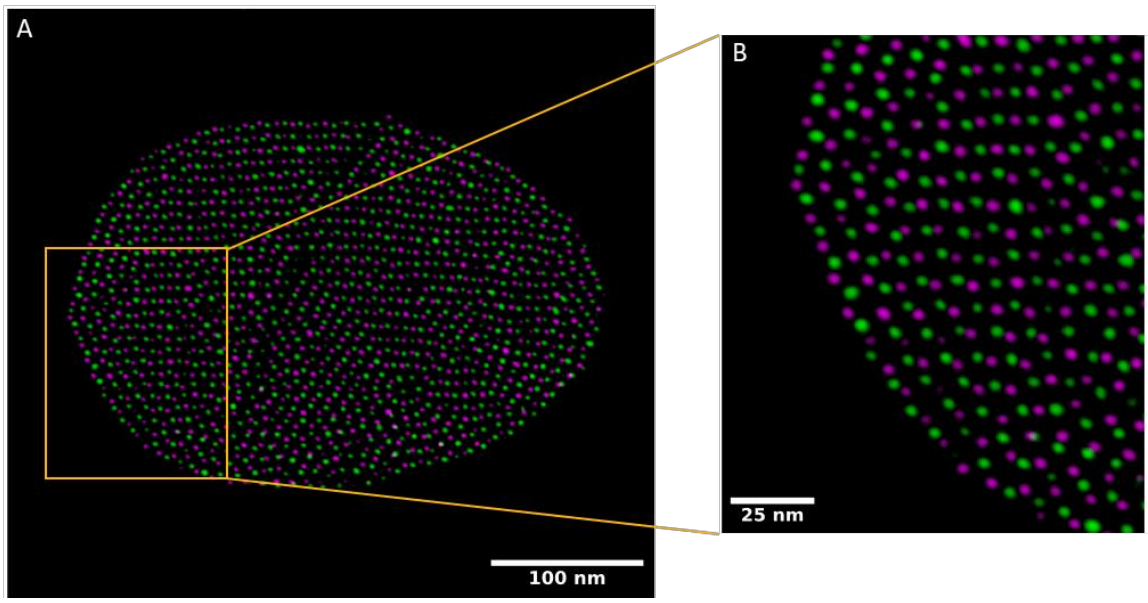

Figure 4-18 a) shows the two base plane layers, demonstrating a distorted hexagonal lattice b) shows a zoomed in view of the lattice within the yellow rectangle.

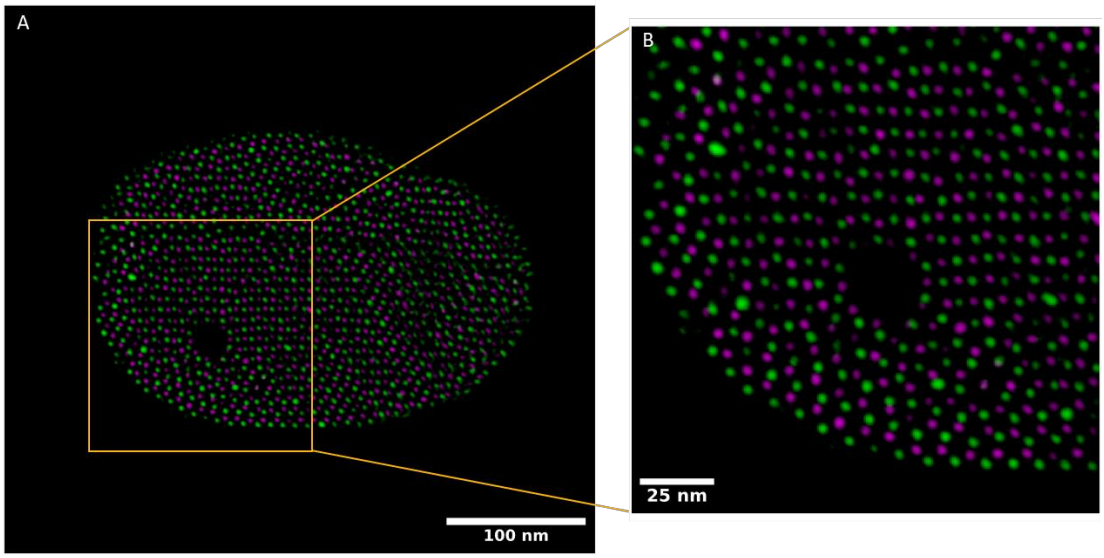

Figure 4-19 a) shows two plane layers near the top. The zoomed in cut (b) shows that near the edge of the NP crystal, especially in the top planes, an HCP/FCC (hollow site) stacking can be observed.

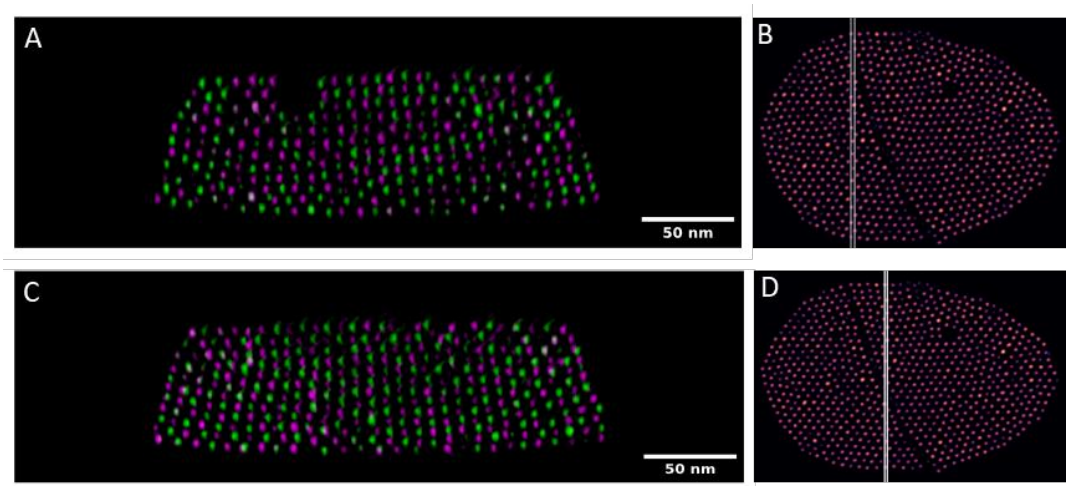

Figure 4-20 Slices of the side view of the 4.0nm (3.8k) Au PGNP (A,B) and the correspondent vertical cuts inset (C, D).

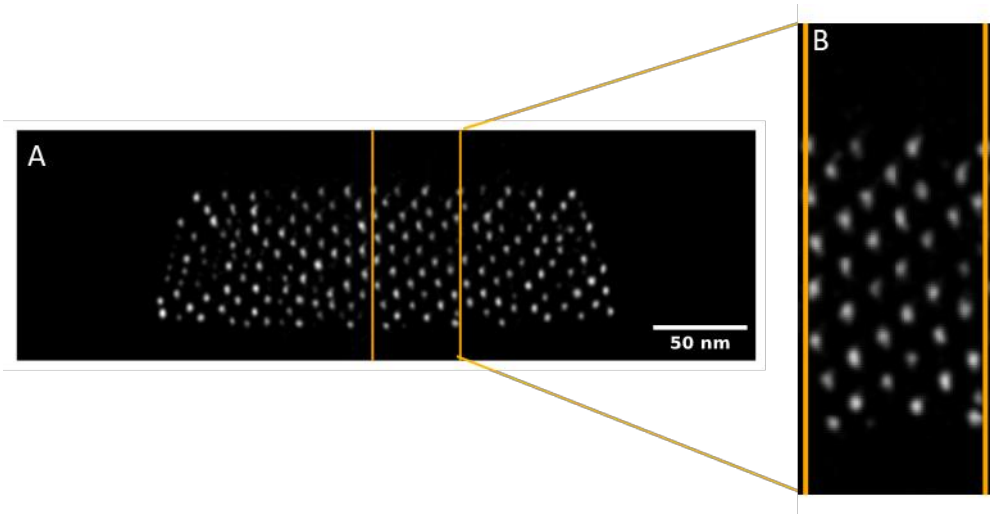

Figure 4-21 . A) 4.0nm (3.8k) Au PGNP single layer showing a square lattice arrangement from the BCC(001) and B) a zoomed in section cut.

A similar NN analysis as for the previous superlattice was performed for the 4.0 nm (3.8k) Au nanoparticle. The calculated number of individual nanoparticles in the 4.0nm (3.8k) Au superlattice was 9305 nanoparticles. The surface area and volume of the superlattice were calculated to be $1.91 \cdot 10^5$ nm^2 and $4.9 \cdot 10^6$ nm^3, respectively. This also yielded a density of $\rho = 2 \cdot 10^{-3}$ nanoparticles/nm^3. The resulting surface area to volume ratio (S/V) for this nanoparticle was 0.039 nm^{-1}.

The resulting RDF function and the histograms are shown in Figure 4-22. The first peak in the RDF function is at r = 8.5 nm and the limit for the first NN is at r = 12 nm.

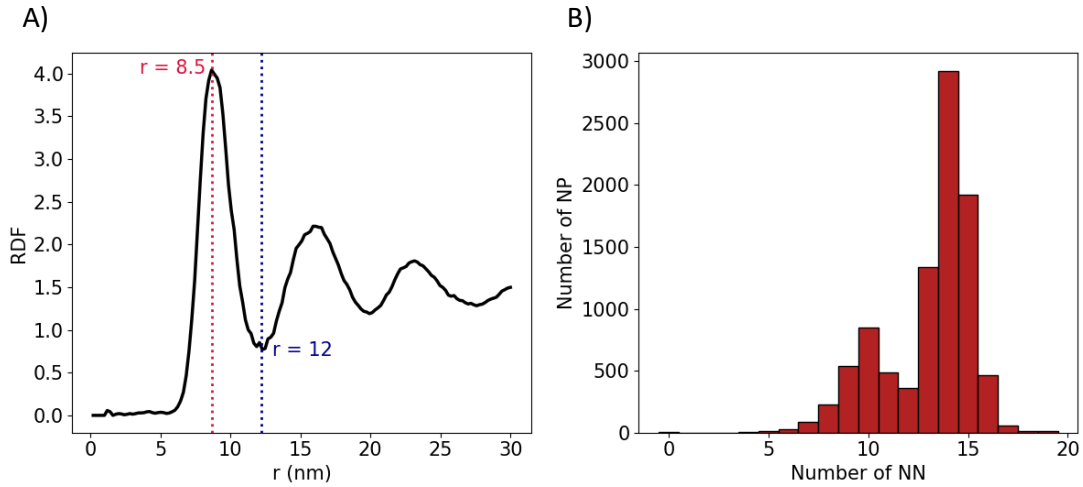

Figure 4-22 a) RDF function showing the average radius of the first NN shell (r = 8.5 nm) and b) the limit of the first NN shell (r = 12 nm).

The histogram in Figure 4-22 shows that within the first shell radius r = 12 nm, the modal number of neighbours is 14. In a BCC structure, the first two shells are close in radius. The first shell has 8 neighbours within $a\sqrt{3}/2$, and the second shell has a further 6 neighbours with radius a, where a is the lattice constant. The peak in the RDF would therefore account for both the first and second NN shells and since these are closely spaced, they could not be resolved in the data. In a BCC structure the distance of the second NN is equal to a, meaning a~8.5 nm for this nanoparticle crystal. Also, a smaller peak at 10 neighbours can be noticed in Figure 4-22. This is due the contribution of the nanoparticles from the outermost layers, which have only around 10 neighbours within the first shell radius. This peak appears in Figure 4-22 because of the relatively higher weight from the contribution of the outermost layers when compared to the previous superlattice – and can be explained by the higher surface area to volume of this nanoparticle, which is around 50% higher than the calculated ratio for the superlattice presented in the last section.

The projections of the histograms, within the radius r = 12 nm are shown in Figure 4-23, a. When comparing the projections from a simulated BCC lattice (Figure 4-23, b), the

directions observed match to the directions $[111]$, $[1\bar{1}0]$ and $[11\bar{2}]$, confirming that the Au superlattice has a BCC structure.

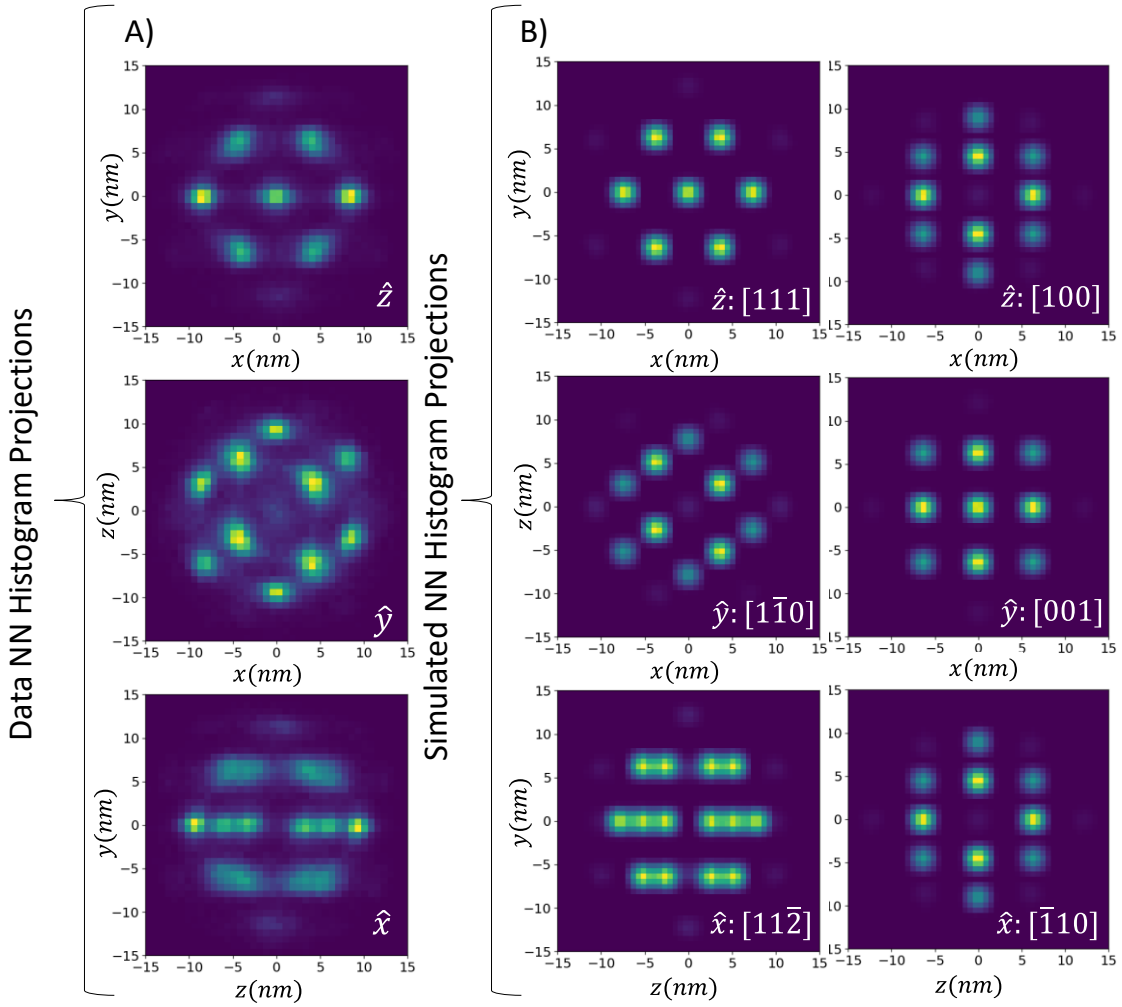

Figure 4-23 Histogram projections of the NN for a shell with radius r = 12 nm. a) from original data b) simulated data for a BCC lattice at the directions indicated (right lower corner). The $[111]$, $[1\bar{1}0]$ and $[11\bar{2}]$ projections match the experimental data in a).

As explained in the introductory section, in polymerized nanoparticles BCC structures can be formed when the soft parameter λ_s, which is the ratio between the extended ligand length and the core radius, is above 0.7. Polystyrene is constituted from styrene monomers with chemical formula $(CHC_6H_5CH_2)_n$ which has an atomic mass of 104 amu. Therefore, the degree

of polymerization[79] of this nanoparticle is n_p~36. The stretched length of these polystyrene nanoparticles can be calculated as[149,154,168]:

$$L_{lig} = 0.128 \cdot 2n_p + 0.2 \tag{4.2}$$

Resulting in a stretched length of L_{lig} = 9.4 nm. This results in a soft parameter of λ_s= 4.7. Therefore, this result explains the observed BCC structures.

The soft parameter for the first nanoparticle was also calculated for comparison. The 4.0nm (PS = 1.3k) Au nanoparticles had a degree of polymerization of n_p~ 12 that resulted in L_{lig} = 3.3 nm and λ_s = 1.65. Thus, although this soft parameter value also predicts the formation of BCC structures, the lattice of these nanoparticles was assembled as a RHCP structure instead, as it was shown in the last section. The data presented in this chapter does agree with the trend towards FCC structures with decreasing λ_s. This result could be an effect from the grafting densities Σ of these nanoparticles, i.e. the number of bound polymers per surface area (chains/nm^2), since Σ determines the effective diameter of the nanoparticle[154] (as mentioned in Section 4.1), and previous results have reported an increase in λ_s to higher effective values as a function of the grafting density[154].

Therefore, to understand the formation of the lattice structures in these nanoparticles, a continuation of this work would involve the synthesis of these nanoparticles with different values of Σ. The measurement of Σ and the resulting lattice parameters would complement this investigation of the formation of the lattice structures in these nanoparticles.

4.4 Conclusion

This chapter has studied the lattice structures of self-assemblies composed of polystyrene-coated Au nanoparticles. The addition of PP in the solution generated the formation of 3D self-assemblies that were investigated through their electron tomography.

The 3D reconstruction and analysis of two different nanoparticles were presented where their cores sizes had approximately 4.0 nm, but different molecular weights 1.3k g/mol and 3.8k g/mol, respectively. Both structures had in-plane hexagonal symmetries, and more nanoparticles in their bottom layers than the top, indicating that the growth starts from the substrate.

The identification of the individual positions of the nanoparticles allowed the determination of their stacking arrangement. It also allowed the determination of the nearest neighbourhood of these nanoparticles and therefore the interparticle distance in their crystal arrangement.

The Au nanoparticles with M_n = 1.3k g/mol, had formed superlattices which showed competition between FCC and HCP stacking, resulting in a RHCP structure. As mentioned earlier, this is an expected observation since previous reports show that hard spherical nanoparticles normally assemble into one of these structures – and since both FCC and HCP have similar levels of free energy, variations on the temperature can trigger transitions from one arrangement to the other. In the second superlattice (M_n = 3.8k g/mol), the nanoparticle behaved as “soft spheres”, and their lattice assembly is in good agreement with a non-close packed BCC structure.

The structural analysis and quantification from the electron tomography datasets contribute providing initial insight for the tuning of packing symmetries, which has applications in electronic and magnetic fields[140].

5 Electron tomography of gold bipyramidal nanoparticles

In this chapter chemically synthesized bipyramidal gold nanoparticles are studied through electron tomography and their morphologies are investigated for potential chirality.

The structure of this chapter is as follows: section 5.1 presents the motivation for these experiments and previous research related to this work. Section 5.2 explains how the experiments and the reconstruction of the tomography datasets were performed. Section 5.3 presents the main results obtained from the STEM electron tomography and details of the geometries of the Au bipyramids. Finally, section 5.4 discusses the conclusions of these experiments and future work.

5.1 Au bipyramidal nanoparticles

In recent years a lot of research has been carried out into engineering nanoparticles with controlled shapes using different mixtures of surfactants. There is a special interest in development of controlled and optimized synthesis of anisotropic nanoparticles (i.e. with non-spherical shapes) due to their applications in several research areas. In the field of optics for example, the optical properties of nanoparticles are dependent on their shape[169] - the axis of interaction with the light, and the aspect ratio of the nanoparticle (length/diameter ratio)[170]. Anisotropic nanoparticles also have applications in the electronic and medical fields, since these areas have a strong desire to engineer the shapes of nanoparticles in order to efficiently control activities such as sensing[171,172] and drug delivery[173,174].

Seed-mediated processes are the most common methods used to control anisotropic shape synthesis of nanoparticles. Growth is initiated from spherical seeds[175,176], leading to

morphologies from nanorods[177] to more complex shapes such as bipyramids[170,178,179], nanoflowers[180,181], and nanodendrites[182,183].

In particular, the seed-mediated synthesis of Au nanoparticles can lead to a broad variety of anisotropic shapes and symmetries, where the initial seed structure has an important role in the resulting shapes[184]. Normally, multiply-twinned seeds lead to the production of nanorods and bipyramids, and the overall growth process consists of two consecutive reactions. The first reaction consists of the production of the gold seeds by the reduction of a gold precursor (e.g. $HAuCl_4$) using a reducing agent (e.g. $NaBH_4$) in a surfactant solution such as cetyltrimethylammonium bromide (CTAB) for example. At this stage, citrates may also be added to cap and stabilize the nanoparticles[185]. The resulting seeds typically have sizes that vary in the a range of 3-5 nm[185] and the final anisotropic shapes highly dependent on the seed structures.

The second reaction is performed to grow the anisotropic structures. Here, silver nitrate is added since it assists the growth of the seeds and affects the aspect ratio of the final geometries[170]. In fact, the presence of Ag ions in many studies is believed to be the reason for the formation of high index planes, resulting in more complex and interesting morphologies[184,186]. In this step, a mild reducing agent, such as ascorbic acid (vitamin C) is used to assist the growth[187].

Depending on the synthesis conditions, the nanorod obtained from seed-mediated methods are often either single crystals with growth axis aligned in the [001] direction[188] or penta-twinned folded nanorods with isometric five-fold twinned symmetry around their axis[189]. The rod-like shapes are often used for optical studies, where the interactions of the nanoparticle with the emitted frequency can be tuned by the ratio aspect of the nanorod[190].

Regarding the bipyramidal shapes, there have been several reports of a variety of morphologies. Lee at al., for example, achieved good control in the production of monodisperse

gold bipyramids with different geometries, by tuning the regrowth of the bipyramids in single and binary surfactants[178]. A majority of research reports on nanoparticles with bipyramidal shapes described by a penta-twinned symmetry - although some studies have observed hexagonal structures, instead[191]. There is a particular interest in bipyramidal nanoparticle shapes due to an increased plasmon response at their apices and which has potential applications in imaging and bio sensing[192].

Although in general these methods result in a good control of the nanoparticles shape, the role of each reactant in these two reactions are not very well understood[193]. Therefore, the use of tomography experiments to precisely characterize the shapes of these nanoparticles in three dimensions is an important ally to support future development of computational simulations to predict nanoparticle shapes.

5.2 Sample characterization and electron tomography

In this work the morphology of Au bipyramid nanoparticles was studied through STEM electron tomography. The Au nanoparticles were prepared by Assaf Ben-Moshe from Alivisatos Group at the Chemistry and Materials Science department, University of Berkeley. The synthesis of the Au bipyramids was performed with a seed-mediated process, and the reactions have a composition similar to previous work published in order to study the plasmonic properties of these nanoparticles[194], consisting of the growth of 3 nm gold nanoparticles used as seeds. CTAB was used to stabilize the nanoparticles, and NaB_4H_4 was used as a strong reducing agent. However, the growth of the seed was performed using hydroquinone ($C_6H_6O_2$) as a mild reducing component, instead of the commonly used ascorbic acid, as mentioned previously. The final reaction mixture was drop cast onto amorphous carbon film TEM grids

for imaging in the electron microscope. The solvent atop the grid was allowed to dry under ambient conditions before imaging.

TEM images were acquired from a FEI ThemIS S(TEM) microscope, operated at 300 kV with a Ceta2 CMOS camera. Figure 5-1 shows a TEM image from an Au bipyramid, where a diffraction contrast line can be observed along the growth axis of the nanoparticle, indicating that these structures are not single crystalline. Instead, the diffraction line evidences a boundary twinning separating two different planes. The 2D-FFT of two regions, from opposite sides of the diffraction line (Figure 5-1) revealed interplanar distances of 2.36 Å and 2.05 Å. Since gold has a FCC lattice arrangement, with a lattice constant of 4.072 Å[195], these planes correspond to the {111} and {002} planes, respectively.

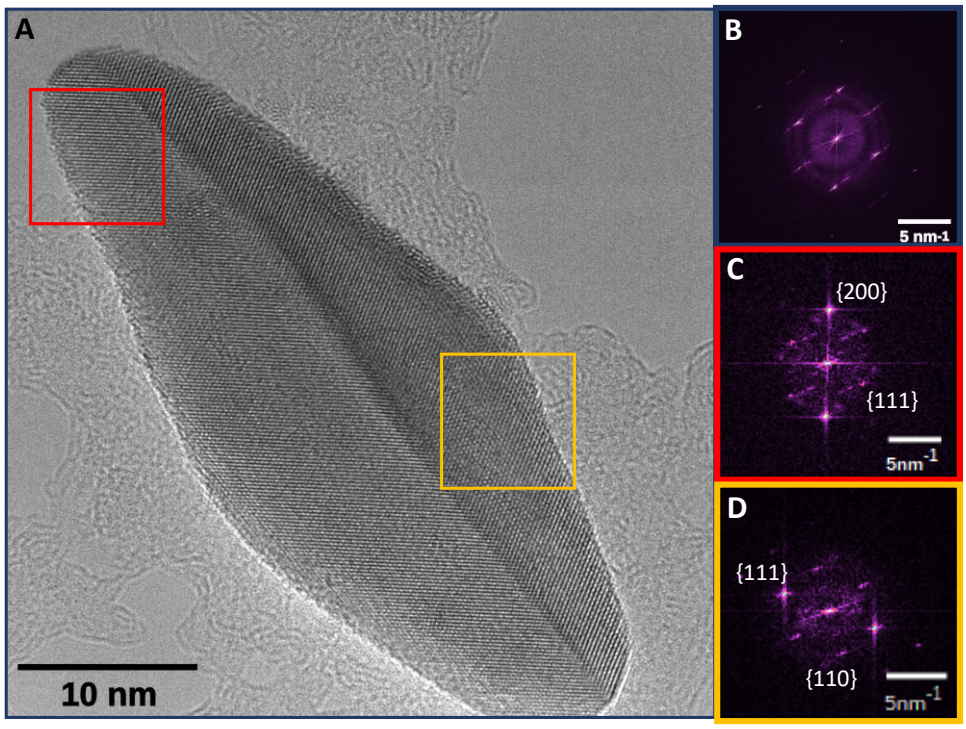

Figure 5-1 TEM image from an Au bipyramid showing a twinning boundary. b) shows the 2D FFT from the whole image. c) and d) are the 2D FFT's of the cropped regions (indicated by the outliner colours).

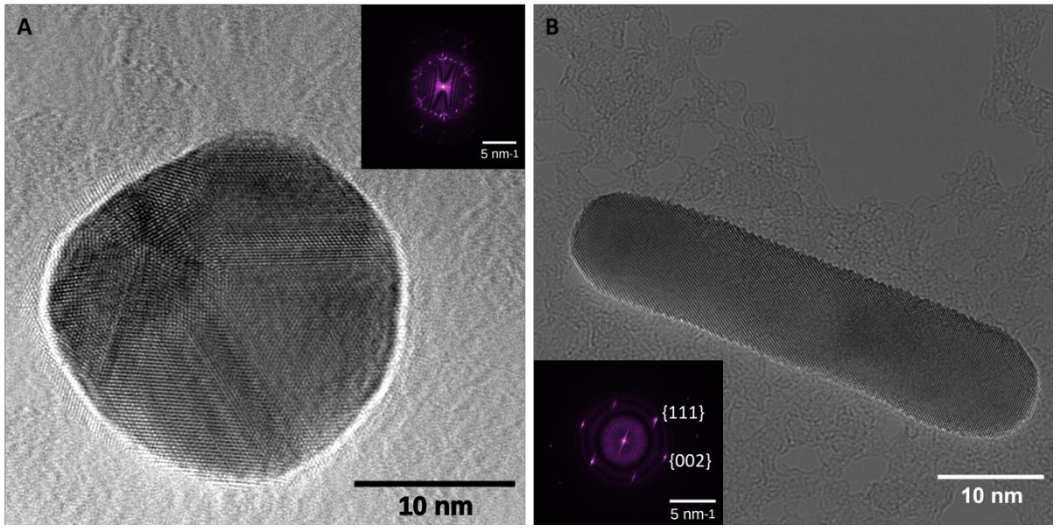

Figure 5-2 TEM images showing the different AuNP morphologies resulted from the seed-mediated synthesis. a) shows a multiply-twinned spherical shape, slightly defocused to enhance contrast. (the quality of this image is slightly compromised by astigmatism.) b) TEM image and FFT of a single crystalline nanorod, oriented in the [110] zone axis.

The reaction also resulted in spherical multiple-twinned nanoparticles (Figure 5-2, a), with diameters of 15 nm. Nanorods were also observed oriented in the [110] zone axis direction, and with single crystalline structure, i.e. with no observable twin boundaries or any stacking faults (Figure 5-2, b). Beyond the rod shapes, dog bones[187,196] geometries were also found as shown in Figure 5-3.

To prepare the samples for electron tomography, the solution with the Au bipyramids were drop cast onto a hexagonal 100 mesh grid coated with an ultrathin carbon layer (3-4 nm). The grid structure had a lower number of mesh units and therefore increased grid square side lengths. This improved the tilt range of the tomography, resulting in two tomography datasets acquired from -75° to 75° and from -78° to 70°, respectively. An ultrathin carbon layer was used to improve image quality by reducing beam attenuation through the layer.

The drop cast solution containing Au bipyramids was allowed to dry, before a stock solution containing 5nm Au fiducial markers was also drop cast on the grid. The samples were checked in the STEM microscope prior to the electron tomography acquisition. Contamination

buildup under the electron beam during scanning required that the sample needed to be plasma cleaned. For these samples, 30 seconds of Ar/O_2 (5%) plasma treatment was enough to remove the contamination to levels that did not interfere in the acquisition of the tomographic dataset and did not cause observable sample damage. Both tomography datasets were acquired using a FEI Titan operated at 300 kV, with a semi-convergence angle of α_c = 10 mrad and a collection angle of β_c = 68 mrad. The 1024 × 1024 images were acquired with typical dwell times of 16 μs. Figure 5-3 shows one of the ADF-STEM images from the first tomography dataset, taken at 0°, sample tilt, showing both the bipyramids of interest and the fiducial markers used for the electron tomography - as well as a variety of nanoparticle shapes found on the grid, as discussed previously. The Au nanoparticles had bipyramidal or spherical shapes, in higher proportions, but nanorods and dog bones shapes were also observed in smaller quantities. In this sample, from 92 nanoparticles observed in the STEM images, 60% of them had bipyramidal shapes. These bipyramidal nanoparticles had a typical in plane length of 72 ± 7 nm and maximum width of 24 ± 2 nm, corresponding to an aspect ratio of ~ 3.

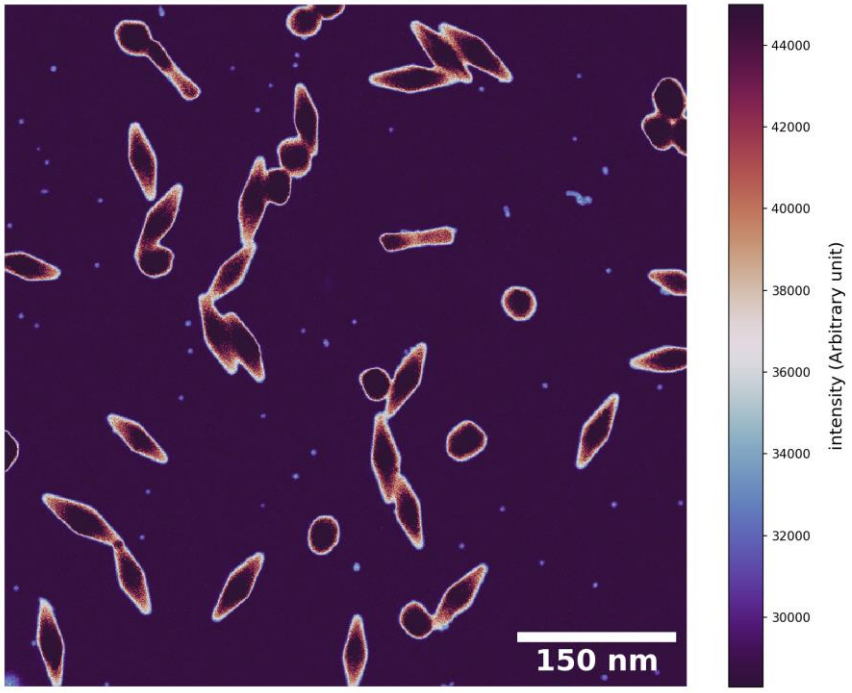

Figure 5-3 ADF-STEM projection (α = 0°) from the first tomography dataset, showing different nanoparticle shapes (bipyramids, spheres and dog bones) obtained from the Au seed-mediated synthesis, as well as and the fiducial markers used for the fine alignment.

This first tomography data was acquired with a magnification of 80 kx, resulting in projections with a pixel size of 0.91 nm and with an electron beam dose of 2.5×10^3 $e^- nm^{-2}$ $frame^{-1}$. With this resolution the overall shape of the Au bipyramid could be identified; however, the geometrical details of the facets could not be well resolved, as will be discussed in the next section.

During the STEM tomography acquisition of these samples, there was a trade-off between increased magnification and resolution with contamination growth. As discussed in previous chapters, the build-up of hydrocarbons on the sample under the electron beam will affect the measured intensities in the image projections and this will critically affect quality of the reconstructed volume. Therefore, in order to improve the information about the geometrical details of the Au bipyramids, a second sample was prepared from a new synthesis, where the growth step was prolonged, in order to obtain bigger Au nanoparticles.

The resulting nanoparticles had an in-plane length of 133 ± 8 nm, and maximum width of 33 ± 2 nm, corresponding to an aspect ratio of ~ 4. This second dataset was taken with a higher magnification 160 kx, corresponding to a pixel size of 0.46 nm – and with an electron beam dose of 9.9×10^3 $e^- nm^{-2}$ $frame^{-1}$. This sample did not exhibit significant contamination buildup during the experiment. One of the ADF-STEM projections for this second tomography dataset, taken at 0˚ sample, is presented in Figure 5-4.

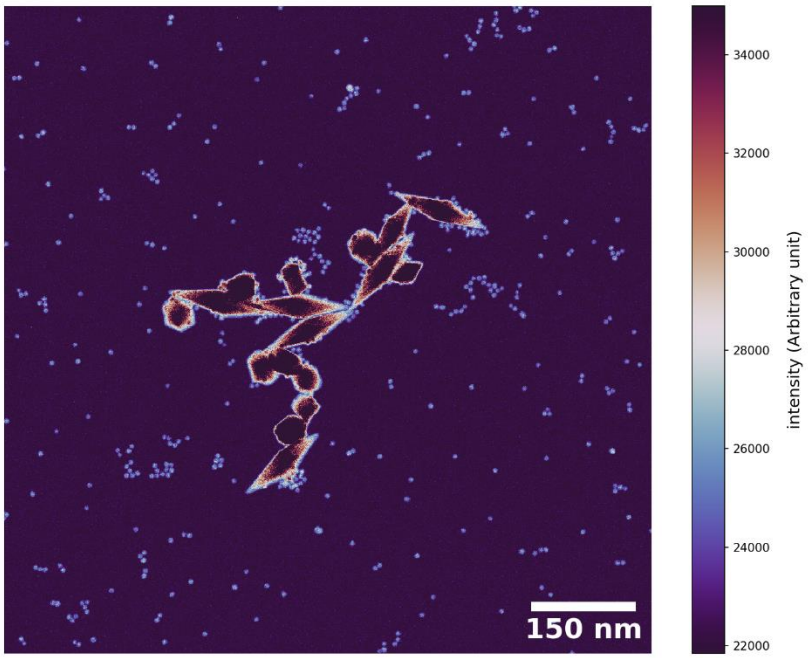

Figure 5-4 Colormap image of one of the ADF- STEM projections, taken at α = 0°, for the second tomography data acquired for Au NP with an aspect ratio of 4 and pixel size of 0.46 nm.

The alignment and reconstruction of both electron tomography series was performed using IMOD. Coarse and fine alignment were achieved, using cross-correlation and by the fiducial markers, respectively. Reconstructions were performed using the filtered back-projection method.

5.3 Results

The rendered view of a region of interest reconstructed from the first tomography dataset is shown in Figure 5-5. The Au bipyramids exhibit a complex shape, with truncated apices and curvy edges. These features were smoothed out because, as mentioned in the previous section, the nanoparticles had small sizes and the image projections had a pixel size of 0.91 nm. Thus, the question was whether the corners were actually twisting, as was believed to be the case in the work published by Navarro et. al., where they performed TEM tomography[194]; or if the resolution of this dataset was not high enough to capture the fine details and angles of the facets, giving a false perception of twisting at lower magnification.

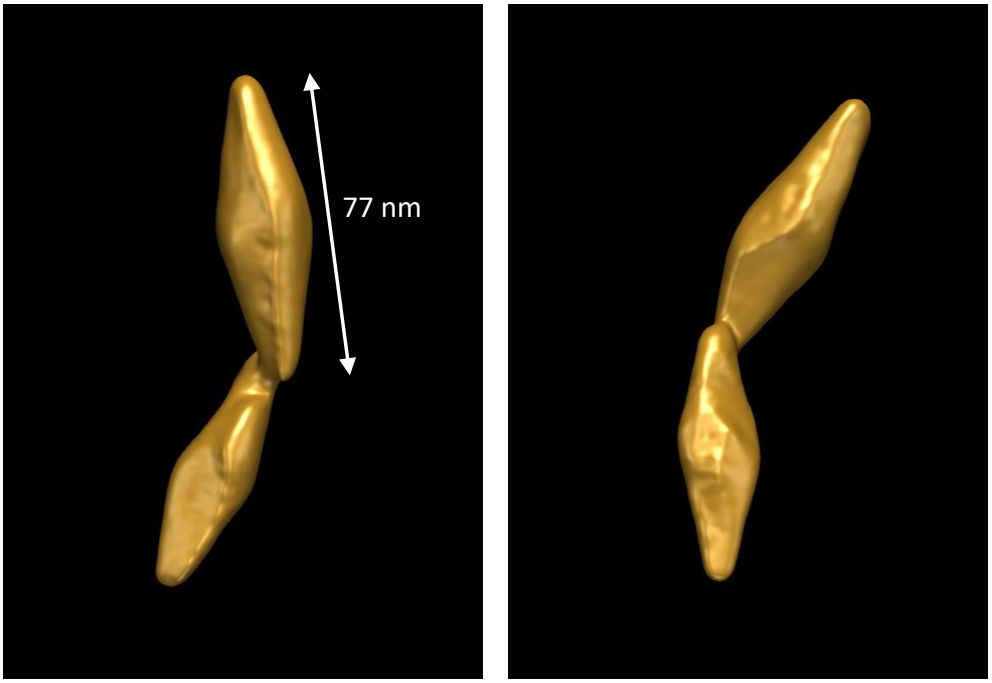

Figure 5-5 Rendered views of the reconstructed volume from the first electron tomography of Au nanoparticles.

Therefore, the second electron tomography dataset, with bigger nanoparticle sizes and lower pixel size (0.46 nm) allowed for the resolution of edges and facets from the Au bipyramids through their cross-sections as will be discussed later. The fine details in the

volumetric data could not be easily assigned though due to two reasons. Firstly, the tomography series had intrinsic imperfections from reconstruction artefacts, similar to the other datasets presented in the previous chapters. Secondly, on the top of these drawbacks, the Au bipyramid nanoparticles were always part of agglomerated clusters on the samples, as can be seen in Figure 5-4. These agglomerates were composed not only by other nanoparticles grown from the seed-mediated synthesis, but also from the Au fiducial markers.

The cross-section slices from this second tomography data series revealed that the geometry of the bipyramids maintain a five-fold symmetry along the growth axis of the Au bipyramids, as shown in Figure 5-6.

However, despite what has been reported in the literature (as presented in the section 5.1), the shape of these slices are non-regular pentagons. They can be interpreted as the resulting shapes cut from regular pentagons which result in a geometry that resembles a "house" shape, as outlined in Figure 5-7. Geometrically, these irregular pentagonal cross-sections can be constructed with asymmetrical radial axes, i.e. a short and long axis with lengths r_s and r respectively in Figure 5-7 - instead of equal axes r, which construct a regular pentagon.

Another characteristic observed in Figure 5-6 and along the bipyramidal slices, is that the orientation of the sharpest pentagon vertex , i.e. the vertex bound by short axes either side, shifts between the top and bottom halves of each nanoparticle. Cross-sections taken along the top half of an Au bipyramid, show that the sharp vertex is oriented towards the lower right of each image, whereas the sharp vertex in the bottom half of the bipyramid is oriented towards the right of each image. This feature was observed in all of the Au bipyramid nanoparticles present in the tomography dataset. Another characteristic of the morphologies of these bipyramids is that cross-sections in the central region are irregular with more than five edges indicating a transitional geometry between the top and bottom half of the bipyramid.

Figure 5-8 shows the angles calculated for a few cross-sections along the Au bipyramids. A mask of the nanoparticle cross-section was constructed through image thresholding and the dominant edges were determined using Hough line detection using the skimage package. The intersection of the lines extrapolated from the detected edges were then fit to a polygon, which is the resulting feature shown in Figure 5-8. The angle between the sharp vertices in the top and bottom half in the bipyramids was calculated to be $\Delta \approx 70°$. This is approximately not only the internal angle of a regular pentagon, but also the internal angle of the model presented in Figure 5-7. This result indicates that the location of the vertices in the top and bottom half of the bipyramids do not shift significantly, and that the observed irregularity is due to elongated facets in certain direction, as it depicted in Figure 5-9.

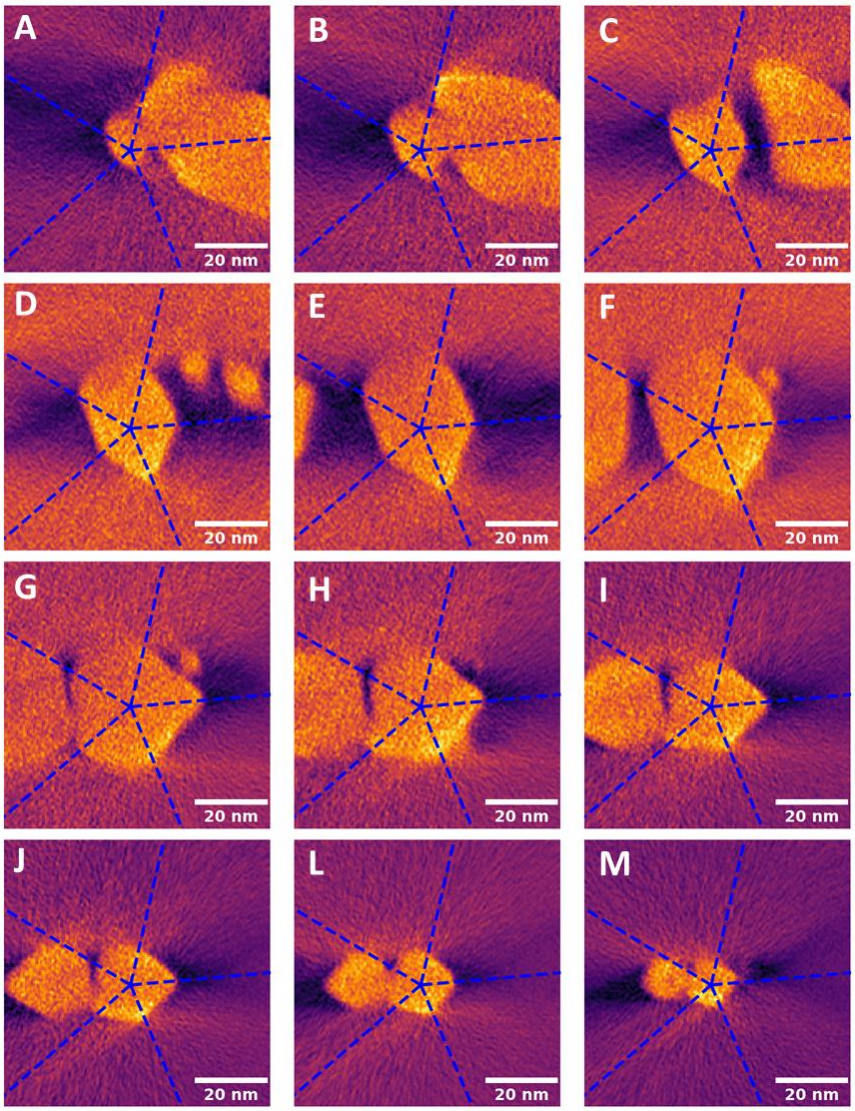

Figure 5-6 Cross-sectional cuts from the reconstructed electron tomography of the Au bipyramids. All slices show a five-fold symmetry. The blue-dashed lines show the axes of a pentagon which is unchanged between slices and lies on the central axis of the nanoparticle. The (x, y) vertices of this pentagon are described by $(x, y) = (rcos(\theta_{off} + n\,2\pi/5), rsin(\theta_{off} + n\,2\pi/5))$, where $n = 0,\ldots,5$, r is the distance between each vertex and the center of the pentagon, and θ_{off} is an angular offset.

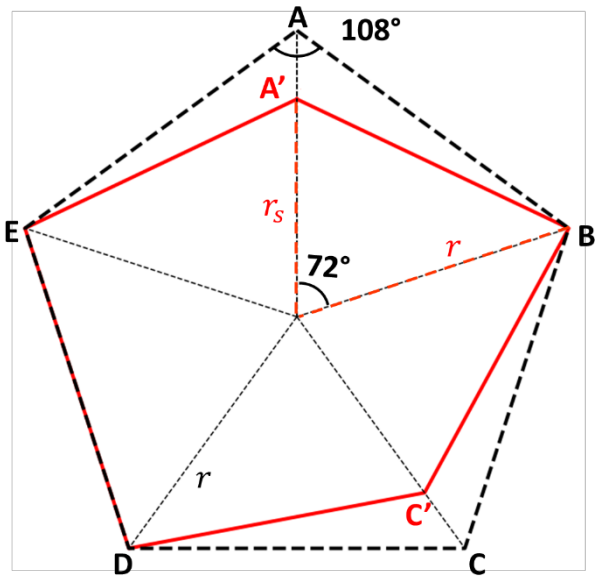

Figure 5-7 Scheme showing the cross section of the Au bipyramids (red line) compared to a regular pentagonal polygon (black dashed line) commonly reported in the literature. Each cross section has the shape of an irregular pentagon ($A'BC'DE$) with the short and long axes labelled as r_s and r, respectively. The regular pentagon ($ABCDE$) has axis given by r, that coincides with the long axis of the irregular shape.

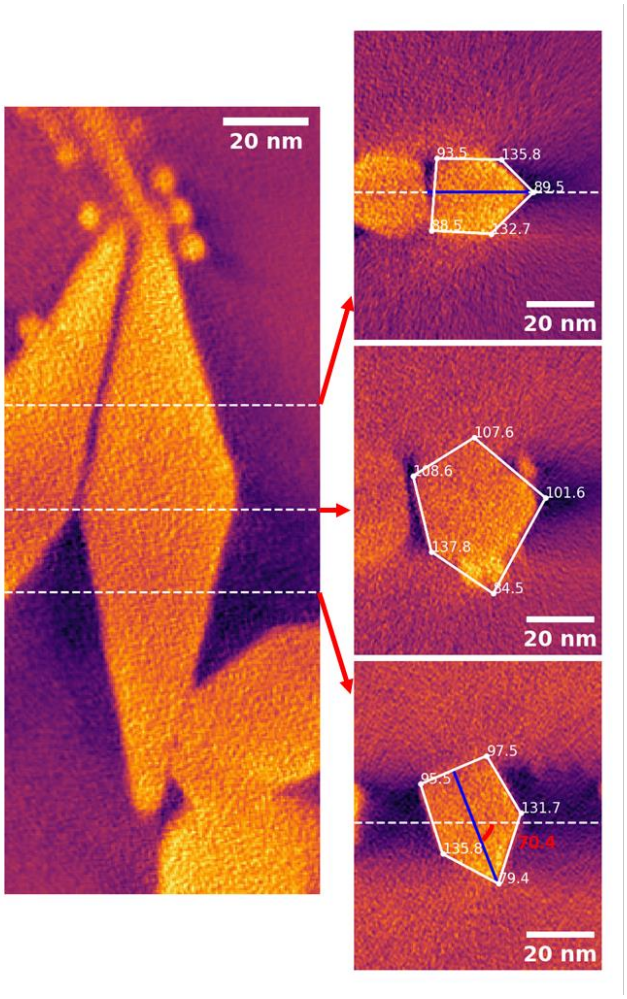

Figure 5-8 Cuts along the Au bipyramid (A) showing that the sharpest edge has a rotation of 70° from slice B) to D.

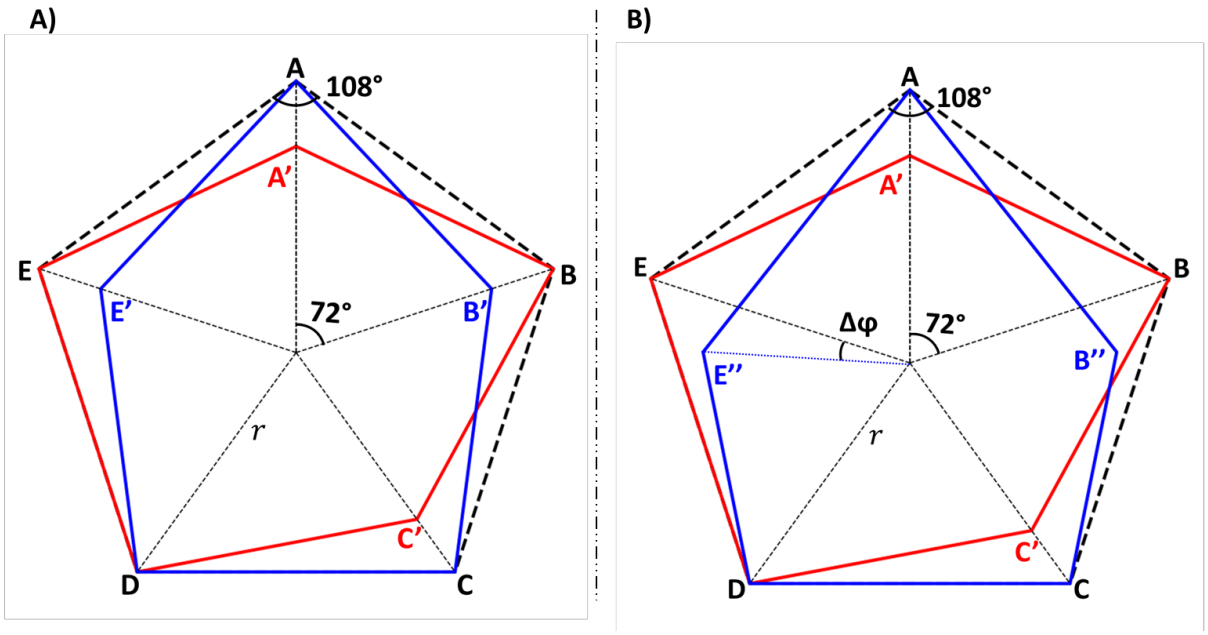

Figure 5-9 A) A scheme showing the case where two of these irregular pentagons have their sharpest vertices rotated by 72˚, to model the experimental data B) Additionally, in order to account for all the geometric details detected in the reconstructed slices, the model of the cross sections need to include the angular deviations (Δφ) in the vertex orientations.

As mentioned previously, the observed agglomeration of the nanoparticles on substrate made the visualization of rendered volume and identification of the individual nanoparticle features difficult. Therefore, in order to better understand and determine the geometry of these nanoparticles, two models were built from the information obtained from the cross sections of the 3D reconstructed Au nanoparticle volumes.

The first model, labelled as “reference model”, was built from two ideal and non-regular bases, rotated with relation to each other, by 72° as the scheme presented in Figure 5-9. Also as shown in Figure 5-9, two cases were built: the first one has no deviations in the directions of the vertices, whereas the second has an angular deviation of $\Delta\varphi = 15^{\circ}$. The effect of introducing angular deviations in the vertices can be observed in Figure 5-10. Basically, it produces irregularities in the facets – and instead of having 3 sides as in the case that $\Delta\varphi = 0$,

they become tetragonal. This small adjustment also induces an S-shape observed along each affected edge in the final model.

This model was made in order to obtain the closest ideal shape – thus setting a reference to the experimental Au shapes. The two simulated results from the reference model are shown in the left side of Figure 5-12.

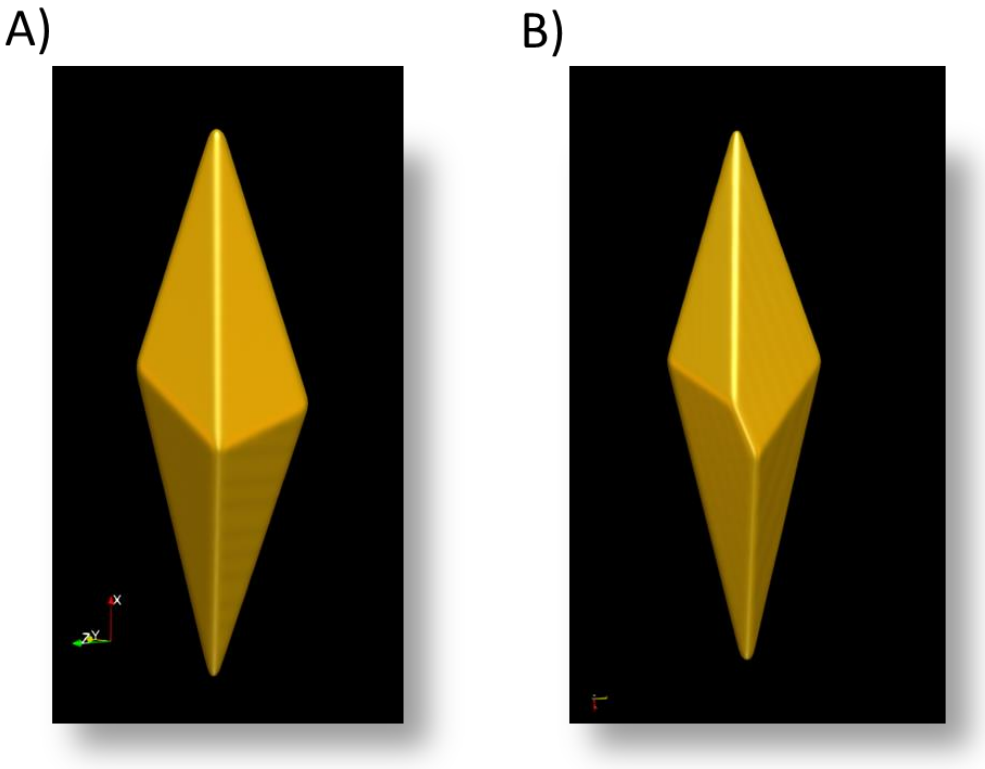

Figure 5-10 The effect of introducing angular deviations in the vertices of the pentagon bases for bipyramids built from the reference model. A) $\Delta\varphi = 0^{\circ}$ and B) a deviaton of $\Delta\varphi = 15^{\circ}$ is introduced in the vertices indicated in Figure 5-9.

The second model, labelled as “experimental model”, was constructed by cutting a cubic volume with the same angles given by the Au bipyramids, and with the intention of obtaining an approximation of the nanoparticle geometry, but free from the artefacts previously mentioned. To build this model, two cross sections, one from the top half and one from the bottom, were chosen along the bipyramid in locations where the shape was well defined (Figure

5-11, a). "Well defined" here means that these slices were not close to the middle of the nanoparticle since the cross-sections in this region were transitional. In each of these slices, lines were manually fitted to each of the 5 edges, as illustrated in Figure 5-11 (b). The planes formed by each facet in the bipyramids were defined by two points (A and B) on the cross-section edges and the corresponding closest bipyramid apex point (C). The normal of each facet is given by the cross product between two vectors situated along the plane, in this case the segments $\overline{AC}$ and the segments $\overline{BC}$ were chosen, and are labelled as $\overrightarrow{v1}$ and $\overrightarrow{v2}$ in Figure 5-11 (c), respectively. Therefore, cuts along these normal directions are made in the initial volumetric cube (Figure 5-11, d), where the dot product of the coordinates in the original volume with the facet normal defines the cutting plane. This process is repeated for each facet, on both the top and bottom cross-sections to create a final model volume. Thus, this model resembles a sculptor cutting a bipyramid from a block of stone and the final morphology is revealed after the final cut. Each reconstructed nanoparticle can have its custom model that emulates its morphology. Although this model gives a good and consistent approximation to the shapes of the nanoparticles, it is subject to errors at the facets boundaries if they are not well defined, since the original cross-section fitting inherently contains viewer errors. These errors, however, were mediated by double checking with other group members.

Figure 5-12 shows the comparison between the ideal reference model and the custom experimental model, where the experimental model was implemented for two different Au nanoparticles.

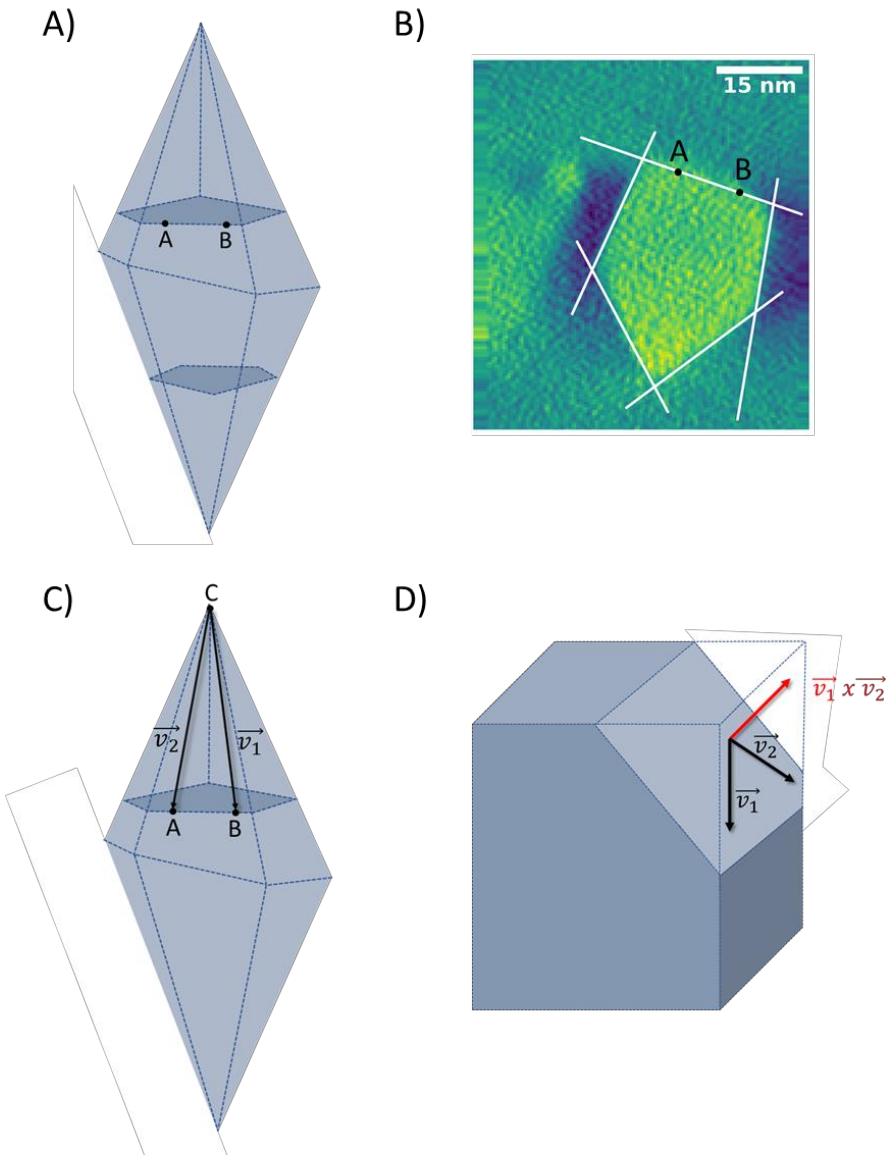

Figure 5-11 Illustrations explaining how the experimental model was built to emulate the bipyramids shape from their experimental geometry. A) Two different slices are taken along the bipyramid and for each of them, two points *A* and *B* are selected for each of the 5 edges (in the illustration above, only one edge is displayed) B) Lines that pass through the selected points are fitted for each edge in a given slice. C) The direction of a facet is the same as the plane formed by the two points (*A* and *B*) and the closest vertex of the bipyramids (*C*). The direction normal to the plane is determined by taking two vectors along this plane ($\overrightarrow{v1}$ and $\overrightarrow{v2}$, respectively in the figure) and calculating the cross product $\overrightarrow{v1} \times \overrightarrow{v2}$. D) Thus, cuts in a cubic volume are made with the same direction as defined by the facets and a model representing the nanoparticle morphology is created.

The geometry of the nanoparticle generated by the reference model resembles a hexagonal scalenohedron, but since the Au bipyramids have a five-fold symmetry it has one facet less than these polyhedrons. The presence of chiral crystals with a regular scalenohedral (hexagonal) symmetry is well reported[82,197,198]. However, to the knowledge of this author, there is no report of chiral crystals with the same symmetry presented in this work.

The more realistic geometries obtained from the experimental model, were precisely consistent between both nanoparticles that the model was implemented for and revealed a similar geometry to the ideal five-fold structure generated by the reference model, but with irregular and truncated facets. The asymmetry in each facet gives to these Au nanoparticles a chiral morphology, since they are not superimposable with their mirror images.

The actual atomic arrangement and crystallography of the bipyramids remains undefined; however, the created models represent a step forward in describing these bipyramid structures. As mentioned previously, previous work has concluded that Au bipyramids have regular pentagonal cross-sections, however the analysis performed in this chapter shows that this is not the case. The S-shapes observed along the bipyramid edges have been observed previously[194], and a simple model with small (~10 degree) angular deviations from a perfect pentagon along some edges is able to replicate this structure. It should also be noted that the S-shape is non-evident without these angular deviations.

Further work should investigate the origin of these deviations at the atomic and crystallographic level. It is possible that the inherent symmetry in these deviations is related to the twinning observed in the HR-TEM images. There is a certain amount of symmetry in locations of the produced tetragonal facets within the overall structure- these facets are located either side of a partial symmetry line (Figure 5-12, experimental model, second panel from top). Further studies may elucidate whether these represent well-defined crystallographic directions within the nanoparticle and therefore the origin of the feature.

The elongation of certain vertices in the bipyramid creates the observed chirality. A regular pentagonal bipyramid is achiral with five-fold symmetry. These symmetries are broken when the certain vertices are elongated, as described by the reference model, and the overall geometry is not superimposable with its mirror.

Figure 5-13 shows a comparison between the experimental tomography data and its associated model (experimental model). As previously discussed, the rendered model was created by sculpting a volume using planar cuts defined by the facets of the nanoparticle, and therefore the data and model are expected to be in good agreement. Two identifiable orientations from the experimental rendered volume are presented. In panel A) and B) an 'S'-shaped edge is highlighted which is present due to the misorientation between the top and bottom pentagonal pyramids as discussed previously. In panels C) and D) the neighbouring projection, ie. one facet across, has an inverted-'V' shape. These morphologies are predicted by the experimental model panels 2 and 3, which also represent neighbouring facets.

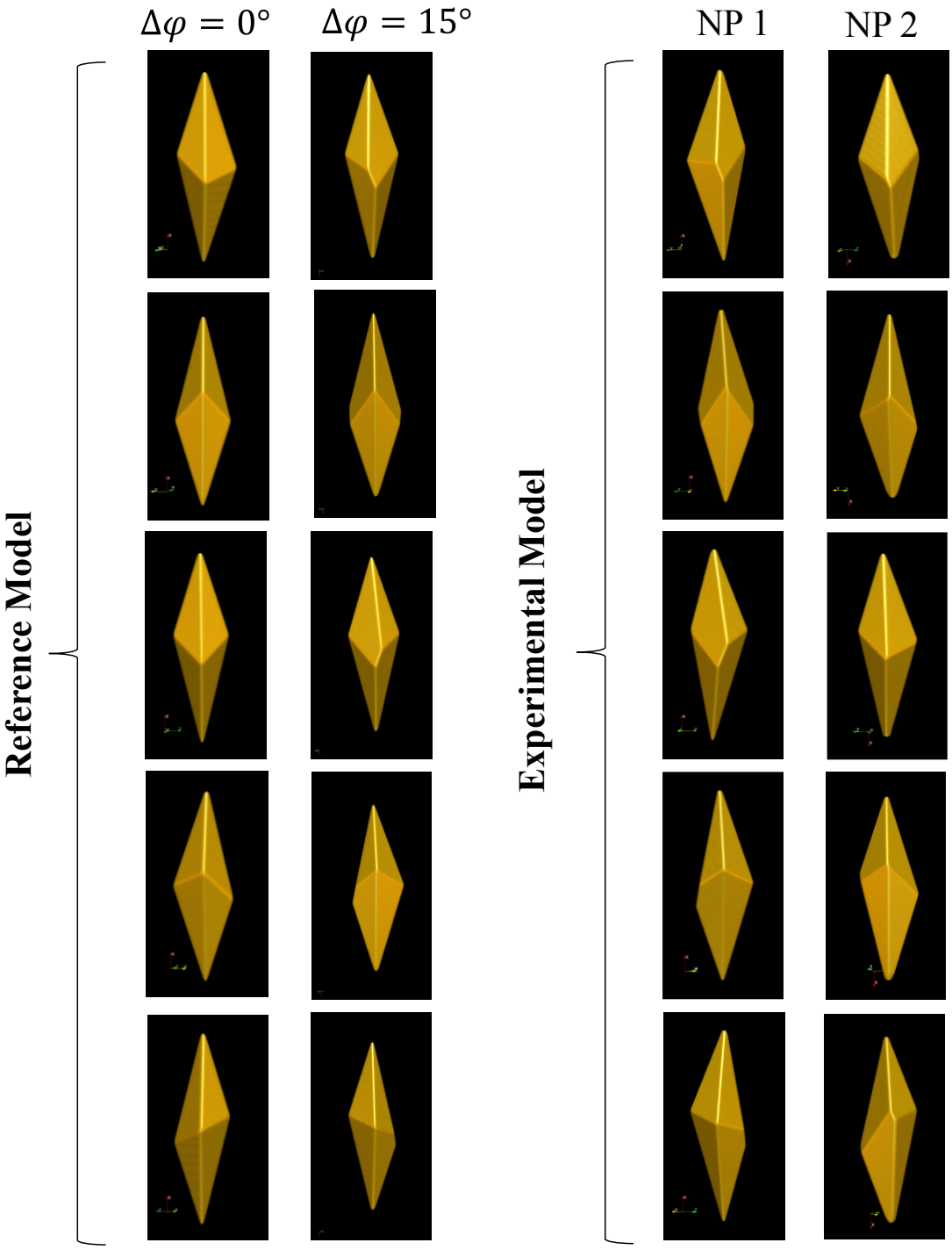

Figure 5-12 Comparison of the facets obtained from the two models built for the investigation of the Au bipyramidal geometries. Left: shows the bipyramid facets obtained with the reference model, made from two ideal "house" shape bases, rotated by 72˚ and with deviations in the vertices of Δφ = 0˚ and Δφ = 15˚, respectively. Right: Two different bipyramids generated from the experimental model, i.e. from their respective cross-sections.

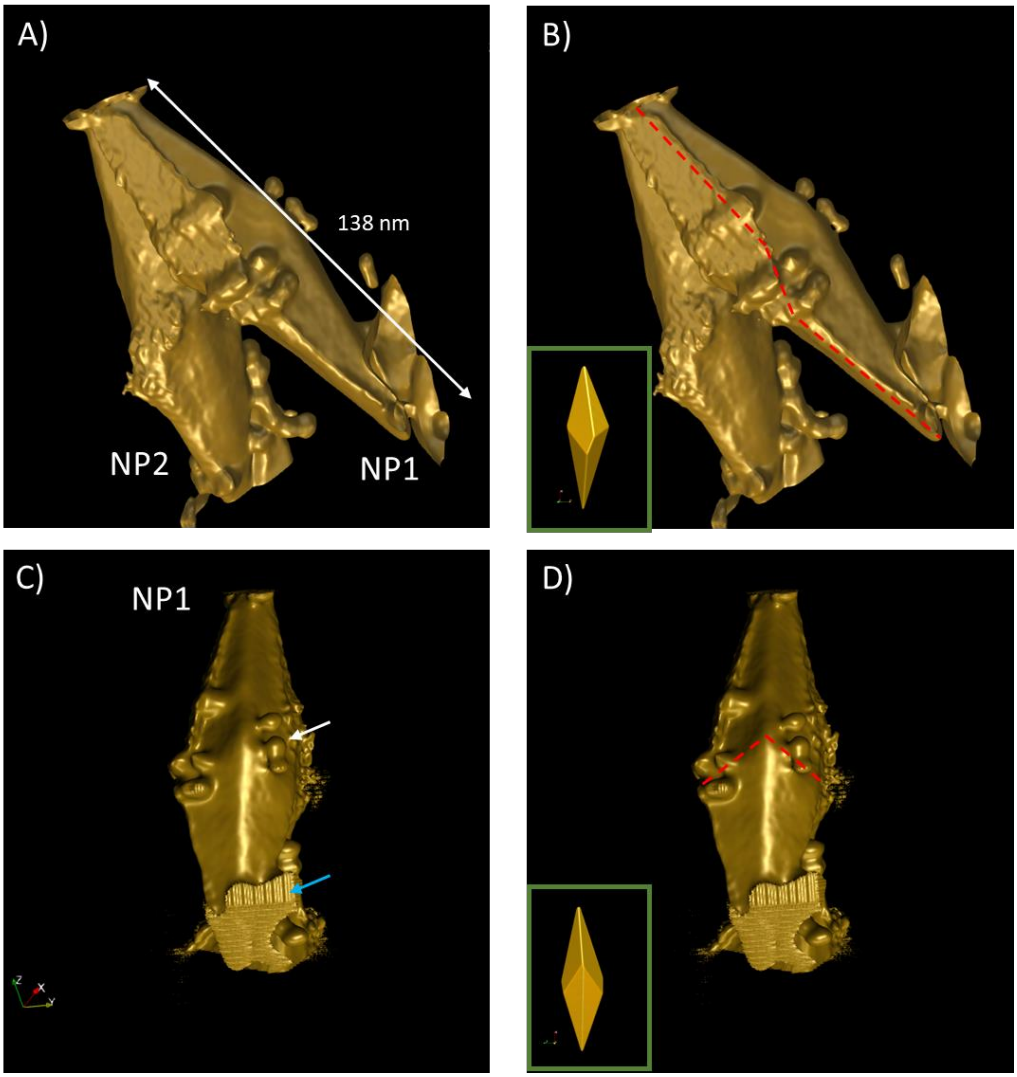

Figure 5-13 Experimental electron tomography data outlining the comparisons between the data and the experimental model, which was constructed from the experimental cross-sections. a) and b) side view highlighting an 'S'-shaped edge formed by neighbouring facets (red dashed line). The inset shows the relevant projection predicted by the experimental model. C) and D) front view with where the inverted 'V' shape has been highlighted (red dashed line) which is predicted by the experimental model (inset). Due to nanoparticle aggregation on the sample, the surface rendering presented here shows artefacts from the fiducial markers (white arrow) and due to cropping of the rendered volume (blue arrow). These artefacts visually obfuscate the nanoparticles however they do not affect the interpretation of the overall morphology of the nanoparticle.

5.4 Conclusion

In this chapter the shapes of anisotropic Au nanocrystals synthesized though a seed-mediated method were studied. Small gold nanoparticles with a diameter of a few nanometers were used as seeds and stabilized by a CTAB layer. The addition of hydroquinone as a reducing agent led to the formation of an unconventional bipyramidal morphology that was investigated through electron microscopy and tomography experiments. The detailed analysis of the rendered volume of Au nanoparticles revealed that their overall morphology is neither regular pentagonal bipyramids nor twisted, as was believed to be the case in previous reports in the literature. Instead, although the facets of these nanoparticles are assembled in pentagonal structures, they are irregular, forming an overall chiral nanoparticle shape. The high number of facets in these bipyramids can have applications in the optical and electronic field, since absorption of radiation becomes increasingly size dependent for anisotropic nanoparticles. Moreover, the presence of chirality in these nanoparticles, even though bulk gold has an FCC, and therefore achiral crystal lattice, has several applications, including use in fields of pharmaceuticals and catalysis. In these fields enantiomers play an important role, where crystalline surfaces often have preference for the adsorption of a determined chiral molecule[82,199]. The sharp apexes observed in the bipyramidal geometries is favourable for tissue penetration applications in the medical field[187].

The main conclusion of this study is that currently the model for growth of bipyramids by simply elongating the five-fold seeds is not complete and too simplistic to explain the morphologies presented here and needs further study.

Future studies would investigate defects and dislocations in the lattice structure of the Au bipyramids to elucidate the details of its growth mechanisms. To this effect 4D-STEM experiments may elucidate changing lattice orientations across the nanoparticle and provide

further evidence of lattice structure. Also, further synthesis work may investigate controlling of the handiness of the chiral nanoparticles, which would allow use in real-world applications.

6 Conclusion and Outlook

This thesis studied the application of scanning transmission electron microscopy towards understanding the 3D morphologies of different nanoparticle systems.

In the first experimental chapter Te chiral nanoparticles were studied and the results would potentially have high impact in the field of chirality. It was shown that chiral nanoparticles can be formed without chiral ligands and the results evidence a growth mechanism mediated by screw dislocations, which has not been suggested previously for this system to our accounts. The 4D-STEM experiment presented a novel type of analysis to extract lattice twisting from the recorded diffraction patterns by considering the changes in misalignment of the ZOLZ across the length of the nanoparticle. Further study of VDF reconstructed data revealed twist band pairs, which are further evidence of lattice twisting and screw dislocations. Importantly the magnitudes of observed twisting calculated from the ZOLZ method and the twist bands were in agreement, highlighting the efficacy of the techniques. Future work on this subject would involve the determination of the handedness of the chiral lattice through 4D-STEM experiments that include the SOLZ or high-resolution STEM[200].

In the second experimental chapter, the study of Au grafted nanoparticles demonstrated a new method of forming 3D superlattices by adding polypropylene to the solvent. Electron tomography and subsequent analysis was able to determine the lattice structure with clarity by looking at lattice stacking order and the nearest neighbour distribution of the constituent nanoparticles. This type of analysis worked for both RHCP (FCC/HCP) and BCC lattices which were prepared with ligands of different molecular weights, and the trends in observed stacking were in agreement with the soft-lattice parameter studied previously. This type of nearest neighbour analysis is general and therefore applicable to many different systems.

Future work would involve the synthesis of this nanoparticles with different polymer grafting densities and the study of their lattice structures to determine whether complete control can be created from the synthesis.

In the final experimental chapter, electron tomography was used to study the structure of Au bipyramids. These nanoparticles have an interesting geometry that has not been precisely reported in the literature to the knowledge of this author. To further understand the tomography results, and study any potential twisting, a model was developed based on the cross-sections of the nanoparticles from which a volume with similar geometry was sculpted. The concept used in the implementation of this model is general and therefore it can be applied to other nanoparticle systems, including different materials and geometries. Future work on the Au bipyramid nanoparticles would involve high resolution electron tomography to confirm the geometry proposed in the model. Also, a model to explain the origin of growth mechanism forming the chiral shapes observed in these nanoparticles. This study would look at the geometries and shapes of the bipyramids at different growth times under the same conditions.

The overall theme throughout this thesis is the use of scanning transmission electron microscopy to study particles at the nanoscale. Both real space (images, tomography) and reciprocal space (diffraction) techniques have been used and quantitatively analysed to extract information about the objects of interest. The advent and ubiquity of aberration-corrected electron microscopes has opened the door to atomic resolution electron tomography which is a natural step to observe atomic arrangements in detail, and to understand the assembly of materials at a more fundamental level.

Appendix A

A.1 Te nanorods: Model and HAADF images that support partial screw dislocations

This appendix presents in general terms the model and high-resolution images that support the theory of a partial screw dislocation in Te. A typical dissociated dislocation has discontinuity in atomic rows characterized by figure A-1-B. When viewed along the $[\bar{1}2\bar{1}0]$ direction atomic displacements are only observed when the screw dislocation is a partial with Burgers vector $b = {}^{c}/_{3}\,[0001]$. This type of atomic arrangement is observed in the prepared Te nanorods viewed along the $[\bar{1}2\bar{1}0]$ direction as shown in Figure A-2. The image was taken by Peter Ercius and the elasticity model to identify the partial screw dislocation was performed Anas Abu-Odeh.

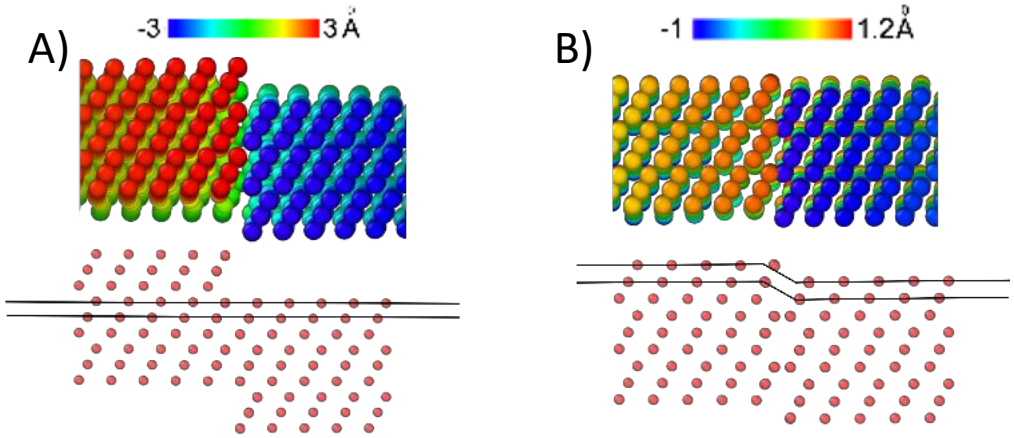

Figure A-1 Screw dislocations models for Te viewed along $[\bar{1}2\bar{1}0]$ with Burgers vectors A) $b =$ c$[0001]$ and B) $b = {}^{c}/_{3}\,[0001]$. The colour scales represent the magnitude of atomic displacements along the c-axis due to the dislocation. The single colour models (red dots) are side views along the $[\bar{1}2\bar{1}0]$ direction, that keep just the frontmost atoms. Model and figure were created by Anas Abu-Odeh and Assaf Ben-Moshe, respectively.

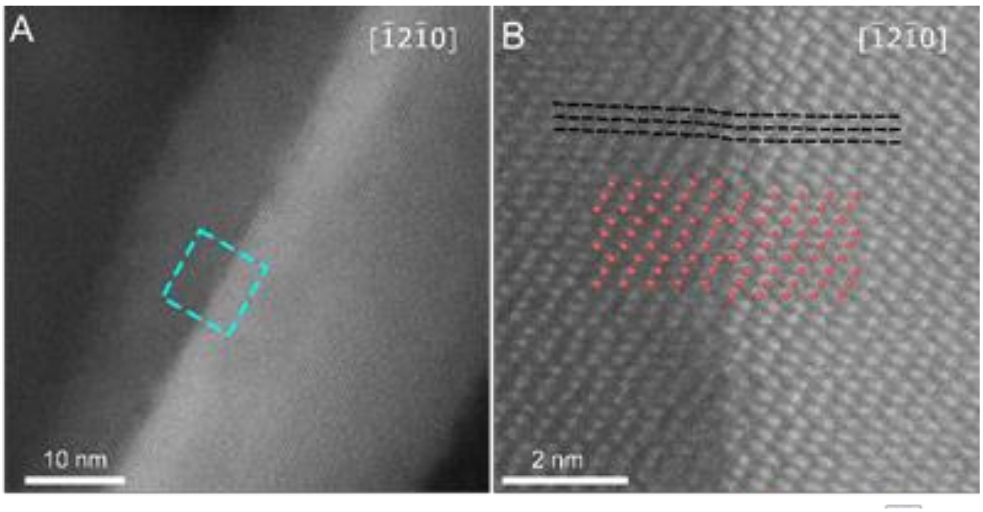

Figure A-2 (A) HAADF-STEM image of a nanorod observed along the [$\bar{1}2\bar{1}0$] direction. (B) An enlarged, rotated view of the section marked by a cyan frame in 3A. A 2D section of the model for a dissociated dislocation (red dots) is placed onto the image for comparison. The discontinuity in atomic rows, typical of the dissociated dislocation, is observed in both image and model. Black dashed lines that trace atomic rows in the image also highlight this discontinuity. HAADF-STEM image and figure were performed by Peter Ercius and Assaf Ben-Moshe, respectively.

A.2 Code repository

The 4D-STEM algorithms and general codes developed by the author have been made available on Github at: https://github.com/dasilvaale/.

References

(1) Williams, D. B.; Carter, C. B. *Transmission Electron Microscopy: A Textbook for Materials Science*, 2nd ed.; Springer: New York, 2008.

(2) Rutherford, E. The Scattering of α and β Particles by Matter and Structure of the Atom. *Philos. Mag* **1911**, *21*, 669–688. https://doi.org/10.1080/14786440508637080.

(3) Lord Rayleigh, F. R. S. XXXI. Investigations in Optics, with Special Reference to the Spectroscope. *The London, Edinburgh, and Dublin Philosophical Magazine and Journal of Science* **1879**, *8* (49), 261–274. https://doi.org/10.1080/14786447908639684.

(4) Kisielowski, C.; Freitag, B.; Bischoff, M.; van Lin, H.; Lazar, S.; Knippels, G.; Tiemeijer, P.; van der Stam, M.; von Harrach, S.; Stekelenburg, M.; Haider, M.; Uhlemann, S.; Müller, H.; Hartel, P.; Kabius, B.; Miller, D.; Petrov, I.; Olson, E. A.; Donchev, T.; Kenik, E. A.; Lupini, A. R.; Bentley, J.; Pennycook, S. J.; Anderson, I. M.; Minor, A. M.; Schmid, A. K.; Duden, T.; Radmilovic, V.; Ramasse, Q. M.; Watanabe, M.; Erni, R.; Stach, E. A.; Denes, P.; Dahmen, U. Detection of Single Atoms and Buried Defects in Three Dimensions by Aberration-Corrected Electron Microscope with 0.5-Å Information Limit. *Microscopy and Microanalysis* **2008**, *14* (5), 469–477. https://doi.org/10.1017/S1431927608080902.

(5) Shirota, K.; Yamamoto, T.; Yanaka, T.; Vingsbo, O. On Dark Field Techniques in Transmission Electron Microscopy. *Ultramicroscopy* **1975**, *1* (1), 67–78. https://doi.org/10.1016/S0304-3991(75)80008-8.

(6) Rauch, E. F.; Véron, M. Virtual Dark-Field Images Reconstructed from Electron Diffraction Patterns. *The European Physical Journal Applied Physics* **2014**, *66* (1), 10701. https://doi.org/10.1051/epjap/2014130556.

(7) Gammer, C.; Burak Ozdol, V.; Liebscher, C. H.; Minor, A. M. Diffraction Contrast Imaging Using Virtual Apertures. *Ultramicroscopy* **2015**, *155*, 1–10. https://doi.org/10.1016/j.ultramic.2015.03.015.

(8) Hartel, P.; Rose, H.; Dinges, C. Conditions and Reasons for Incoherent Imaging in STEM. *Ultramicroscopy* **1996**, *63* (2), 93–114. https://doi.org/10.1016/0304-3991(96)00020-4.

(9) Li, Z. Scanning Transmission Electron Microscopy Studies of Mono- and Bimetallic Nanoclusters. In *Frontiers of Nanoscience*; Elsevier, 2012; Vol. 3, pp 213–247.

(10) *Nanoparticles in Biology and Medicine*; Soloviev, M., Ed.; Methods in Molecular Biology; Humana Press: Totowa, NJ, 2012; Vol. 906. https://doi.org/10.1007/978-1-61779-953-2.

(11) Wells, D. M.; Rossi, G.; Ferrando, R.; Palmer, R. E. Metastability of the Atomic Structures of Size-Selected Gold Nanoparticles. *Nanoscale* **2015**, *7* (15), 6498–6503. https://doi.org/10.1039/C4NR05811A.

(12) Bragg, W. H.; Bragg, W. L. The Reflection of X-Rays by Crystals. *Proc. Roy. Soc. Lond* **1913**, *A88*, 428–438. https://doi.org/10.1098/rspa.1913.0040.

(13) Wang, Z. L. *Elastic and Inelastic Scattering in Electron Diffraction and Imaging*; Springer US: Boston, MA, 1995. https://doi.org/10.1007/978-1-4899-1579-5.

(14) Jones, P. M.; Rackham, G. M.; Steeds, J. W. Higher Order Laue Zone Effects in Electron Diffraction and Their Use in Lattice Parameter Determination. *Proceedings of the Royal Society of London. A. Mathematical and Physical Sciences* **1977**, *354* (1677), 197–222. https://doi.org/10.1098/rspa.1977.0064.

(15) Kilaas, R.; O'Keefe, M. A.; Krishnan, K. M. On the Inclusion of Upper Laue Layers in Computational Methods in High Resolution Transmission Electron Microscopy. *Ultramicroscopy* **1987**, *21* (1), 47–61. https://doi.org/10.1016/0304-3991(87)90006-4.
(16) Champness, P. E. Convergent Beam Electron Diffraction. *Cambridge University* **1987**, *51* (359), 33–48. https://doi.org/10.1180/minmag.1987.051.359.04.
(17) Ophus, C. Four-Dimensional Scanning Transmission Electron Microscopy (4D-STEM): From Scanning Nanodiffraction to Ptychography and Beyond. *Microscopy and Microanalysis* **2019**, *25* (3), 563–582. https://doi.org/10.1017/S1431927619000497.
(18) Zuo, J.-M.; Tao, J. Scanning Electron Nanodiffraction and Diffraction Imaging. In *Scanning Transmission Electron Microscopy*; Pennycook, S. J., Nellist, P. D., Eds.; Springer New York: New York, NY, 2011; pp 393–427. https://doi.org/10.1007/978-1-4419-7200-2_9.
(19) Cowley, J. M. Electron Nanodiffraction. *Microscopy Research and Technique* **1999**, *46* (2), 75–97. https://doi.org/10.1002/(SICI)1097-0029(19990715)46:2<75::AID-JEMT2>3.0.CO;2-S.
(20) Cowley, J. M. Applications of Electron Nanodiffraction. *Micron* **2004**, *35* (5), 345–360. https://doi.org/10.1016/j.micron.2003.12.002.
(21) Lavakumar, A.; Morgan & Claypool Publishers; Institute of Physics (Great Britain). *Concepts in Physical Metallurgy: Concise Lecture Notes*; 2017.
(22) Dubrovinsky, L. S.; Saxena, S. K. Thermal Expansion of Periclase (MgO) and Tungsten (W) to Melting Temperatures. *Physics and Chemistry of Minerals* **1997**, *24* (8), 547–550. https://doi.org/10.1007/s002690050070.
(23) Basinski, Z. S.; Hume-Rothery, W.; Sutton, A. L. The Lattice Expansion of Iron. *Royal Society* **1955**, *229* (1179), 9. https://doi.org/10.1098/rspa.1955.0102.
(24) Foiles, S. M.; Baskes, M. I.; Daw, M. S. Embedded-Atom-Method Functions for the Fcc Metals Cu, Ag, Au, Ni, Pd, Pt, and Their Alloys. *Physical Review B* **1986**, *33* (12), 7983–7991. https://doi.org/10.1103/PhysRevB.33.7983.
(25) Wan, J.; Fan, Y. L.; Gong, D. W.; Shen, S. G.; Fan, X. Q. Surface Relaxation and Stress of Fcc Metals: Cu, Ag, Au, Ni, Pd, Pt, Al and Pb. *Modelling and Simulation in Materials Science and Engineering* **1999**, *7* (2), 189–206. https://doi.org/10.1088/0965-0393/7/2/005.
(26) Bacon, D. J. A Review of Computer Models of Point Defects in Hcp Metals. *Journal of Nuclear Materials* **1988**, *159*, 176–189. https://doi.org/10.1016/0022-3115(88)90092-X.
(27) Patterson, R. A. Crystal Structure of Titanium and Chromium. *Physical Review* **1925**, *26* (1), 56–59. https://doi.org/10.1103/PhysRev.26.56.
(28) Sloane, N. J. A. Kepler's Conjecture Confirmed. *Nature* **1998**, *395* (6701), 435–436. https://doi.org/10.1038/26609.
(29) Frank, J. *Electron Tomography: Three-Dimensional Imaging with the Transmission Electron Microscope*; Springer US: Boston, MA, 1992.
(30) Thorsten M. Buzug. *Computed Tomography*; Springer-Verlag Berlin Heidelberg: Leipzig, Germany, 2008.
(31) John C.Russ. *The Image Processing Handbook*, Sixth Edition.; CRC Press by Taylor and Francis Group, LLC, 2011.
(32) Semenov, S. Microwave Tomography: Review of the Progress towards Clinical Applications. *Philosophical Transactions of the Royal Society A: Mathematical, Physical and Engineering Sciences* **2009**, *367* (1900), 3021–3042. https://doi.org/10.1098/rsta.2009.0092.
(33) Vontobel, P.; Lehmann, E. H.; Hassanein, R.; Frei, G. Neutron Tomography: Method and Applications. *Physica B: Condensed Matter* **2006**, *385–386*, 475–480. https://doi.org/10.1016/j.physb.2006.05.252.

(34) Pesente, S.; Vanini, S.; Benettoni, M.; Bonomi, G.; Calvini, P.; Checchia, P.; Conti, E.; Gonella, F.; Nebbia, G.; Squarcia, S.; Viesti, G.; Zenoni, A.; Zumerle, G. First Results on Material Identification and Imaging with a Large-Volume Muon Tomography Prototype. *Nuclear Instruments and Methods in Physics Research Section A: Accelerators, Spectrometers, Detectors and Associated Equipment* **2009**, *604* (3), 738–746. https://doi.org/10.1016/j.nima.2009.03.017.

(35) Bonetta, L. Zooming in on Electron Tomography. *Nature Methods* **2005**, *2* (2), 139–145. https://doi.org/10.1038/nmeth0205-139.

(36) Ercius, P.; Alaidi, O.; Rames, M. J.; Ren, G. Electron Tomography: A Three-Dimensional Analytic Tool for Hard and Soft Materials Research. *Advanced Materials* **2015**, *27* (38), 5638–5663. https://doi.org/10.1002/adma.201501015.

(37) Miao, J.; Ercius, P.; Billinge, S. J. L. Atomic Electron Tomography: 3D Structures without Crystals. *Science* **2016**, *353* (6306), aaf2157–aaf2157. https://doi.org/10.1126/science.aaf2157.

(38) Scott, M. C.; Theis, W.; Xu, R.; Wu, L.; Chen, C.-C.; Ophus, C.; Ercius, P.; Miao, J. Implementation of Atomic Resolution Electron Tomography of a Needle Sample. *Microscopy and Microanalysis* **2015**, *21* (S3), 1523–1524. https://doi.org/10.1017/S1431927615008399.

(39) Xu, R.; Chen, C.-C.; Wu, L.; Scott, M. C.; Theis, W.; Ophus, C.; Bartels, M.; Yang, Y.; Ramezani-Dakhel, H.; Sawaya, M. R.; Heinz, H.; Marks, L. D.; Ercius, P.; Miao, J. Three-Dimensional Coordinates of Individual Atoms in Materials Revealed by Electron Tomography. *Nature Materials* **2015**, *14* (11), 1099–1103. https://doi.org/10.1038/nmat4426.

(40) Levin, B. D. A.; Padgett, E.; Chen, C.-C.; Scott, M. C.; Xu, R.; Theis, W.; Jiang, Y.; Yang, Y.; Ophus, C.; Zhang, H.; Ha, D.-H.; Wang, D.; Yu, Y.; Abruña, H. D.; Robinson, R. D.; Ercius, P.; Kourkoutis, L. F.; Miao, J.; Muller, D. A.; Hovden, R. Nanomaterial Datasets to Advance Tomography in Scanning Transmission Electron Microscopy. *Scientific Data* **2016**, *3* (1). https://doi.org/10.1038/sdata.2016.41.

(41) *Electron Tomography: Methods for Three-Dimensional Visualization of Structures in the Cell*, 2nd ed.; Frank, J., Ed.; Springer: New York ; London, 2006.

(42) Mastronarde, D. N. Dual-Axis Tomography: An Approach with Alignment Methods That Preserve Resolution. *Journal of Structural Biology* **1997**, *120* (3), 343–352. https://doi.org/10.1006/jsbi.1997.3919.

(43) Zheng, S. Q.; Matsuda, A.; Braunfeld, M. B.; Sedat, J. W.; Agard, D. A. Dual-Axis Target Mapping and Automated Sequential Acquisition of Dual-Axis EM Tomographic Data. *Journal of Structural Biology* **2009**, *168* (2), 323–331. https://doi.org/10.1016/j.jsb.2009.06.010.

(44) Padgett, E.; Hovden, R.; DaSilva, J. C.; Levin, B. D. A.; Grazul, J. L.; Hanrath, T.; Muller, D. A. A Simple Preparation Method for Full-Range Electron Tomography of Nanoparticles and Fine Powders. *Microscopy and Microanalysis* **2017**, *23* (06), 1150–1158. https://doi.org/10.1017/S1431927617012764.

(45) Koster, A. J.; Grimm, R.; Typke, D.; Hegerl, R.; Stoschek, A.; Walz, J.; Baumeister, W. Perspectives of Molecular and Cellular Electron Tomography. *Journal of Structural Biology* **1997**, *120* (3), 276–308. https://doi.org/10.1006/jsbi.1997.3933.

(46) McEwen, B. F.; Radermacher, M.; Rieder, C. L.; Frank, J. Tomographic Three-Dimensional Reconstruction of Cilia Ultrastructure from Thick Sections. *Proceedings of the National Academy of Sciences* **1986**, *83* (23), 9040–9044. https://doi.org/10.1073/pnas.83.23.9040.

(47) Resch, G. P. Software for Automated Acquisition of Electron Tomography Tilt Series. In *Methods in Cell Biology*; Elsevier, 2019; Vol. 152, pp 135–178. https://doi.org/10.1016/bs.mcb.2019.05.002.
(48) Mastronarde, D. N. Automated Electron Microscope Tomography Using Robust Prediction of Specimen Movements. *Journal of Structural Biology* **2005**, *152* (1), 36–51. https://doi.org/10.1016/j.jsb.2005.07.007.
(49) Fung, J. C.; Liu, W.; de Ruijter, W. J.; Chen, H.; Abbey, C. K.; Sedat, J. W.; Agard, D. A. Toward Fully Automated High-Resolution Electron Tomography. *Journal of Structural Biology* **1996**, *116* (1), 181–189. https://doi.org/10.1006/jsbi.1996.0029.
(50) Mastronarde, D. N. Fiducial Marker and Hybrid Alignment Methods for Single- and Double-Axis Tomography. In *Electron Tomography*; Frank, J., Ed.; Springer New York: New York, NY, 2006; pp 163–185. https://doi.org/10.1007/978-0-387-69008-7_6.
(51) Owen, C. H.; Landis, W. J. Alignment of Electron Tomographic Series by Correlation without the Use of Gold Particles. *Ultramicroscopy* **1996**, *63* (1), 27–38. https://doi.org/10.1016/0304-3991(95)00154-9.
(52) Midgley, P. A.; Weyland, M. 3D Electron Microscopy in the Physical Sciences: The Development of Z-Contrast and EFTEM Tomography. *Ultramicroscopy* **2003**, *96* (3–4), 413–431. https://doi.org/10.1016/S0304-3991(03)00105-0.
(53) Liu, Y.; Penczek, P. A.; McEwen, B. F.; Frank, J. A Marker-Free Alignment Method for Electron Tomography. *Ultramicroscopy* **1995**, *58* (3–4), 393–402. https://doi.org/10.1016/0304-3991(95)00006-M.
(54) Brandt, S.; Heikkonen, J.; Engelhardt, P. Multiphase Method for Automatic Alignment of Transmission Electron Microscope Images Using Markers. *Journal of Structural Biology* **2001**, *133* (1), 10–22. https://doi.org/10.1006/jsbi.2001.4343.
(55) McEwen, B. F.; Renken, C.; Marko, M.; Mannella, C. Chapter 6 Principles and Practice in Electron Tomography. In *Methods in Cell Biology*; Elsevier, 2008; Vol. 89, pp 129–168. https://doi.org/10.1016/S0091-679X(08)00606-7.
(56) Pan, S.; Kak, A. A Computational Study of Reconstruction Algorithms for Diffraction Tomography: Interpolation versus Filtered-Backpropagation. *IEEE Transactions on Acoustics, Speech, and Signal Processing* **1983**, *31* (5), 1262–1275. https://doi.org/10.1109/TASSP.1983.1164196.
(57) Penczek, P. A. Fundamentals of Three-Dimensional Reconstruction from Projections. In *Methods in Enzymology*; Elsevier, 2010; Vol. 482, pp 1–33. https://doi.org/10.1016/S0076-6879(10)82001-4.
(58) Stark, H.; Woods, J.; Paul, I.; Hingorani, R. Direct Fourier Reconstruction in Computer Tomography. *IEEE Transactions on Acoustics, Speech, and Signal Processing* **1981**, *29* (2), 237–245. https://doi.org/10.1109/TASSP.1981.1163528.
(59) Mersereau, R. M. Direct Fourier Transform Techniques in 3-D Image Reconstruction. *Computers in Biology and Medicine* **1976**, *6* (4), 247-IN4. https://doi.org/10.1016/0010-4825(76)90064-0.
(60) Gilbert, P. Iterative Methods for the Three-Dimensional Reconstruction of an Object from Projections. *J. theor. Biol* **1971**, *36*, 13.
(61) Mastronarde, D. N.; Held, S. R. Automated Tilt Series Alignment and Tomographic Reconstruction in IMOD. *Journal of Structural Biology* **2017**, *197* (2), 102–113. https://doi.org/10.1016/j.jsb.2016.07.011.
(62) Crowther, R. A.; DeRosier, D. J.; Klug, F. R. S. The Reconstruction of a Three-Dimensional Structure from Projections and Its Application to Electron Microscopy. *Proceedings of the Royal Society of London. A. Mathematical and Physical Sciences* **1970**, *317* (1530), 319–340. https://doi.org/10.1098/rspa.1970.0119.

(63) Radermacher, M. Three-Dimensional Reconstruction of Single Particles from Random and Nonrandom Tilt Series. *Journal of Electron Microscopy Technique* **1988**, *9* (4), 359–394. https://doi.org/10.1002/jemt.1060090405.
(64) Lee, J.-H.; Suh, H.; Lee, S.-G.; Kim, J.-G.; Yoo, S. J. Advanced Method for the Accurate Measurement of Tilt Angle in a Transmission Electron Microscopy Goniometer. *Journal of Analytical Science and Technology* **2018**, *9* (1). https://doi.org/10.1186/s40543-018-0140-6.
(65) Biskupek, J.; Leschner, J.; Walther, P.; Kaiser, U. Optimization of STEM Tomography Acquisition — A Comparison of Convergent Beam and Parallel Beam STEM Tomography. *Ultramicroscopy* **2010**, *110* (9), 1231–1237. https://doi.org/10.1016/j.ultramic.2010.05.008.
(66) Feng, J.; Somlyo, A. P.; Somlyo, A. V.; Shao, Z. Automated Electron Tomography with Scanning Transmission Electron Microscopy. *Journal of Microscopy* **2007**, *228* (3), 406–412. https://doi.org/10.1111/j.1365-2818.2007.01859.x.
(67) Ziese, U.; Geerts, W. J. C.; Van Der Krift, T. P.; Verkleij, A. J.; Koster, A. J. Correction of Autofocusing Errors Due to Specimen Tilt for Automated Electron Tomography. *Journal of Microscopy* **2003**, *211* (2), 179–185. https://doi.org/10.1046/j.1365-2818.2003.01153.x.
(68) *Springer Handbook of Microscopy*; Hawkes, P. W., Spence, J. C. H., Eds.; Springer Handbooks; Springer International Publishing: Cham, 2019. https://doi.org/10.1007/978-3-030-00069-1.
(69) Zaluzec, N. J. Quantitative Measurements of Magnetic Vortices Using Position Resolved Diffraction in Lorentz Stem. *Microscopy and Microanalysis* **2002**, *8* (S02), 376–377. https://doi.org/10.1017/S143192760210064X.
(70) Gammer, C.; Ophus, C.; Pekin, T. C.; Eckert, J.; Minor, A. M. Local Nanoscale Strain Mapping of a Metallic Glass during *in Situ* Testing. *Applied Physics Letters* **2018**, *112* (17), 171905. https://doi.org/10.1063/1.5025686.
(71) Cooper, D.; Denneulin, T.; Bernier, N.; Béché, A.; Rouvière, J.-L. Strain Mapping of Semiconductor Specimens with Nm-Scale Resolution in a Transmission Electron Microscope. *Micron* **2016**, *80*, 145–165. https://doi.org/10.1016/j.micron.2015.09.001.
(72) Béché, A.; Rouvière, J. L.; Barnes, J. P.; Cooper, D. Strain Measurement at the Nanoscale: Comparison between Convergent Beam Electron Diffraction, Nano-Beam Electron Diffraction, High Resolution Imaging and Dark Field Electron Holography. *Ultramicroscopy* **2013**, *131*, 10–23. https://doi.org/10.1016/j.ultramic.2013.03.014.
(73) Ophus, C.; Ercius, P.; Huijben, M.; Ciston, J. Non-Spectroscopic Composition Measurements of $SrTiO_3$-$La_{0.7}Sr_{0.3}MnO_3$ Multilayers Using Scanning Convergent Beam Electron Diffraction. *Applied Physics Letters* **2017**, *110* (6), 063102. https://doi.org/10.1063/1.4975932.
(74) Pekin, T. C.; Gammer, C.; Ciston, J.; Minor, A. M.; Ophus, C. Optimizing Disk Registration Algorithms for Nanobeam Electron Diffraction Strain Mapping. *Ultramicroscopy* **2017**, *176*, 170–176. https://doi.org/10.1016/j.ultramic.2016.12.021.
(75) Savitzky, B.; Zeltmann, S. E.; Barnard, E.; Brown, H. G.; Henderson, M.; Ginsburg, D.; Ophus, C. Py4DSTEM. **2019**, *v0.5*. https://doi.org/10.5281/zenodo.3333960.
(76) de la Peña, F.; Ostasevicius, T.; Tonaas Fauske, V.; Burdet, P.; Prestat, E.; Jokubauskas, P.; Nord, M.; Garmannslund, A. HyperSpy 1.3.1. **2018**. https://doi.org/10.5281/zenodo.1221347.
(77) Jenkins, S. J. *Chirality at Solid Surfaces*; John Wiley & Sons, Ltd: Chichester, UK, 2018. https://doi.org/10.1002/9781118880173.
(78) Hananel, U.; Ben-Moshe, A.; Diamant, H.; Markovich, G. Spontaneous and Directed Symmetry Breaking in the Formation of Chiral Nanocrystals. *Proceedings of the National*

Academy of Sciences **2019**, *116* (23), 11159–11164. https://doi.org/10.1073/pnas.1821923116.

(79) Weissbuch, I.; Lahav, M. Crystalline Architectures as Templates of Relevance to the Origins of Homochirality. *Chemical Reviews* **2011**, *111* (5), 3236–3267. https://doi.org/10.1021/cr1002479.

(80) David B. Amabilino. - *Chirality at the Nanoscale_ Nanoparticles, Surfaces, Materials and More*; WILEY-VCH Verlag GmbH & Co. KGaA, Weinheim, 2009.

(81) Wang, Z.; Cheng, F.; Winsor, T.; Liu, Y. Optical Chiral Metamaterials: A Review of the Fundamentals, Fabrication Methods and Applications. *Nanotechnology* **2016**, *27* (41), 412001. https://doi.org/10.1088/0957-4484/27/41/412001.

(82) Hazen, R. M.; Sholl, D. S. Chiral Selection on Inorganic Crystalline Surfaces. *Nature Materials* **2003**, *2* (6), 367–374. https://doi.org/10.1038/nmat879.

(83) Matthews, S. J.; McCoy, C. Thalidomide: A Review of Approved and Investigational Uses. *Clinical Therapeutics* **2003**, *25* (2), 342–395. https://doi.org/10.1016/S0149-2918(03)80085-1.

(84) Noguez, C.; Garzón, I. L. Optically Active Metal Nanoparticles. *Chemical Society Reviews* **2009**, *38* (3), 757. https://doi.org/10.1039/b800404h.

(85) Ben-Moshe, A.; Wolf, S. G.; Sadan, M. B.; Houben, L.; Fan, Z.; Govorov, A. O.; Markovich, G. Enantioselective Control of Lattice and Shape Chirality in Inorganic Nanostructures Using Chiral Biomolecules. *Nature Communications* **2014**, *5* (1). https://doi.org/10.1038/ncomms5302.

(86) Brown, G. E.; Henrich, V. E.; Casey, W. H.; Clark, D. L.; Eggleston, C.; Felmy, A.; Goodman, D. W.; Grätzel, M.; Maciel, G.; McCarthy, M. I.; Nealson, K. H.; Sverjensky, D. A.; Toney, M. F.; Zachara, J. M. Metal Oxide Surfaces and Their Interactions with Aqueous Solutions and Microbial Organisms. *Chemical Reviews* **1999**, *99* (1), 77–174. https://doi.org/10.1021/cr980011z.

(87) Wang, P.; Yu, S.-J.; Govorov, A. O.; Ouyang, M. Cooperative Expression of Atomic Chirality in Inorganic Nanostructures. *Nature Communications* **2017**, *8* (1). https://doi.org/10.1038/ncomms14312.

(88) Gal, J. The Discovery of Biological Enantioselectivity: Louis Pasteur and the Fermentation of Tartaric Acid, 1857—A Review and Analysis 150 Yr Later. *Chirality* **2008**, *20* (1), 5–19. https://doi.org/10.1002/chir.20494.

(89) Lee, H.-E.; Ahn, H.-Y.; Mun, J.; Lee, Y. Y.; Kim, M.; Cho, N. H.; Chang, K.; Kim, W. S.; Rho, J.; Nam, K. T. Amino-Acid- and Peptide-Directed Synthesis of Chiral Plasmonic Gold Nanoparticles. *Nature* **2018**, *556* (7701), 360–365. https://doi.org/10.1038/s41586-018-0034-1.

(90) Morales-Vidal, J.; López, N.; Ortuño, M. A. Chirality Transfer in Gold Nanoparticles by L -Cysteine Amino Acid: A First-Principles Study. *The Journal of Physical Chemistry C* **2019**, *123* (22), 13758–13764. https://doi.org/10.1021/acs.jpcc.9b02918.

(91) Yao, H. Monolayer-Protected Metal Nanoclusters with Chirality: Synthesis, Size Fractionation, Optical Activity and Asymmetric Transformation. In *Handbook of Nanoparticles*; Aliofkhazraei, M., Ed.; Springer International Publishing: Cham, 2016; pp 191–216. https://doi.org/10.1007/978-3-319-15338-4_12.

(92) Govorov, A. O.; Gun'ko, Y. K.; Slocik, J. M.; Gérard, V. A.; Fan, Z.; Naik, R. R. Chiral Nanoparticle Assemblies: Circular Dichroism, Plasmonic Interactions, and Exciton Effects. *Journal of Materials Chemistry* **2011**, *21* (42), 16806. https://doi.org/10.1039/c1jm12345a.

(93) Tizei, L. H. G.; Craven, A. J.; Zagonel, L. F.; Tencé, M.; Stéphan, O.; Chiaramonte, T.; Cotta, M. A.; Ugarte, D. Enhanced Eshelby Twist on Thin Wurtzite InP Nanowires and

Measurement of Local Crystal Rotation. *Physical Review Letters* **2011**, *107* (19). https://doi.org/10.1103/PhysRevLett.107.195503.

(94) Brown, P. J.; Forsyth, J. B. The Crystal Structure and Optical Activity of Tellurium. *Acta Crystallographica Section A Foundations of Crystallography* **1996**, *52* (3), 408–412. https://doi.org/10.1107/S0108767395017144.

(95) Bouad, N.; Chapon, L.; Marin-Ayral, R.-M.; Bouree-Vigneron, F.; Tedenac, J.-C. Neutron Powder Diffraction Study of Strain and Crystallite Size in Mechanically Alloyed PbTe. *Journal of Solid State Chemistry* **2003**, *173* (1), 189–195. https://doi.org/10.1016/S0022-4596(03)00017-3.

(96) Panahi-Kalamuei, M.; Rajabpour, P.; Salavati-Niasari, M.; Zarghami, Z.; Mousavi-Kamazani, M. Simple and Rapid Methods Based Microwave and Sonochemistry for Synthesizing of Tellurium Nanostructures Using Novel Starting Reagents for Solar Cells. *Journal of Materials Science: Materials in Electronics* **2015**, *26* (6), 3691–3699. https://doi.org/10.1007/s10854-015-2887-5.

(97) Lin, S.; Li, W.; Chen, Z.; Shen, J.; Ge, B.; Pei, Y. Tellurium as a High-Performance Elemental Thermoelectric. *Nature Communications* **2016**, *7* (1). https://doi.org/10.1038/ncomms10287.

(98) Guisbiers, G.; Mimun, L. C.; Mendoza-Cruz, R.; Nash, K. L. Synthesis of Tunable Tellurium Nanoparticles. *Semiconductor Science and Technology* **2017**, *32* (4), 04LT01. https://doi.org/10.1088/1361-6641/aa6173.

(99) Okuyama, Y.; Sugiyama, Y.; Ideta, S.; Tanaka, K.; Hirahara, T. Growth and Atomic Structure of Tellurium Thin Films Grown on Bi2Te3. *Applied Surface Science* **2017**, *398*, 125–129. https://doi.org/10.1016/j.apsusc.2016.11.196.

(100) Kremer, J. R.; Mastronarde, D. N.; McIntosh, J. R. Computer Visualization of Three-Dimensional Image Data Using IMOD. *Journal of Structural Biology* **1996**, *116* (1), 71–76. https://doi.org/10.1006/jsbi.1996.0013.

(101) Pearu Peterson, E. J.; Travis Oliphant. SciPy: Open Source Scientific Tools for Python. 2001.

(102) Orme, C. A.; Noy, A.; Wierzbicki, A.; McBride, M. T.; Grantham, M.; Teng, H. H.; Dove, P. M.; DeYoreo, J. J. Formation of Chiral Morphologies through Selective Binding of Amino Acids to Calcite Surface Steps. *Nature* **2001**, *411* (6839), 775–779. https://doi.org/10.1038/35081034.

(103) Meng, F.; Estruga, M.; Forticaux, A.; Morin, S. A.; Wu, Q.; Hu, Z.; Jin, S. Formation of Stacking Faults and the Screw Dislocation-Driven Growth: A Case Study of Aluminum Nitride Nanowires. *ACS Nano* **2013**, *7* (12), 11369–11378. https://doi.org/10.1021/nn4052293.

(104) Meng, F.; Morin, S. A.; Forticaux, A.; Jin, S. Screw Dislocation Driven Growth of Nanomaterials. *Accounts of Chemical Research* **2013**, *46* (7), 1616–1626. https://doi.org/10.1021/ar400003q.

(105) Zhang, L.; Liu, K.; Wong, A. B.; Kim, J.; Hong, X.; Liu, C.; Cao, T.; Louie, S. G.; Wang, F.; Yang, P. Three-Dimensional Spirals of Atomic Layered MoS $_2$. *Nano Letters* **2014**, *14* (11), 6418–6423. https://doi.org/10.1021/nl502961e.

(106) Chen, L.; Liu, B.; Abbas, A. N.; Ma, Y.; Fang, X.; Liu, Y.; Zhou, C. Screw-Dislocation-Driven Growth of Two-Dimensional Few-Layer and Pyramid-like WSe $_2$ by Sulfur-Assisted Chemical Vapor Deposition. *ACS Nano* **2014**, *8* (11), 11543–11551. https://doi.org/10.1021/nn504775f.

(107) Nanev, C. N. On the Slope of the Growing Pyramids. *Kristall und Technik* **1977**, *12* (6), 587–598. https://doi.org/10.1002/crat.19770120609.

(108) Nanev, C. N. On the Polygonized Growth of a Step Anchoredin Two Screw Dislocations of Opposite Sign. *Journal of Crystal Growth* **1976**, *35* (1), 113–119. https://doi.org/10.1016/0022-0248(76)90252-9.

(109) Liu, D.; Cho, S. J.; Zhang, H.; Carlos, C. R.; Kalapala, A. R. K.; Park, J.; Kim, J.; Dalmau, R.; Gong, J.; Moody, B.; Wang, X.; Albrecht, J. D.; Zhou, W.; Ma, Z. Influences of Screw Dislocations on Electroluminescence of AlGaN/AlN-Based UVC LEDs. *AIP Advances* **2019**, *9* (8), 085128. https://doi.org/10.1063/1.5108743.

(110) Chuvyrov, A. N.; Mazitov, R. M. Structure and Properties of Quartz Crystals Grown from Fluoride Solutions: I. The Morphology of Basal Pinacoid Habit. *Crystallography Reports* **2008**, *53* (5), 894–899. https://doi.org/10.1134/S106377450805026X.

(111) Zhuang, A.; Li, J.-J.; Wang, Y.-C.; Wen, X.; Lin, Y.; Xiang, B.; Wang, X.; Zeng, J. Screw-Dislocation-Driven Bidirectional Spiral Growth of Bi $_2$ Se $_3$ Nanoplates. *Angewandte Chemie International Edition* **2014**, *53* (25), 6425–6429. https://doi.org/10.1002/anie.201403530.

(112) Chirilla, R.; Iliescu, B. Dislocations in Synthetic Quartz. *Crystal Research and Technology* **1994**, *29* (2), 159–169. https://doi.org/10.1002/crat.2170290202.

(113) Morin, S. A.; Bierman, M. J.; Tong, J.; Jin, S. Mechanism and Kinetics of Spontaneous Nanotube Growth Driven by Screw Dislocations. *Science* **2010**, *328* (5977), 476–480. https://doi.org/10.1126/science.1182977.

(114) Heindl, J.; Strunk, H. P.; Heydemann, V. D.; Pensl, G. Micropipes: Hollow Tubes in Silicon Carbide. *physica status solidi (a)* **1997**, *162* (1), 251–262. https://doi.org/10.1002/1521-396X(199707)162:1<251::AID-PSSA251>3.0.CO;2-7.

(115) Liu, Y.; Wang, J.; Kim, S.; Sun, H.; Yang, F.; Fang, Z.; Tamura, N.; Zhang, R.; Song, X.; Wen, J.; Xu, B. Z.; Wang, M.; Lin, S.; Yu, Q.; Tom, K. B.; Deng, Y.; Turner, J.; Chan, E.; Jin, D.; Ritchie, R. O.; Minor, A. M.; Chrzan, D. C.; Scott, M. C.; Yao, J. Helical van Der Waals Crystals with Discretized Eshelby Twist. *Nature* **2019**, *570* (7761), 358–362. https://doi.org/10.1038/s41586-019-1308-y.

(116) Furuta, N.; Itinose, H.; Maruyama, N.; Ohasi, Y. Morphology and Dislocation Structure of Tellurium Whiskers Grown from the Vapor. *Japanese Journal of Applied Physics* **1972**, *11* (8), 1113–1118. https://doi.org/10.1143/JJAP.11.1113.

(117) Maeda, K.; Takeuchi, S. Chapter 54 Enhancement of Dislocation Mobility in Semiconducting Crystals by Electronic Excitation. In *Dislocations in Solids*; Elsevier, 1996; Vol. 10, pp 443–504. https://doi.org/10.1016/S1572-4859(96)80009-X.

(118) Lavagne§, S.; Levade, C.; Vanderschaeve, G. Transmission Electron Microscopy ***in Situ*** Investigation of Dislocation Behaviour in Semiconductors and the Influence of Electronic Excitation. *Philosophical Magazine* **2006**, *86* (29–31), 4923–4940. https://doi.org/10.1080/14786430600750038.

(119) Yu, Z.; Hahn, M. A.; Calcines, J.; Krauss, T. D.; Silcox, J. Study of the Internal Structure of Individual CdSe Quantum Rods Using Electron Nanodiffraction. *Applied Physics Letters* **2005**, *86* (1), 013101. https://doi.org/10.1063/1.1843278.

(120) H.C. Shih, C.-Y. W. Determination of the Three-Dimensional Crystallographic Misorientation in Heterostructures by Selected Area Diffraction (SAD) in Cross-Sectional TEM. *Journal of Crystal Growth* **2000**, *213*, 150–156.

(121) Verch, A.; Côté, A. S.; Darkins, R.; Kim, Y.-Y.; van de Locht, R.; Meldrum, F. C.; Duffy, D. M.; Kröger, R. Correlation between Anisotropy and Lattice Distortions in Single Crystal Calcite Nanowires Grown in Confinement. *Small* **2014**, *10* (13), 2697–2702. https://doi.org/10.1002/smll.201303839.

(122) van der Walt, S.; Schönberger, J. L.; Nunez-Iglesias, J.; Boulogne, F.; Warner, J. D.; Yager, N.; Gouillart, E.; Yu, T. Scikit-Image: Image Processing in Python. *PeerJ* **2014**, *2*, e453. https://doi.org/10.7717/peerj.453.

(123) Mukhopadhyay, P.; Chaudhuri, B. B. A Survey of Hough Transform. *Pattern Recognition* **2015**, *48* (3), 993–1010. https://doi.org/10.1016/j.patcog.2014.08.027.
(124) Tico, M. Classical Geometrical Approach to Circle Fitting—Review and New Developments. *Journal of Electronic Imaging* **2003**, *12* (1), 179. https://doi.org/10.1117/1.1525792.
(125) Chernov, N. I.; Ososkov, G. A. Effective Algorithms for Circle Fitting. *Computer Physics Communications* **1984**, *33* (4), 329–333. https://doi.org/10.1016/0010-4655(84)90137-1.
(126) Chernov, N.; Lesort, C. Least Squares Fitting of Circles. *Journal of Mathematical Imaging and Vision* **2005**, *23* (3), 239–252. https://doi.org/10.1007/s10851-005-0482-8.
(127) Vosselman, G.; Haralick, R. M. Performance Analysis of Line and Circle Tting in Digital Images. 24.
(128) Shakarji, C. M. Least-Squares Fitting Algorithms of the NIST Algorithm Testing System. *Journal of Research of the National Institute of Standards and Technology* **1998**, *103* (6), 633. https://doi.org/10.6028/jres.103.043.
(129) Wu, H.; Meng, F.; Li, L.; Jin, S.; Zheng, G. Dislocation-Driven CdS and CdSe Nanowire Growth. *ACS Nano* **2012**, *6* (5), 4461–4468. https://doi.org/10.1021/nn301194v.
(130) Morin, S. A.; Jin, S. Screw Dislocation-Driven Epitaxial Solution Growth of ZnO Nanowires Seeded by Dislocations in GaN Substrates. *Nano Letters* **2010**, *10* (9), 3459–3463. https://doi.org/10.1021/nl1015409.
(131) Meng, F.; Jin, S. The Solution Growth of Copper Nanowires and Nanotubes Is Driven by Screw Dislocations. *Nano Letters* **2012**, *12* (1), 234–239. https://doi.org/10.1021/nl203385u.
(132) Rogers, W. B.; Shih, W. M.; Manoharan, V. N. Using DNA to Program the Self-Assembly of Colloidal Nanoparticles and Microparticles. *Nature Reviews Materials* **2016**, *1* (3). https://doi.org/10.1038/natrevmats.2016.8.
(133) Boles, M. A.; Engel, M.; Talapin, D. V. Self-Assembly of Colloidal Nanocrystals: From Intricate Structures to Functional Materials. *Chemical Reviews* **2016**, *116* (18), 11220–11289. https://doi.org/10.1021/acs.chemrev.6b00196.
(134) Pileni, M.-P. Self-Assembly of Inorganic Nanocrystals: Fabrication and Collective Intrinsic Properties. *Accounts of Chemical Research* **2007**, *40* (8), 685–693. https://doi.org/10.1021/ar6000582.
(135) Pileni, M. P. Supracrystals of Inorganic Nanocrystals: An Open Challenge for New Physical Properties. *Accounts of Chemical Research* **2008**, *41* (12), 1799–1809. https://doi.org/10.1021/ar800082q.
(136) Nie, Z.; Petukhova, A.; Kumacheva, E. Properties and Emerging Applications of Self-Assembled Structures Made from Inorganic Nanoparticles. *Nature Nanotechnology* **2010**, *5* (1), 15–25. https://doi.org/10.1038/nnano.2009.453.
(137) Murray, C. B.; Kagan, C. R.; Bawendi, M. G. Synthesis and Characterization of Monodisperse Nanocrystals and Close-Packed Nanocrystal Assemblies. *Annual Review of Materials Science* **2000**, *30* (1), 545–610. https://doi.org/10.1146/annurev.matsci.30.1.545.
(138) Wang, Z. L. Structural Analysis of Self-Assembling Nanocrystal Superlattices. *Advanced Materials* **1998**, *10* (1), 13–30. https://doi.org/10.1002/(SICI)1521-4095(199801)10:1<13::AID-ADMA13>3.0.CO;2-W.
(139) Wang, C.; Siu, C.; Zhang, J.; Fang, J. Understanding the Forces Acting in Self-Assembly and the Implications for Constructing Three-Dimensional (3D) Supercrystals. *Nano Research* **2015**, *8* (8), 2445–2466. https://doi.org/10.1007/s12274-015-0767-1.

(140) Si, K. J.; Chen, Y.; Shi, Q.; Cheng, W. Nanoparticle Superlattices: The Roles of Soft Ligands. *Advanced Science* **2018**, *5* (1), 1700179. https://doi.org/10.1002/advs.201700179.
(141) Grzelczak, M.; Liz-Marzán, L. M.; Klajn, R. Stimuli-Responsive Self-Assembly of Nanoparticles. *Chemical Society Reviews* **2019**, *48* (5), 1342–1361. https://doi.org/10.1039/C8CS00787J.
(142) Schmitt, J.; Hajiw, S.; Lecchi, A.; Degrouard, J.; Salonen, A.; Impéror-Clerc, M.; Pansu, B. Formation of Superlattices of Gold Nanoparticles Using Ostwald Ripening in Emulsions: Transition from Fcc to Bcc Structure. *The Journal of Physical Chemistry B* **2016**, *120* (25), 5759–5766. https://doi.org/10.1021/acs.jpcb.6b03287.
(143) Josten, E.; Wetterskog, E.; Glavic, A.; Boesecke, P.; Feoktystov, A.; Brauweiler-Reuters, E.; Rücker, U.; Salazar-Alvarez, G.; Brückel, T.; Bergström, L. Superlattice Growth and Rearrangement during Evaporation-Induced Nanoparticle Self-Assembly. *Scientific Reports* **2017**, *7* (1). https://doi.org/10.1038/s41598-017-02121-4.
(144) Cordeiro, M. A. L.; Leite, E. R.; Stach, E. A. Controlling the Formation and Structure of Nanoparticle Superlattices through Surface Ligand Behavior. *Langmuir* **2016**, *32* (44), 11606–11614. https://doi.org/10.1021/acs.langmuir.6b03026.
(145) Isojima, T.; Suh, S. K.; Vander Sande, J. B.; Hatton, T. A. Controlled Assembly of Nanoparticle Structures: Spherical and Toroidal Superlattices and Nanoparticle-Coated Polymeric Beads. *Langmuir* **2009**, *25* (14), 8292–8298. https://doi.org/10.1021/la900522u.
(146) Mirkin, C. A.; Letsinger, R. L.; Mucic, R. C.; Storhoff, J. J. A DNA-Based Method for Rationally Assembling Nanoparticles into Macroscopic Materials. *Nature* **1996**, *382* (6592), 607–609. https://doi.org/10.1038/382607a0.
(147) Alivisatos, A. P.; Johnsson, K. P.; Peng, X.; Wilson, T. E.; Loweth, C. J.; Bruchez, M. P.; Schultz, P. G. Organization of "nanocrystal Molecules" Using DNA. *Nature* **1996**, *382* (6592), 609–611. https://doi.org/10.1038/382609a0.
(148) Smilgies, D.-M.; Li, R.; Pileni, M. P. Au Nanocrystal Superlattices: Nanocrystallinity, Vicinal Surfaces, and Growth Processes. *Nanoscale* **2018**, *10* (32), 15371–15378. https://doi.org/10.1039/C8NR04606A.
(149) Fan, Z.; Grunwald, M. Energy vs. Entropy in Superlattices of Ligand-Covered Nanoparticles. 11.
(150) Dmitri V. Talapin; Elena V. Shevchenko; Christopher B. Murray; Alexey V. Titov; Petr Kral. Dipole−Dipole Interactions in Nanoparticles Superlattices. *Nano Letters* **2007**, *7* (5), 1213–1219.
(151) P. G. Bolhuis; D. Frenkel; Siun-Chuon Mau; David A. Huse. Entropy Difference between Crystal Phases. *Nature* **1997**, *388*, 236.
(152) Hilhorst, J.; Wolters, J. R.; Petukhov, A. V. Slanted Stacking Faults and Persistent Face Centered Cubic Crystal Growth in Sedimentary Colloidal Hard Sphere Crystals. *CrystEngComm* **2010**, *12* (11), 3820. https://doi.org/10.1039/c0ce00022a.
(153) Dolbnya, I. P.; Petukhov, A. V.; Aarts, D. G. A. L.; Vroege, G. J.; Lekkerkerker, H. N. W. Coexistence of Rhcp and Fcc Phases in Hard-Sphere Colloidal Crystals. *Europhysics Letters (EPL)* **2005**, *72* (6), 962–968. https://doi.org/10.1209/epl/i2005-10325-6.
(154) Yun, H.; Yu, J. W.; Lee, Y. J.; Kim, J.-S.; Park, C. H.; Nam, C.; Han, J.; Heo, T.-Y.; Choi, S.-H.; Lee, D. C.; Lee, W. B.; Stein, G. E.; Kim, B. J. Symmetry Transitions of Polymer-Grafted Nanoparticles: Grafting Density Effect. *Chemistry of Materials* **2019**, *31* (14), 5264–5273. https://doi.org/10.1021/acs.chemmater.9b01699.
(155) Ye, X.; Zhu, C.; Ercius, P.; Raja, S. N.; He, B.; Jones, M. R.; Hauwiller, M. R.; Liu, Y.; Xu, T.; Alivisatos, A. P. Structural Diversity in Binary Superlattices Self-Assembled from

Polymer-Grafted Nanocrystals. *Nature Communications* **2015**, *6* (1). https://doi.org/10.1038/ncomms10052.

(156) Wei, J.; Schaeffer, N.; Pileni, M.-P. Solvent-Mediated Crystallization of Nanocrystal 3D Assemblies of Silver Nanocrystals: Unexpected Superlattice Ripening. *Chemistry of Materials* **2016**, *28* (1), 293–302. https://doi.org/10.1021/acs.chemmater.5b04120.

(157) Li, P.; Li, Y.; Zhou, Z.-K.; Tang, S.; Yu, X.-F.; Xiao, S.; Wu, Z.; Xiao, Q.; Zhao, Y.; Wang, H.; Chu, P. K. Evaporative Self-Assembly of Gold Nanorods into Macroscopic 3D Plasmonic Superlattice Arrays. *Advanced Materials* **2016**, *28* (13), 2511–2517. https://doi.org/10.1002/adma.201505617.

(158) Zang, D.; Tarafdar, S.; Tarasevich, Y. Yu.; Dutta Choudhury, M.; Dutta, T. Evaporation of a Droplet: From Physics to Applications. *Physics Reports* **2019**, *804*, 1–56. https://doi.org/10.1016/j.physrep.2019.01.008.

(159) Bigioni, T. P.; Lin, X.-M.; Nguyen, T. T.; Corwin, E. I.; Witten, T. A.; Jaeger, H. M. Kinetically Driven Self Assembly of Highly Ordered Nanoparticle Monolayers. *Nature Materials* **2006**, *5* (4), 265–270. https://doi.org/10.1038/nmat1611.

(160) Yang, X.; Shen, X.; Long, J.; Chen, H. An Improved Median-Based Otsu Image Thresholding Algorithm. *AASRI Procedia* **2012**, *3*, 468–473. https://doi.org/10.1016/j.aasri.2012.11.074.

(161) Zack, G. W.; Rogers, W. E.; Latt, S. A. Automatic Measurement of Sister Chromatid Exchange Frequency. *Journal of Histochemistry & Cytochemistry* **1977**, *25* (7), 741–753. https://doi.org/10.1177/25.7.70454.

(162) Jui-Cheng Yen; Fu-Juay Chang; Shyang Chang. A New Criterion for Automatic Multilevel Thresholding. *IEEE Transactions on Image Processing* **1995**, *4* (3), 370–378. https://doi.org/10.1109/83.366472.

(163) Marechal, M.; Hermes, M.; Dijkstra, M. Stacking in Sediments of Colloidal Hard Spheres. *The Journal of Chemical Physics* **2011**, *135* (3), 034510. https://doi.org/10.1063/1.3609103.

(164) STS-73 Space Shuttle Crew; Zhu, J.; Li, M.; Rogers, R.; Meyer, W.; Ottewill, R. H.; Russel, W. B.; Chaikin, P. M. Crystallization of Hard-Sphere Colloids in Microgravity. *Nature* **1997**, *387* (6636), 883–885. https://doi.org/10.1038/43141.

(165) Verhaegh, N. A. M.; van Duijneveldt, J. S.; van Blaaderen, A.; Lekkerkerker, H. N. W. Direct Observation of Stacking Disorder in a Colloidal Crystal. *The Journal of Chemical Physics* **1995**, *102* (3), 1416–1421. https://doi.org/10.1063/1.468928.

(166) Chandler, D.; Percus, J. K. *Introduction to Modern Statistical Mechanics*. *Physics Today* **1988**, *41* (12), 114–118. https://doi.org/10.1063/1.2811680.

(167) Hjorth Larsen, A.; Jørgen Mortensen, J.; Blomqvist, J.; Castelli, I. E.; Christensen, R.; Dułak, M.; Friis, J.; Groves, M. N.; Hammer, B.; Hargus, C.; Hermes, E. D.; Jennings, P. C.; Bjerre Jensen, P.; Kermode, J.; Kitchin, J. R.; Leonhard Kolsbjerg, E.; Kubal, J.; Kaasbjerg, K.; Lysgaard, S.; Bergmann Maronsson, J.; Maxson, T.; Olsen, T.; Pastewka, L.; Peterson, A.; Rostgaard, C.; Schiøtz, J.; Schütt, O.; Strange, M.; Thygesen, K. S.; Vegge, T.; Vilhelmsen, L.; Walter, M.; Zeng, Z.; Jacobsen, K. W. The Atomic Simulation Environment—a Python Library for Working with Atoms. *Journal of Physics: Condensed Matter* **2017**, *29* (27), 273002. https://doi.org/10.1088/1361-648X/aa680e.

(168) Travesset, A. Soft Skyrmions, Spontaneous Valence and Selection Rules in Nanoparticle Superlattices. *ACS Nano* **2017**, *11* (6), 5375–5382. https://doi.org/10.1021/acsnano.7b02219.

(169) Kang, X.; Ruan, Q.; Zhang, H.; Bao, F.; Guo, J.; Tang, M.; Cheng, S.; Wang, J. Concave Gold Bipyramids Bound with Multiple High-Index Facets: Improved Raman and Catalytic Activities. *Nanoscale* **2017**, *9* (18), 5879–5886. https://doi.org/10.1039/C7NR00620A.

(170) Kou, X.; Zhang, S.; Tsung, C.-K.; Yeung, M. H.; Shi, Q.; Stucky, G. D.; Sun, L.; Wang, J.; Yan, C. Growth of Gold Nanorods and Bipyramids Using CTEAB Surfactant. *The Journal of Physical Chemistry B* **2006**, *110* (33), 16377–16383. https://doi.org/10.1021/jp0639086.

(171) Vigderman, L.; Khanal, B. P.; Zubarev, E. R. Functional Gold Nanorods: Synthesis, Self-Assembly, and Sensing Applications. *Advanced Materials* **2012**, *24* (36), 4811–4841. https://doi.org/10.1002/adma.201201690.

(172) Li, P.; Wu, Y.; Li, D.; Su, X.; Luo, C.; Wang, Y.; Hu, J.; Li, G.; Jiang, H.; Zhang, W. Seed-Mediated Synthesis of Tunable-Aspect-Ratio Gold Nanorods for Near-Infrared Photoacoustic Imaging. *Nanoscale Research Letters* **2018**, *13* (1). https://doi.org/10.1186/s11671-018-2734-8.

(173) Truong, N. P.; Whittaker, M. R.; Mak, C. W.; Davis, T. P. The Importance of Nanoparticle Shape in Cancer Drug Delivery. *Expert Opinion on Drug Delivery* **2015**, *12* (1), 129–142. https://doi.org/10.1517/17425247.2014.950564.

(174) Daraee, H.; Eatemadi, A.; Abbasi, E.; Fekri Aval, S.; Kouhi, M.; Akbarzadeh, A. Application of Gold Nanoparticles in Biomedical and Drug Delivery. *Artificial Cells, Nanomedicine, and Biotechnology* **2016**, *44* (1), 410–422. https://doi.org/10.3109/21691401.2014.955107.

(175) Bandyopadhyay, S.; Singh, G.; Glomm, W. R. Shape Tunable Synthesis of Anisotropic Gold Nanostructures through Binary Surfactant Mixtures. *Materials Today Chemistry* **2017**, *3*, 1–9. https://doi.org/10.1016/j.mtchem.2016.11.005.

(176) Bandyopadhyay, S.; McDonagh, B. H.; Singh, G.; Raghunathan, K.; Sandvig, A.; Sandvig, I.; Andreassen, J.-P.; Glomm, W. R. Growing Gold Nanostructures for Shape-Selective Cellular Uptake. *Nanoscale Research Letters* **2018**, *13* (1). https://doi.org/10.1186/s11671-018-2662-7.

(177) Perezjuste, J.; Pastorizasantos, I.; Lizmarzan, L.; Mulvaney, P. Gold Nanorods: Synthesis, Characterization and Applications. *Coordination Chemistry Reviews* **2005**, *249* (17–18), 1870–1901. https://doi.org/10.1016/j.ccr.2005.01.030.

(178) Lee, J.-H.; Gibson, K. J.; Chen, G.; Weizmann, Y. Bipyramid-Templated Synthesis of Monodisperse Anisotropic Gold Nanocrystals. *Nature Communications* **2015**, *6* (1). https://doi.org/10.1038/ncomms8571.

(179) Rao, W.; Li, Q.; Wang, Y.; Li, T.; Wu, L. Comparison of Photoluminescence Quantum Yield of Single Gold Nanobipyramids and Gold Nanorods. *ACS Nano* **2015**, *9* (3), 2783–2791. https://doi.org/10.1021/nn506689b.

(180) Liebig, F.; Henning, R.; Sarhan, R. M.; Prietzel, C.; Bargheer, M.; Koetz, J. A New Route to Gold Nanoflowers. *Nanotechnology* **2018**, *29* (18), 185603. https://doi.org/10.1088/1361-6528/aaaffd.

(181) Sreedhala, S.; Sudheeshkumar, V.; Vinod, C. P. Structure Sensitive Chemical Reactivity by Palladium Concave Nanocubes and Nanoflowers Synthesised by a Seed Mediated Procedure in Aqueous Medium. *Nanoscale* **2014**, *6* (13), 7496. https://doi.org/10.1039/c4nr01283f.

(182) Qiu, P.; Yang, M.; Qu, X.; Huai, Y.; Zhu, Y.; Mao, C. Tuning Photothermal Properties of Gold Nanodendrites for in Vivo Cancer Therapy within a Wide near Infrared Range by Simply Controlling Their Degree of Branching. *Biomaterials* **2016**, *104*, 138–144. https://doi.org/10.1016/j.biomaterials.2016.06.033.

(183) Kobayashi, H.; Lim, B.; Wang, J.; Camargo, P. H. C.; Yu, T.; Kim, M. J.; Xia, Y. Seed-Mediated Synthesis of Pd–Rh Bimetallic Nanodendrites. *Chemical Physics Letters* **2010**, *494* (4–6), 249–254. https://doi.org/10.1016/j.cplett.2010.06.009.

(184) Xia, Y.; Xiong, Y.; Lim, B.; Skrabalak, S. E. Shape-Controlled Synthesis of Metal Nanocrystals: Simple Chemistry Meets Complex Physics? *Angewandte Chemie International Edition* **2009**, *48* (1), 60–103. https://doi.org/10.1002/anie.200802248.

(185) Gole, A.; Murphy, C. J. Seed-Mediated Synthesis of Gold Nanorods: Role of the Size and Nature of the Seed. *Chemistry of Materials* **2004**, *16* (19), 3633–3640. https://doi.org/10.1021/cm0492336.

(186) Mettela, G.; Boya, R.; Singh, D.; Kumar, G. V. P.; Kulkarni, G. U. Highly Tapered Pentagonal Bipyramidal Au Microcrystals with High Index Faceted Corrugation: Synthesis and Optical Properties. *Scientific Reports* **2013**, *3* (1). https://doi.org/10.1038/srep01793.

(187) Li, N.; Zhao, P.; Astruc, D. Anisotropic Gold Nanoparticles: Synthesis, Properties, Applications, and Toxicity. *Angewandte Chemie International Edition* **2014**, *53* (7), 1756–1789. https://doi.org/10.1002/anie.201300441.

(188) Wang, Z. L.; Mohamed, M. B.; Link, S.; El-Sayed, M. A. Crystallographic Facets and Shapes of Gold Nanorods of Different Aspect Ratios. *Surface Science* **1999**, *440* (1–2), L809–L814. https://doi.org/10.1016/S0039-6028(99)00865-1.

(189) Johnson, C. J.; Dujardin, E.; Davis, S. A.; Murphy, C. J.; Mann, S. Growth and Form of Gold Nanorods Prepared by Seed-Mediated, Surfactant-Directed Synthesis. *Journal of Materials Chemistry* **2002**, *12* (6), 1765–1770. https://doi.org/10.1039/b200953f.

(190) Liu, M.; Guyot-Sionnest, P. Mechanism of Silver(I)-Assisted Growth of Gold Nanorods and Bipyramids. *The Journal of Physical Chemistry B* **2005**, *109* (47), 22192–22200. https://doi.org/10.1021/jp054808n.

(191) Burgin, J.; Florea, I.; Majimel, J.; Dobri, A.; Ersen, O.; Tréguer-Delapierre, M. 3D Morphology of Au and Au@Ag Nanobipyramids. *Nanoscale* **2012**, *4* (4), 1299. https://doi.org/10.1039/c2nr11454b.

(192) Dondapati, S. K.; Sau, T. K.; Hrelescu, C.; Klar, T. A.; Stefani, F. D.; Feldmann, J. Label-Free Biosensing Based on Single Gold Nanostars as Plasmonic Transducers. *ACS Nano* **2010**, *4* (11), 6318–6322. https://doi.org/10.1021/nn100760f.

(193) Grochola, G.; Snook, I. K.; Russo, S. P. Computational Modeling of Nanorod Growth. *The Journal of Chemical Physics* **2007**, *127* (19), 194707. https://doi.org/10.1063/1.2789420.

(194) Navarro, J. R. G.; Manchon, D.; Lerouge, F.; Cottancin, E.; Lermé, J.; Bonnet, C.; Chaput, F.; Mosset, A.; Pellarin, M.; Parola, S. Synthesis, Electron Tomography and Single-Particle Optical Response of Twisted Gold Nano-Bipyramids. *Nanotechnology* **2012**, *23* (14), 145707. https://doi.org/10.1088/0957-4484/23/14/145707.

(195) Suh, I.-K.; Ohta, H.; Waseda, Y. High-Temperature Thermal Expansion of Six Metallic Elements Measured by Dilatation Method and X-Ray Diffraction. *Journal of Materials Science* **1988**, *23* (2), 757–760. https://doi.org/10.1007/BF01174717.

(196) Marinakos, S. M.; Chen, S.; Chilkoti, A. Plasmonic Detection of a Model Analyte in Serum by a Gold Nanorod Sensor. *Analytical Chemistry* **2007**, *79* (14), 5278–5283. https://doi.org/10.1021/ac0706527.

(197) Hazen, R. M. Chiral Crystal Faces of Common Rock-Forming Minerals. In *Progress in Biological Chirality*; Elsevier, 2004; pp 137–151. https://doi.org/10.1016/B978-008044396-6/50013-7.

(198) Hazen, R. M.; Filley, T. R.; Goodfriend, G. A. Selective Adsorption of L- and D-Amino Acids on Calcite: Implications for Biochemical Homochirality. *Proceedings of the National Academy of Sciences* **2001**, *98* (10), 5487–5490. https://doi.org/10.1073/pnas.101085998.

(199) Dutta, S.; Gellman, A. J. Enantiomer Surface Chemistry: Conglomerate *versus* Racemate Formation on Surfaces. *Chemical Society Reviews* **2017**, *46* (24), 7787–7839. https://doi.org/10.1039/C7CS00555E.

(200) Dong, Z.; Ma, Y. Atomic-Level Handedness Determination of Chiral Crystals Using Aberration-Corrected Scanning Transmission Electron Microscopy. *Nature Communications* **2020**, *11* (1). https://doi.org/10.1038/s41467-020-15388-5.